

ULTRAVIOLET PHOTOCHEMISTRY OF THE GROUP-V HYDRIDES

by

Lee-Ann M. Smith-Freeman

A dissertation Presented to the
FACULTY OF THE GRADUATE SCHOOL
UNIVERSITY OF SOUTHERN CALIFORNIA
In Partial Fulfillment of the
Requirements for the Degree
DOCTOR OF PHILOSOPHY
(CHEMISTRY)

August 2009

Copyright 2009

Lee-Ann M. Smith-Freeman

Epigraph

I may not have gone where I intended to go, but I think I
have ended up where I intended to be.

~Douglas Adams

Acknowledgements

Graduate school has been the ultimate learning experience, both in and outside the laboratory. I have evolved from a quiet student to a confident adult, eager to embrace my future and carve my own niche. The love, support and guidance I have received from my family, friends and advisor have made this transformation possible.

It is difficult to articulate the gratitude I have for my advisor, Professor Curt Wittig; words are insufficient. His patience, generosity, quick wit and dry humor have inspired me to become the best I can be, both in science and in life. From his example, I have learned that I should never fear questions, but rather fear their absence.

I also owe many thanks to Professor Hanna Reisler. Her encouragement and support of me, and to all women in science, has been remarkable. She has taught me to own and voice my ideas, and take pride in my accomplishments.

The staff in the Chemistry department has made my graduate school experience as smooth and stress-free as possible. Michele Dea always had an answer for me, and Heather Connor never tired of helping me with my finances. Yuki Yabuta and Valerie Childress brightened my day and always informed me of the power/water shutdowns that intermittently plagued Seaver Science Center. Special thanks also go to Corey Schultz, Jim Merritt, Phillip Sliwoski, Thuc Do, Bruno Herreros, Don R. Wiggins and Ross Lewis.

I would especially like to thank my colleagues, past and present, in the Wittig group. Dr. Joelle Underwood first introduced me to the laboratory and provided me with excellent advice on how to navigate graduate school. I admire her passion, enthusiasm

and determination. For the past three years, William Schroeder has been my partner in the laboratory. His ability to function on minimal sleep was admirable especially for experiments that lasted 24 to 48 hours. I would also like to recognize George Kumi, Sergey Malyk, Jessica Quinn, Christopher Nemirow, Anton Zadorozhny, Zhou Lu, Jordan Fine and Oscar Rebolledo-Mayoral; we have had some great times together!

Dr. Jessie Parr has been an incredible friend, my best friend, throughout graduate school. She was always there to encourage me, exchange gossip and venture to Starbucks for much needed breaks. Her compassion and genuine kindness set her apart as a wonderful friend whom I will always cherish.

A Special thanks to Bobby Cockrill. Since freshman year of college, he has been one of my closest and dearest friends, as well as an integral part of my family. His energy, enthusiasm, and constant optimism have kept me going. I would also like to thank another college friend and honorary family member, Laura Bach. Her visits to Los Angeles were a highlight during graduate school, and helped me unwind and enjoy the moment.

Dr. Whitney Waldroup-Hovenic, my childhood friend, my sister on all accounts, deserves recognition, as well. She attended medical school while I completed my graduate research and our conversations (venting sessions) helped me stay focused and positive despite the pressure. I also cannot forget Kelly English. She is truly a free spirit and continually reminds me to treasure life and its adventures.

Finally, I want to acknowledge my family. My parents, Dr. Ladd Smith and Barbara Smith, have been my biggest cheerleaders. They have endured the highs and lows that accompany the roller coaster that is graduate school: panicked phone calls in the middle of the night, bizarre behavior due to stress, etc. They have endured with grace, patience and love. My brother, Brett, has always been there to make me smile and laugh. He is one of the most loyal and genuine people I am privileged to know. I am so proud of him, and I know he is proud of me. My in-laws, Gary and Maggie Freeman, have welcomed me unconditionally into their family. They are extremely generous with their love and support, and I feel blessed to have them in my corner. My brother-in-law, Chris Freeman, has introduced me to the world of hip-hop, cheesy chingalingas and sarcastic banter, all of which have helped me survive graduate school. I would also like to thank Adria Price, whose advice and encouragement have helped me define my future. To precious Adrianna Freeman, I thank you for being my most sweet, beautiful, gentle niece; you will always be a princess in my book.

To my husband, Matthew Smith-Freeman, I thank you for your love, your strength and your unwavering faith in me. You have stood by me even when I littered our apartment with scientific journals, even when I declared a home cooked meal was synonymous with cold cereal, even when my fashion style was limited to dirty lab clothes covered in pump oil. Despite the challenges and stormy weather, we have arrived together. I love you with all that I am.

Table of Contents

Epigraph	ii
Acknowledgements	iii
List of Tables	viii
List of Figures	ix
Abstract	xii
Chapter 1 Introduction	1
1.1 Periodic Trends and Anomalies	2
1.2 Photodissociation Dynamics	5
1.2.1 Experimental Approaches	9
1.2.2 Theoretical Approaches	11
1.3 Relativistic Calculations	17
1.3.1 Potential Energy Surfaces and Relativity	19
1.4 Group-V Hydrides	20
1.5 Chapter 1 References	24
Chapter 2 Experimental Methods	27
2.1 Time-of-flight Spectroscopy	28
2.1.1 Hydrogen Atom Time-of-flight Spectroscopy	30
2.1.2 High- <i>n</i> Rydberg Hydrogen Time-of-flight Spectroscopy	31
2.2 Experimental Details	32
2.2.1 Vacuum System	34
2.2.2 Detector Assembly	35
2.2.3 Laser Systems	35
2.2.4 Laser and Molecular Beam Alignment	39
2.3 Chapter 2 References	41
Chapter 3 The Ultraviolet Photochemistry of AsH₃	43
3.1 Introduction	44
3.2 Experimental Method and Results	52
3.3 Discussion	58
3.3.1 Primary photolysis: $\text{AsH}_3 \rightarrow \text{AsH}_2 + \text{H}$	59
3.3.2 AsH ₂ internal excitations	62
3.3.3 Secondary photolysis: $\text{AsH}_2 \rightarrow \text{AsH} + \text{H}$	66
3.4 Conclusions	68

		vii
3.5	Chapter 3 References	71
Chapter 4	Future Directions	74
4.1	SbH ₃	75
	4.1.1 SbH ₃ Synthesis	81
	4.1.2 Ultraviolet Absorption Spectrum of SbH ₃	82
	4.1.3 High- <i>n</i> Rydberg Time-of-flight Experiments	82
	4.1.4 Discussion	84
4.2	BiH ₃	86
4.3	A quick look at AsH ₂	86
	4.3.1 SbH ₂ and BiH ₂	90
4.4	Chapter 4 References	91
Bibliography		93

List of Tables

Table 3.1	Equilibrium H-M-H angles for N, P and As, and related electronic states	48
Table 4.1	Equilibrium H-M-H angles for N, P, As, and Sb, and related electronic states	77

List of Figures

Figure 1.1	Periodic Table. In general, atomic radii decrease, ionization energies and electronegativities increase moving left to right in a period. Atomic radii, ionization energies and electronegativities decrease moving down a group	3
Figure 1.2	Illustration of direct dissociation (adapted from reference 11): $AB + h\nu \rightarrow AB^* \rightarrow A + B$. AB^* is the photoexcited complex and R_{AB} represents the internuclear distance between A and B	7
Figure 1.3	Illustration of indirect photodissociation (adapted from reference 11). AB^* is the photoexcited complex, and R_{AB} represents the internuclear distance between A and B. (a) AB^* dissociates <i>via</i> IVR or tunneling. (b) AB^* dissociates <i>via</i> a transition from a bound electronic state to a repulsive electronic state	8
Figure 1.4	(a) Adiabatic (U_1 , U_2) and (b) diabatic (V_1 , V_2) potential energy surfaces of NH_3 . θ is the angle between a NH bond and the normal to the trigonal plane ($\theta = 90^\circ$ represents a planar geometry). Note the presence of a conical intersection between the adiabatic PESs at $\theta = 90^\circ$ and $R = 2.13 \text{ \AA}$	16
Figure 1.5	Potential energy curves for SbH (a) without SO coupling and (b) with SO coupling	21
Figure 1.6	Potential energy curves for BiH (a) without SO coupling and (b) with SO coupling	22
Figure 2.1	The velocity of fragment A in the c.m. frame	29
Figure 2.2	Schematic of the HRTOF apparatus. Components include: 1) source chamber, 2) molecular beam, 3) pulsed nozzle, 4) skimmer, 5) main chamber, 6) electrode pair, 7) alignment bar, 8) linear motion feedthrough, 9) RGA, 10) TOF tube, 11) detector assembly, 12) turbomolecular pump, 13) gate valve, 14) diffusion pump	33
Figure 2.3	Schematic of the detector assembly	36
Figure 2.4	Schematic of the main chamber and laser radiation pathways	37
Figure 2.5	Schematic of the alignment bar	39
Figure 3.1	The ground and excited state potential energy surfaces of NH_3 .	46

Vertical excitation from the $\text{NH}_3 \tilde{X}^1A_1$ ground vibrational level to \tilde{A}^1A_2 can lead to dissociation to $\text{NH}_2(\tilde{A}^2A_1)$ via adiabatic paths, or to $\text{NH}_2(\tilde{X}^2B_1)$ via nonadiabatic paths that pass near the conical intersection. θ is the angle between an NH bond and the normal to the trigonal plane. $\theta = 90^\circ$ corresponds to planar geometry

- Figure 3.2** Energies relevant to 193 nm photolysis of AsH_3 are indicated, including product species that can undergo secondary photodissociation. The two red arrows and shaded rectangles to the right of the $\text{AsH}_2 + \text{H}$ column indicate the range of energies associated with internally excited AsH_2 51
- Figure 3.3** Schematic of the experimental arrangement 53
- Figure 3.4** HRTOF spectrum obtained using 10% AsH_3 and 193 nm photolysis: Results from 121,000 laser firings were summed to obtain the trace. The 193 nm energy ranged between 2.2 and 2.5 mJ. The vertical dashed lines indicate the earliest possible arrival time compatible with 1-photon AsH_3 photodissociation 54
- Figure 3.5** HRTOF spectra for photolysis energies of 0.5 and 4.2 mJ; 135,000 and 116,000 laser firings, respectively 56
- Figure 3.6** (a) The HRTOF spectrum in Fig. 4 has been converted to $P(E_{\text{c.m.}})$; inset: expanded view of the high-energy region. The black dashed line to the right of the red box indicates the maximum $E_{\text{c.m.}}$ available to a 1-photon process. The blue dashed line in the blue box indicates the maximum $E_{\text{c.m.}}$ available to the $\text{AsH}_2(\tilde{A})$ channel via a 1-photon process. (b) This pertains to the blue box in (a). To highlight peaks, the underlying continuous distribution has been suppressed. (c) This pertains to the red box in (a). To highlight peaks, the underlying continuous distribution has been suppressed 57
- Figure 3.7** Low energy features can be fit using high J values and various distributions of low K_c values 65
- Figure 4.1** Energy level diagram for the 193.3 and 248 nm photolysis of SbH_3 . The 193.3 nm photon energy is significantly greater than the SbH_3 bond dissociation energy. The product species that can undergo secondary photodissociation are also shown. The shaded rectangles indicate possible energy ranges for internally excited SbH_2 . The spin-orbit SbH states are not shown here 80

- Figure 4.2** Room temperature absorption spectrum of SbH_3 ; inset: expanded view of the 230-300 nm region 83
- Figure 4.3** Energy level diagram for the 193.3 and 248 nm photolysis of BiH_3 . It should be noted that spin-orbit coupling splits the electronic states of BiH into numerous relativistic states. Only a few BiH spin-orbit state are shown here 87
- Figure 4.4** Schematic of a HRTOF experiment designed to probe AsH_2 89

Abstract

This dissertation discusses the molecular properties and ultraviolet photochemistry of the group-V hydrides (NH_3 , PH_3 , AsH_3 , SbH_3 , BiH_3). Relativistic effects become increasingly important for the heavier group-V hydrides and can be manifest in studies of the photodissociation dynamics.

High- n Rydberg time-of-flight (HRTOF) spectroscopy has been used to study the 193.3 nm photolysis of AsH_3 . The center-of-mass (c.m.) translational energy distribution for the one-photon process, $\text{AsH}_3 + h\nu \rightarrow \text{AsH}_2 + \text{H}$, $P(E_{\text{c.m.}})$, indicates that AsH_2 internal excitation accounts for $\sim 64\%$ of the available energy [i.e., $h\nu - D_0(\text{H}_2\text{As-H})$]. Secondary AsH_2 photodissociation also takes place. Analyses of superimposed structure atop the broad $P(E_{\text{c.m.}})$ distribution suggest that AsH_2 is formed with significant a-axis rotation as well as bending excitation. Comparison of the results obtained with AsH_3 versus those of the lighter group-V hydrides (NH_3 , PH_3) lends support to the proposed mechanisms. Of the group-V hydrides, AsH_3 lies intermediate between the nonrelativistic and relativistic regimes, requiring high-level electronic structure theory.

The room temperature absorption spectrum of SbH_3 has been recorded. The absorption spectrum is a broad continuum with no discernible structure; however, a long-wavelength tail is evident. The HRTOF technique has also been used to investigate the photodissociation dynamics of SbH_3 following 193.3 nm photolysis. The overall shapes of the translational energy distributions were inconsistent, precluding confident analysis. In spite of this, it is apparent that SbH_2 products are formed with substantial internal

excitation and secondary photodissociation occurs. These general observations are consistent with the results obtained for AsH₃.

Chapter 1

Introduction

This dissertation presents a quantitative understanding of the molecular and spectroscopic properties of the group-V hydrides, NH_3 , PH_3 , AsH_3 , SbH_3 and BiH_3 . An in-depth study of how photochemical and photophysical mechanisms vary when the lightest group-V hydride, NH_3 , is replaced by its heavier homologues provide insight into group trends. The group-V hydrides span the nonrelativistic and relativistic regimes, thus the influence of relativistic effects on the photodissociation dynamics of these molecules is manifest. Section 1.1 describes trends and anomalies in the periodic table. The experimental and theoretical study of photodissociation dynamics is critical to understanding photochemistry and is discussed in section 1.2. Section 1.3 outlines relativistic theoretical computations and section 1.4 introduces the group-V hydrides.

1.1 Periodic Trends and Anomalies

As long as chemistry is studied there will be a periodic table. And even if someday we communicate with another part of the universe, we can be sure that one thing that both cultures will have in common is an ordered system of elements that will be instantly recognizable by both intelligent life forms. ~ John Emsley

The periodic table is the ultimate reference tool for Chemistry. Dmitri Mendeleev is often credited with the formation of the modern periodic table, however, many notable scientists contributed to its evolution.¹⁻⁴ To date, there are ~ 700 forms of the periodic table, constructed in unique arrangements designed to highlight specific properties of the elements.^{1,2}

This discussion will focus on the form of the periodic table that organizes chemical elements in order of increasing atomic number Z . As a result, chemical periodicity emerges (Figure 1.1). Patterns in the chemical and physical properties of the elements can be explained in terms of the electronic configuration of the elements.^{1,2,5} Thus, the periodic table bridges macroscopic chemical properties with quantum mechanics. These regularities give insight into the nature of chemical bonding and can lead to the prediction of new elements and compounds.

Predictions based on chemical periodicity often fail when applied to the heavier elements.^{2,6-10} Several well known chemical anomalies include: Lanthanide contraction, the color of gold, the inert pair effect, the stability of the mercurous ion, Hg_2^{2+} , the liquid nature of mercury, and spin-orbit splitting. These anomalous trends result from

Legend:
 Solids (White)
 Liquids (Blue)
 Gases (Pink)
 Artificially Prepared (Yellow)

Group 1 (IA): 1 H, 2 Li, 3 Na, 4 K, 5 Rb, 6 Cs, 7 Fr
Group 2 (IIA): 3 He, 4 Be, 5 Mg, 6 Ca, 7 Sr, 8 Ba, 9 Ra
Group 13 (IIIA): 5 B, 6 Al, 7 Ga, 8 In, 9 Tl, 10 Uuq
Group 14 (IVA): 6 C, 7 Si, 8 Ge, 9 Sn, 10 Pb, 11 Uuh
Group 15 (VA): 7 N, 8 P, 9 As, 10 Sb, 11 Bi, 12 Uub
Group 16 (VIA): 8 O, 9 S, 10 Se, 11 Te, 12 Po, 13 Uuh
Group 17 (VIIA): 9 F, 10 Cl, 11 Br, 12 I, 13 At, 14 Uub
Group 18 (VIII): 10 Ne, 11 Ar, 12 Kr, 13 Xe, 14 Rn, 15 Uuo, 16 Uuq, 17 Uuh, 18 Uuo

Transition Metals (Groups 3-10): 3 Sc, 4 Ti, 5 V, 6 Cr, 7 Mn, 8 Fe, 9 Co, 10 Ni, 11 Cu, 12 Zn, 13 Ga, 14 Ge, 15 As, 16 Se, 17 Br, 18 Kr, 19 Rb, 20 Sr, 21 Y, 22 Zr, 23 Nb, 24 Mo, 25 Tc, 26 Ru, 27 Rh, 28 Pd, 29 Ag, 30 Cd, 31 In, 32 Sn, 33 Sb, 34 Te, 35 I, 36 Xe, 37 Rb, 38 Sr, 39 Y, 40 Zr, 41 Nb, 42 Mo, 43 Tc, 44 Ru, 45 Rh, 46 Pd, 47 Ag, 48 Cd, 49 In, 50 Sn, 51 Sb, 52 Te, 53 I, 54 Xe, 55 Rb, 56 Sr, 57 Y, 58 Zr, 59 Nb, 60 Mo, 61 Tc, 62 Ru, 63 Rh, 64 Pd, 65 Ag, 66 Cd, 67 In, 68 Sn, 69 Sb, 70 Te, 71 I, 72 Xe, 73 Rb, 74 Sr, 75 Y, 76 Zr, 77 Nb, 78 Mo, 79 Tc, 80 Ru, 81 Rh, 82 Pd, 83 Ag, 84 Cd, 85 In, 86 Sn, 87 Sb, 88 Te, 89 I, 90 Xe, 91 Rb, 92 Sr, 93 Y, 94 Zr, 95 Nb, 96 Mo, 97 Tc, 98 Ru, 99 Rh, 100 Pd, 101 Ag, 102 Cd, 103 In, 104 Sn, 105 Sb, 106 Te, 107 I, 108 Xe, 109 Rb, 110 Sr, 111 Y, 112 Zr, 113 Nb, 114 Mo, 115 Tc, 116 Ru, 117 Rh, 118 Pd, 119 Ag, 120 Cd, 121 In, 122 Sn, 123 Sb, 124 Te, 125 I, 126 Xe, 127 Rb, 128 Sr, 129 Y, 130 Zr, 131 Nb, 132 Mo, 133 Tc, 134 Ru, 135 Rh, 136 Pd, 137 Ag, 138 Cd, 139 In, 140 Sn, 141 Sb, 142 Te, 143 I, 144 Xe, 145 Rb, 146 Sr, 147 Y, 148 Zr, 149 Nb, 150 Mo, 151 Tc, 152 Ru, 153 Rh, 154 Pd, 155 Ag, 156 Cd, 157 In, 158 Sn, 159 Sb, 160 Te, 161 I, 162 Xe, 163 Rb, 164 Sr, 165 Y, 166 Zr, 167 Nb, 168 Mo, 169 Tc, 170 Ru, 171 Rh, 172 Pd, 173 Ag, 174 Cd, 175 In, 176 Sn, 177 Sb, 178 Te, 179 I, 180 Xe, 181 Rb, 182 Sr, 183 Y, 184 Zr, 185 Nb, 186 Mo, 187 Tc, 188 Ru, 189 Rh, 190 Pd, 191 Ag, 192 Cd, 193 In, 194 Sn, 195 Sb, 196 Te, 197 I, 198 Xe, 199 Rb, 200 Sr, 201 Y, 202 Zr, 203 Nb, 204 Mo, 205 Tc, 206 Ru, 207 Rh, 208 Pd, 209 Ag, 210 Cd, 211 In, 212 Sn, 213 Sb, 214 Te, 215 I, 216 Xe, 217 Rb, 218 Sr, 219 Y, 220 Zr, 221 Nb, 222 Mo, 223 Tc, 224 Ru, 225 Rh, 226 Pd, 227 Ag, 228 Cd, 229 In, 230 Sn, 231 Sb, 232 Te, 233 I, 234 Xe, 235 Rb, 236 Sr, 237 Y, 238 Zr, 239 Nb, 240 Mo, 241 Tc, 242 Ru, 243 Rh, 244 Pd, 245 Ag, 246 Cd, 247 In, 248 Sn, 249 Sb, 250 Te, 251 I, 252 Xe, 253 Rb, 254 Sr, 255 Y, 256 Zr, 257 Nb, 258 Mo, 259 Tc, 260 Ru, 261 Rh, 262 Pd, 263 Ag, 264 Cd, 265 In, 266 Sn, 267 Sb, 268 Te, 269 I, 270 Xe, 271 Rb, 272 Sr, 273 Y, 274 Zr, 275 Nb, 276 Mo, 277 Tc, 278 Ru, 279 Rh, 280 Pd, 281 Ag, 282 Cd, 283 In, 284 Sn, 285 Sb, 286 Te, 287 I, 288 Xe, 289 Rb, 290 Sr, 291 Y, 292 Zr, 293 Nb, 294 Mo, 295 Tc, 296 Ru, 297 Rh, 298 Pd, 299 Ag, 300 Cd, 301 In, 302 Sn, 303 Sb, 304 Te, 305 I, 306 Xe, 307 Rb, 308 Sr, 309 Y, 310 Zr, 311 Nb, 312 Mo, 313 Tc, 314 Ru, 315 Rh, 316 Pd, 317 Ag, 318 Cd, 319 In, 320 Sn, 321 Sb, 322 Te, 323 I, 324 Xe, 325 Rb, 326 Sr, 327 Y, 328 Zr, 329 Nb, 330 Mo, 331 Tc, 332 Ru, 333 Rh, 334 Pd, 335 Ag, 336 Cd, 337 In, 338 Sn, 339 Sb, 340 Te, 341 I, 342 Xe, 343 Rb, 344 Sr, 345 Y, 346 Zr, 347 Nb, 348 Mo, 349 Tc, 350 Ru, 351 Rh, 352 Pd, 353 Ag, 354 Cd, 355 In, 356 Sn, 357 Sb, 358 Te, 359 I, 360 Xe, 361 Rb, 362 Sr, 363 Y, 364 Zr, 365 Nb, 366 Mo, 367 Tc, 368 Ru, 369 Rh, 370 Pd, 371 Ag, 372 Cd, 373 In, 374 Sn, 375 Sb, 376 Te, 377 I, 378 Xe, 379 Rb, 380 Sr, 381 Y, 382 Zr, 383 Nb, 384 Mo, 385 Tc, 386 Ru, 387 Rh, 388 Pd, 389 Ag, 390 Cd, 391 In, 392 Sn, 393 Sb, 394 Te, 395 I, 396 Xe, 397 Rb, 398 Sr, 399 Y, 400 Zr, 401 Nb, 402 Mo, 403 Tc, 404 Ru, 405 Rh, 406 Pd, 407 Ag, 408 Cd, 409 In, 410 Sn, 411 Sb, 412 Te, 413 I, 414 Xe, 415 Rb, 416 Sr, 417 Y, 418 Zr, 419 Nb, 420 Mo, 421 Tc, 422 Ru, 423 Rh, 424 Pd, 425 Ag, 426 Cd, 427 In, 428 Sn, 429 Sb, 430 Te, 431 I, 432 Xe, 433 Rb, 434 Sr, 435 Y, 436 Zr, 437 Nb, 438 Mo, 439 Tc, 440 Ru, 441 Rh, 442 Pd, 443 Ag, 444 Cd, 445 In, 446 Sn, 447 Sb, 448 Te, 449 I, 450 Xe, 451 Rb, 452 Sr, 453 Y, 454 Zr, 455 Nb, 456 Mo, 457 Tc, 458 Ru, 459 Rh, 460 Pd, 461 Ag, 462 Cd, 463 In, 464 Sn, 465 Sb, 466 Te, 467 I, 468 Xe, 469 Rb, 470 Sr, 471 Y, 472 Zr, 473 Nb, 474 Mo, 475 Tc, 476 Ru, 477 Rh, 478 Pd, 479 Ag, 480 Cd, 481 In, 482 Sn, 483 Sb, 484 Te, 485 I, 486 Xe, 487 Rb, 488 Sr, 489 Y, 490 Zr, 491 Nb, 492 Mo, 493 Tc, 494 Ru, 495 Rh, 496 Pd, 497 Ag, 498 Cd, 499 In, 500 Sn, 501 Sb, 502 Te, 503 I, 504 Xe, 505 Rb, 506 Sr, 507 Y, 508 Zr, 509 Nb, 510 Mo, 511 Tc, 512 Ru, 513 Rh, 514 Pd, 515 Ag, 516 Cd, 517 In, 518 Sn, 519 Sb, 520 Te, 521 I, 522 Xe, 523 Rb, 524 Sr, 525 Y, 526 Zr, 527 Nb, 528 Mo, 529 Tc, 530 Ru, 531 Rh, 532 Pd, 533 Ag, 534 Cd, 535 In, 536 Sn, 537 Sb, 538 Te, 539 I, 540 Xe, 541 Rb, 542 Sr, 543 Y, 544 Zr, 545 Nb, 546 Mo, 547 Tc, 548 Ru, 549 Rh, 550 Pd, 551 Ag, 552 Cd, 553 In, 554 Sn, 555 Sb, 556 Te, 557 I, 558 Xe, 559 Rb, 560 Sr, 561 Y, 562 Zr, 563 Nb, 564 Mo, 565 Tc, 566 Ru, 567 Rh, 568 Pd, 569 Ag, 570 Cd, 571 In, 572 Sn, 573 Sb, 574 Te, 575 I, 576 Xe, 577 Rb, 578 Sr, 579 Y, 580 Zr, 581 Nb, 582 Mo, 583 Tc, 584 Ru, 585 Rh, 586 Pd, 587 Ag, 588 Cd, 589 In, 590 Sn, 591 Sb, 592 Te, 593 I, 594 Xe, 595 Rb, 596 Sr, 597 Y, 598 Zr, 599 Nb, 600 Mo, 601 Tc, 602 Ru, 603 Rh, 604 Pd, 605 Ag, 606 Cd, 607 In, 608 Sn, 609 Sb, 610 Te, 611 I, 612 Xe, 613 Rb, 614 Sr, 615 Y, 616 Zr, 617 Nb, 618 Mo, 619 Tc, 620 Ru, 621 Rh, 622 Pd, 623 Ag, 624 Cd, 625 In, 626 Sn, 627 Sb, 628 Te, 629 I, 630 Xe, 631 Rb, 632 Sr, 633 Y, 634 Zr, 635 Nb, 636 Mo, 637 Tc, 638 Ru, 639 Rh, 640 Pd, 641 Ag, 642 Cd, 643 In, 644 Sn, 645 Sb, 646 Te, 647 I, 648 Xe, 649 Rb, 650 Sr, 651 Y, 652 Zr, 653 Nb, 654 Mo, 655 Tc, 656 Ru, 657 Rh, 658 Pd, 659 Ag, 660 Cd, 661 In, 662 Sn, 663 Sb, 664 Te, 665 I, 666 Xe, 667 Rb, 668 Sr, 669 Y, 670 Zr, 671 Nb, 672 Mo, 673 Tc, 674 Ru, 675 Rh, 676 Pd, 677 Ag, 678 Cd, 679 In, 680 Sn, 681 Sb, 682 Te, 683 I, 684 Xe, 685 Rb, 686 Sr, 687 Y, 688 Zr, 689 Nb, 690 Mo, 691 Tc, 692 Ru, 693 Rh, 694 Pd, 695 Ag, 696 Cd, 697 In, 698 Sn, 699 Sb, 700 Te, 701 I, 702 Xe, 703 Rb, 704 Sr, 705 Y, 706 Zr, 707 Nb, 708 Mo, 709 Tc, 710 Ru, 711 Rh, 712 Pd, 713 Ag, 714 Cd, 715 In, 716 Sn, 717 Sb, 718 Te, 719 I, 720 Xe, 721 Rb, 722 Sr, 723 Y, 724 Zr, 725 Nb, 726 Mo, 727 Tc, 728 Ru, 729 Rh, 730 Pd, 731 Ag, 732 Cd, 733 In, 734 Sn, 735 Sb, 736 Te, 737 I, 738 Xe, 739 Rb, 740 Sr, 741 Y, 742 Zr, 743 Nb, 744 Mo, 745 Tc, 746 Ru, 747 Rh, 748 Pd, 749 Ag, 750 Cd, 751 In, 752 Sn, 753 Sb, 754 Te, 755 I, 756 Xe, 757 Rb, 758 Sr, 759 Y, 760 Zr, 761 Nb, 762 Mo, 763 Tc, 764 Ru, 765 Rh, 766 Pd, 767 Ag, 768 Cd, 769 In, 770 Sn, 771 Sb, 772 Te, 773 I, 774 Xe, 775 Rb, 776 Sr, 777 Y, 778 Zr, 779 Nb, 780 Mo, 781 Tc, 782 Ru, 783 Rh, 784 Pd, 785 Ag, 786 Cd, 787 In, 788 Sn, 789 Sb, 790 Te, 791 I, 792 Xe, 793 Rb, 794 Sr, 795 Y, 796 Zr, 797 Nb, 798 Mo, 799 Tc, 800 Ru, 801 Rh, 802 Pd, 803 Ag, 804 Cd, 805 In, 806 Sn, 807 Sb, 808 Te, 809 I, 810 Xe, 811 Rb, 812 Sr, 813 Y, 814 Zr, 815 Nb, 816 Mo, 817 Tc, 818 Ru, 819 Rh, 820 Pd, 821 Ag, 822 Cd, 823 In, 824 Sn, 825 Sb, 826 Te, 827 I, 828 Xe, 829 Rb, 830 Sr, 831 Y, 832 Zr, 833 Nb, 834 Mo, 835 Tc, 836 Ru, 837 Rh, 838 Pd, 839 Ag, 840 Cd, 841 In, 842 Sn, 843 Sb, 844 Te, 845 I, 846 Xe, 847 Rb, 848 Sr, 849 Y, 850 Zr, 851 Nb, 852 Mo, 853 Tc, 854 Ru, 855 Rh, 856 Pd, 857 Ag, 858 Cd, 859 In, 860 Sn, 861 Sb, 862 Te, 863 I, 864 Xe, 865 Rb, 866 Sr, 867 Y, 868 Zr, 869 Nb, 870 Mo, 871 Tc, 872 Ru, 873 Rh, 874 Pd, 875 Ag, 876 Cd, 877 In, 878 Sn, 879 Sb, 880 Te, 881 I, 882 Xe, 883 Rb, 884 Sr, 885 Y, 886 Zr, 887 Nb, 888 Mo, 889 Tc, 890 Ru, 891 Rh, 892 Pd, 893 Ag, 894 Cd, 895 In, 896 Sn, 897 Sb, 898 Te, 899 I, 900 Xe, 901 Rb, 902 Sr, 903 Y, 904 Zr, 905 Nb, 906 Mo, 907 Tc, 908 Ru, 909 Rh, 910 Pd, 911 Ag, 912 Cd, 913 In, 914 Sn, 915 Sb, 916 Te, 917 I, 918 Xe, 919 Rb, 920 Sr, 921 Y, 922 Zr, 923 Nb, 924 Mo, 925 Tc, 926 Ru, 927 Rh, 928 Pd, 929 Ag, 930 Cd, 931 In, 932 Sn, 933 Sb, 934 Te, 935 I, 936 Xe, 937 Rb, 938 Sr, 939 Y, 940 Zr, 941 Nb, 942 Mo, 943 Tc, 944 Ru, 945 Rh, 946 Pd, 947 Ag, 948 Cd, 949 In, 950 Sn, 951 Sb, 952 Te, 953 I, 954 Xe, 955 Rb, 956 Sr, 957 Y, 958 Zr, 959 Nb, 960 Mo, 961 Tc, 962 Ru, 963 Rh, 964 Pd, 965 Ag, 966 Cd, 967 In, 968 Sn, 969 Sb, 970 Te, 971 I, 972 Xe, 973 Rb, 974 Sr, 975 Y, 976 Zr, 977 Nb, 978 Mo, 979 Tc, 980 Ru, 981 Rh, 982 Pd, 983 Ag, 984 Cd, 985 In, 986 Sn, 987 Sb, 988 Te, 989 I, 990 Xe, 991 Rb, 992 Sr, 993 Y, 994 Zr, 995 Nb, 996 Mo, 997 Tc, 998 Ru, 999 Rh, 1000 Pd, 1001 Ag, 1002 Cd, 1003 In, 1004 Sn, 1005 Sb, 1006 Te, 1007 I, 1008 Xe, 1009 Rb, 1010 Sr, 1011 Y, 1012 Zr, 1013 Nb, 1014 Mo, 1015 Tc, 1016 Ru, 1017 Rh, 1018 Pd, 1019 Ag, 1020 Cd, 1021 In, 1022 Sn, 1023 Sb, 1024 Te, 1025 I, 1026 Xe, 1027 Rb, 1028 Sr, 1029 Y, 1030 Zr, 1031 Nb, 1032 Mo, 1033 Tc, 1034 Ru, 1035 Rh, 1036 Pd, 1037 Ag, 1038 Cd, 1039 In, 1040 Sn, 1041 Sb, 1042 Te, 1043 I, 1044 Xe, 1045 Rb, 1046 Sr, 1047 Y, 1048 Zr, 1049 Nb, 1050 Mo, 1051 Tc, 1052 Ru, 1053 Rh, 1054 Pd, 1055 Ag, 1056 Cd, 1057 In, 1058 Sn, 1059 Sb, 1060 Te, 1061 I, 1062 Xe, 1063 Rb, 1064 Sr, 1065 Y, 1066 Zr, 1067 Nb, 1068 Mo, 1069 Tc, 1070 Ru, 1071 Rh, 1072 Pd, 1073 Ag, 1074 Cd, 1075 In, 1076 Sn, 1077 Sb, 1078 Te, 1079 I, 1080 Xe, 1081 Rb, 1082 Sr, 1083 Y, 1084 Zr, 1085 Nb, 1086 Mo, 1087 Tc, 1088 Ru, 1089 Rh, 1090 Pd, 1091 Ag, 1092 Cd, 1093 In, 1094 Sn, 1095 Sb, 1096 Te, 1097 I, 1098 Xe, 1099 Rb, 1100 Sr, 1101 Y, 1102 Zr, 1103 Nb, 1104 Mo, 1105 Tc, 1106 Ru, 1107 Rh, 1108 Pd, 1109 Ag, 1110 Cd, 1111 In, 1112 Sn, 1113 Sb, 1114 Te, 1115 I, 1116 Xe, 1117 Rb, 1118 Sr, 1119 Y, 1120 Zr, 1121 Nb, 1122 Mo, 1123 Tc, 1124 Ru, 1125 Rh, 1126 Pd, 1127 Ag, 1128 Cd, 1129 In, 1130 Sn, 1131 Sb, 1132 Te, 1133 I, 1134 Xe, 1135 Rb, 1136 Sr, 1137 Y, 1138 Zr, 1139 Nb, 1140 Mo, 1141 Tc, 1142 Ru, 1143 Rh, 1144 Pd, 1145 Ag, 1146 Cd, 1147 In, 1148 Sn, 1149 Sb, 1150 Te, 1151 I, 1152 Xe, 1153 Rb, 1154 Sr, 1155 Y, 1156 Zr, 1157 Nb, 1158 Mo, 1159 Tc, 1160 Ru, 1161 Rh, 1162 Pd, 1163 Ag, 1164 Cd, 1165 In, 1166 Sn, 1167 Sb, 1168 Te, 1169 I, 1170 Xe, 1171 Rb, 1172 Sr, 1173 Y, 1174 Zr, 1175 Nb, 1176 Mo, 1177 Tc, 1178 Ru, 1179 Rh, 1180 Pd, 1181 Ag, 1182 Cd, 1183 In, 1184 Sn, 1185 Sb, 1186 Te, 1187 I, 1188 Xe, 1189 Rb, 1190 Sr, 1191 Y, 1192 Zr, 1193 Nb, 1194 Mo, 1195 Tc, 1196 Ru, 1197 Rh, 1198 Pd, 1199 Ag, 1200 Cd, 1201 In, 1202 Sn, 1203 Sb, 1204 Te, 1205 I, 1206 Xe, 1207 Rb, 1208 Sr, 1209 Y, 1210 Zr, 1211 Nb, 1212 Mo, 1213 Tc, 1214 Ru, 1215 Rh, 1216 Pd, 1217 Ag, 1218 Cd, 1219 In, 1220 Sn, 1221 Sb, 1222 Te, 1223 I, 1224 Xe, 1225 Rb, 1226 Sr, 1227 Y, 1228 Zr, 1229 Nb, 1230 Mo, 1231 Tc, 1232 Ru, 1233 Rh, 1234 Pd, 1235 Ag, 1236 Cd, 1237 In, 1238 Sn, 1239 Sb, 1240 Te, 1241 I, 1242 Xe, 1243 Rb, 1244 Sr, 1245 Y, 1246 Zr, 1247 Nb, 1248 Mo, 1249 Tc, 1250 Ru, 1251 Rh, 1252 Pd, 1253 Ag, 1254 Cd, 1255 In, 1256 Sn, 1257 Sb, 1258 Te, 1259 I, 1260 Xe, 1261 Rb, 1262 Sr, 1263 Y, 1264 Zr, 1265 Nb, 1266 Mo, 1267 Tc, 1268 Ru, 1269 Rh, 1270 Pd, 1271 Ag, 1272 Cd, 1273 In, 1274 Sn, 1275 Sb, 1276 Te, 1277 I, 1278 Xe, 1279 Rb, 1280 Sr, 1281 Y, 1282 Zr, 1283 Nb, 1284 Mo, 1285 Tc, 1286 Ru, 1287 Rh, 1288 Pd, 1289 Ag, 1290 Cd, 1291 In, 1292 Sn, 1293 Sb, 1294 Te, 1295 I, 1296 Xe, 1297 Rb, 1298 Sr, 1299 Y, 1300 Zr, 1301 Nb, 1302 Mo, 1303 Tc, 1304 Ru, 1305 Rh, 1306 Pd, 1307 Ag, 1308 Cd, 1309 In, 1310 Sn, 1311 Sb, 1312 Te, 1313 I, 1314 Xe, 1315 Rb, 1316 Sr, 1317 Y, 1318 Zr, 1319 Nb, 1320 Mo, 1321 Tc, 1322 Ru, 1323 Rh, 1324 Pd, 1325 Ag, 1326 Cd, 1327 In, 1328 Sn, 1329 Sb, 1330 Te, 1331 I, 1332 Xe, 1333 Rb, 1334 Sr, 1335 Y, 1336 Zr, 1337 Nb, 1338 Mo, 1339 Tc, 1340 Ru, 1341 Rh, 1342 Pd, 1343 Ag, 1344 Cd, 1345 In, 1346 Sn, 1347 Sb, 1348 Te, 1349 I, 1350 Xe, 1351 Rb, 1352 Sr, 1353 Y, 1354 Zr, 1355 Nb, 1356 Mo, 1357 Tc, 1358 Ru, 1359 Rh, 1360 Pd, 1361 Ag, 1362 Cd, 1363 In, 1364 Sn, 1365 Sb, 1366 Te, 1367 I, 1368 Xe, 1369 Rb, 1370 Sr, 1371 Y, 1372 Zr, 1373 Nb, 1374 Mo, 1375 Tc, 1376 Ru, 1377 Rh, 1378 Pd, 1379 Ag, 1380 Cd, 1381 In, 1382 Sn, 1383 Sb, 1384 Te, 1385 I, 1386 Xe, 1387 Rb, 1388 Sr, 1389 Y, 1390 Zr, 1391 Nb, 1392 Mo, 1393 Tc, 1394 Ru, 1395 Rh, 1396 Pd, 1397 Ag, 1398 Cd, 1399 In, 1400 Sn, 1401 Sb, 1402 Te, 1403 I, 1404 Xe, 1405 Rb, 1406 Sr, 1407 Y, 1408 Zr, 1409 Nb, 1410 Mo, 1411 Tc, 1412 Ru, 1413 Rh, 1414 Pd, 1415 Ag, 1416 Cd, 1417 In, 1418 Sn, 1419 Sb, 1420 Te, 1421 I, 1422 Xe, 1423 Rb, 1424 Sr, 1425 Y, 1426 Zr, 1427 Nb, 1428 Mo, 1429 Tc, 1430 Ru, 1431 Rh, 1432 Pd, 1433 Ag, 1434 Cd, 1435 In, 1436 Sn, 1437 Sb, 1438 Te, 1439 I, 1440 Xe, 1441 Rb, 1442 Sr, 1443 Y, 1444 Zr, 1445 Nb, 1446 Mo, 1447 Tc, 1448 Ru, 1449 Rh, 1450 Pd, 1451 Ag, 1452 Cd, 1453 In, 1454 Sn, 1455 Sb, 1456 Te, 1457 I, 1458 Xe, 1459 Rb, 1460 Sr, 1461 Y, 1462 Zr, 1463 Nb, 1464 Mo, 1465 Tc, 1466 Ru, 1467 Rh, 1468 Pd, 1469 Ag, 1470 Cd, 1471 In, 1472 Sn, 1473 Sb, 1474 Te, 1475 I, 1476 Xe, 1477 Rb, 1478 Sr, 1479 Y, 1480 Zr, 1481 Nb, 1482 Mo, 1483 Tc, 1484 Ru, 1485 Rh, 1486 Pd, 1487 Ag, 1488 Cd, 1489 In, 1490 Sn, 1491 Sb, 1492 Te, 1493 I, 1494 Xe, 1495 Rb, 1496 Sr, 1497 Y, 1498 Zr, 1499 Nb, 1500 Mo, 1501 Tc, 1502 Ru, 1503 Rh, 1504 Pd, 1505 Ag, 1506 Cd, 1507 In, 1508 Sn, 1509 Sb, 1510 Te, 1511 I, 1512 Xe, 1513 Rb, 1514 Sr, 1515 Y, 1516 Zr, 1517 Nb, 1518 Mo, 1519 Tc, 1520 Ru, 1521 Rh, 1522 Pd, 1523 Ag, 1524 Cd, 1525 In, 1526 Sn, 1527 Sb, 1528 Te, 1529 I, 1530 Xe, 1531 Rb, 1532 Sr, 1533 Y, 1534 Zr, 1535 Nb, 1536 Mo, 1537 Tc, 1538 Ru, 1539 Rh, 1540 Pd, 1541 Ag, 1542 Cd, 1543 In, 1544 Sn, 1545 Sb, 1546 Te, 1547 I, 1548 Xe, 1549 Rb, 1550 Sr, 1551 Y, 1552 Zr, 1553 Nb, 1554 Mo, 1555 Tc, 1556 Ru, 1557 Rh, 1558 Pd, 1559 Ag, 1560 Cd, 1561 In, 1562 Sn, 1563 Sb, 1564 Te, 1565 I, 1566 Xe, 1567 Rb, 1568 Sr, 1569 Y, 1570 Zr, 1571 Nb, 1572 Mo, 1573 Tc, 1574 Ru, 1575 Rh, 1576 Pd, 1577 Ag, 1578 Cd, 1579 In, 1580 Sn, 1581 Sb, 1582 Te, 1583 I, 1584 Xe, 1585 Rb, 1586 Sr, 1587 Y, 1588 Zr, 1589 Nb, 1590 Mo, 1591 Tc, 1592 Ru, 1593 Rh, 1594 Pd, 1595 Ag, 1596 Cd, 1597 In, 1598 Sn, 1599 Sb, 1600 Te, 1601 I, 1602 Xe, 1603 Rb, 1604 Sr, 1605 Y, 1606 Zr, 1607 Nb, 1608 Mo, 1609 Tc, 1610 Ru, 1611 Rh, 1612 Pd, 1613 Ag, 1614 Cd, 1615 In, 1616 Sn, 1617 Sb, 1618 Te, 1619 I, 1620 Xe, 1621 Rb, 1622 Sr, 1623 Y, 1624 Zr, 1625 Nb, 1626 Mo, 1627 Tc, 1628 Ru, 1629 Rh, 1630 Pd, 1631 Ag, 1632 Cd, 1633 In, 1634 Sn, 1635 Sb, 1636 Te, 1637 I, 1638 Xe, 1639 Rb, 1640 Sr, 1641 Y, 1642 Zr, 1643 Nb, 1644 Mo, 1645 Tc, 1646 Ru, 1647 Rh, 1648 Pd, 1649 Ag, 1650 Cd, 1651 In, 1652 Sn, 1653 Sb, 1654 Te, 1655 I, 1656 Xe, 1657 Rb, 1658 Sr, 1659 Y, 1660 Zr, 1661 Nb, 1662 Mo, 1663 Tc, 1664 Ru, 1665 Rh, 1666 Pd, 1667 Ag, 1668 Cd, 1669 In, 1670 Sn, 1671 Sb, 1672 Te, 1673 I, 1674 Xe, 1675 Rb, 1676 Sr, 1677 Y, 1678 Zr, 1679 Nb, 1680 Mo, 1681 Tc, 1682 Ru, 1683 Rh, 1684 Pd, 1685 Ag, 1686 Cd, 1687 In, 1688 Sn, 1689 Sb, 1690 Te, 1691 I, 1692 Xe, 1693 Rb, 1694 Sr, 1695 Y, 1696 Zr, 1697 Nb, 1698 Mo, 1699 Tc, 1700 Ru, 1701 Rh, 1702 Pd, 1703 Ag, 1704 Cd, 1705 In, 1706 Sn, 1707 Sb, 1708 Te, 1709 I, 1710 Xe, 1711 Rb, 1712 Sr, 1713 Y, 1714 Zr, 1715 Nb, 1716 Mo, 1717 Tc, 1718 Ru, 1719 Rh, 1720 Pd, 1721 Ag, 1722 Cd, 1723 In, 1724 Sn, 1725 Sb, 1726 Te, 1727 I, 1728 Xe, 1729 Rb, 1730 Sr, 1731 Y, 1732 Zr, 1733 Nb, 1734 Mo, 1735 Tc, 1736 Ru, 1737 Rh, 1738 Pd, 1739 Ag, 1740 Cd, 1741 In, 1742 Sn, 1743 Sb, 1744 Te, 1745 I, 1746 Xe, 1747 Rb, 1748 Sr, 1749 Y, 1750 Zr, 1751 Nb, 1752 Mo, 1753 Tc, 1754 Ru, 1755 Rh, 1756 Pd, 1757 Ag, 1758 Cd, 1759 In, 1760 Sn, 1761 Sb, 1762 Te, 1763 I, 1764 Xe, 1765 Rb, 1766 Sr, 1767 Y, 1768 Zr, 1769 Nb, 1770 Mo, 1771 Tc, 1772 Ru, 1773 Rh, 1774 Pd, 1775 Ag, 1776 Cd, 1777 In, 1778 Sn, 1779 Sb, 1780 Te, 1781 I, 1782 Xe, 1783 Rb, 1784 Sr, 1785 Y, 1786 Zr, 1787 Nb, 1788 Mo, 1789 Tc, 1790 Ru, 1791 Rh, 1792 Pd, 1793 Ag, 1794 Cd, 1795 In, 1796 Sn, 1797 Sb, 1798 Te, 1799 I, 1800 Xe, 1801 Rb, 1802 Sr, 1803 Y, 1804 Zr, 1805 Nb, 1806 Mo, 1807 Tc, 1808 Ru, 1809 Rh, 1810 Pd, 1811 Ag, 1812 Cd, 1813 In, 1814 Sn, 1815 Sb, 1816

relativistic effects and inclusion of the 4f electron shell. Electrons filling the 4f shell only partially shield the nuclear charge, leading to the contraction of the 5p, 5d and 6s shells. The decrease in atomic radii from La to Lu serves as an example.⁶⁻⁹

The majority of theoretical calculations assume that the speed of light, c , is infinite; a valid assumption for particles whose speeds are significantly less than c . However, this nonrelativistic approximation does not hold for heavier systems. The increase in nuclear charge has a pronounced effect on electron velocities, especially for s -orbitals. As speed increases (approaching the speed of light for the heaviest elements), radii decrease, and orbital energies are lowered. This orbital contraction shields the nuclear charge from the valence electrons, leading to ionization energies, bond energies, and orbital energies that do not follow trends that have been established for lighter atoms.^{6,8}

Spin-orbit (SO) coupling is a relativistic effect⁶⁻¹⁰ that refers to the interaction between the orbital angular momentum, \vec{l} , and spin angular momentum, \vec{s} , of an electron. In the relativistic regime, \vec{l} and \vec{s} cease to be good quantum numbers; however, the vector sum, $\vec{j} = \vec{l} + \vec{s}$, has good quantum numbers. SO coupling can result in large energy differences between SO states and singlet-triplet transitions. Consequently, potential energy surfaces often exhibit shapes due to avoided crossings between SO states.

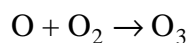
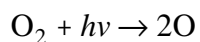
A comparison of the molecular and spectroscopic properties inherent to a specific group in the periodic table can raise stimulating questions. The members of a group have the same valence electron configuration, thus certain similarities are assumed. Yet, the

nuclei get heavier moving down the group. Does the addition of another electronic shell affect these properties? Do relativistic effects begin to dominate? Are these effects manifest in theoretical and experimental studies?

The group-V hydrides, NH_3 , PH_3 , AsH_3 , SbH_3 , and BiH_3 are an excellent test case. The lightest group-V hydride, NH_3 , has enjoyed considerable experimental and theoretical attention. Consequently, the molecular and spectroscopic properties of NH_3 are well characterized. In contrast, the heavier group-V hydrides have received much less attention. From what little is known, the photochemistry of the heavier members exhibit marked differences in comparison to their lighter counterparts. These molecules are readily available via commercial or synthetic routes, thus an in-depth experimental study of the group-V hydrides is feasible and would help explain these differences. The photochemistry of the group-V hydrides is discussed at length in chapter 3 of this dissertation.

1.2 Photodissociation Dynamics

Photodissociation processes are important in many diverse areas of chemistry (*e.g.* atmospheric chemistry, physical chemistry, biochemistry, etc).¹¹⁻¹⁵ For example, photodissociation plays a vital role in the production of ozone, which protects the earth from harmful ultraviolet radiation from the sun:



However, the photodissociation of pollutants in the atmosphere, *i.e.* chlorofluorocarbons, sulfur oxides and nitrogen oxides, is responsible for acid rain and global air pollution. Photodissociation processes have also led to important advances in laser technology (*e.g.* chemical lasers) and have expanded our understanding of chemical reaction dynamics.^{11,13}

The ultimate goal in studying photodissociation dynamics is a detailed understanding of how a molecule falls apart after absorption of a photon. In photodissociation experiments, a photon prepares a molecule in an excited state where dissociation occurs *via* direct or indirect pathways.^{11,12} The excitation step can be considered “instantaneous” compared to the time scale for nuclear motion. As a result, the molecule “lands” on the excited potential energy surface (PES) with its ground state equilibrium geometry initially preserved. Excitation to a repulsive PES leads to direct dissociation. In contrast, indirect photodissociation occurs when the parent molecule is trapped for some time on the excited PES. If a potential barrier is to blame, dissociation can proceed *via* tunneling or internal vibrational energy redistribution (IVR). If the excited PES is bound, the excited state can decay *via* a transition to a repulsive PES (electronic predissociation) or to a highly excited continuum level of the ground state located above the ground state’s dissociation threshold.¹¹⁻¹³ A schematic of direct and indirect photodissociation is presented in Figure 1.2 and 1.3, respectively.

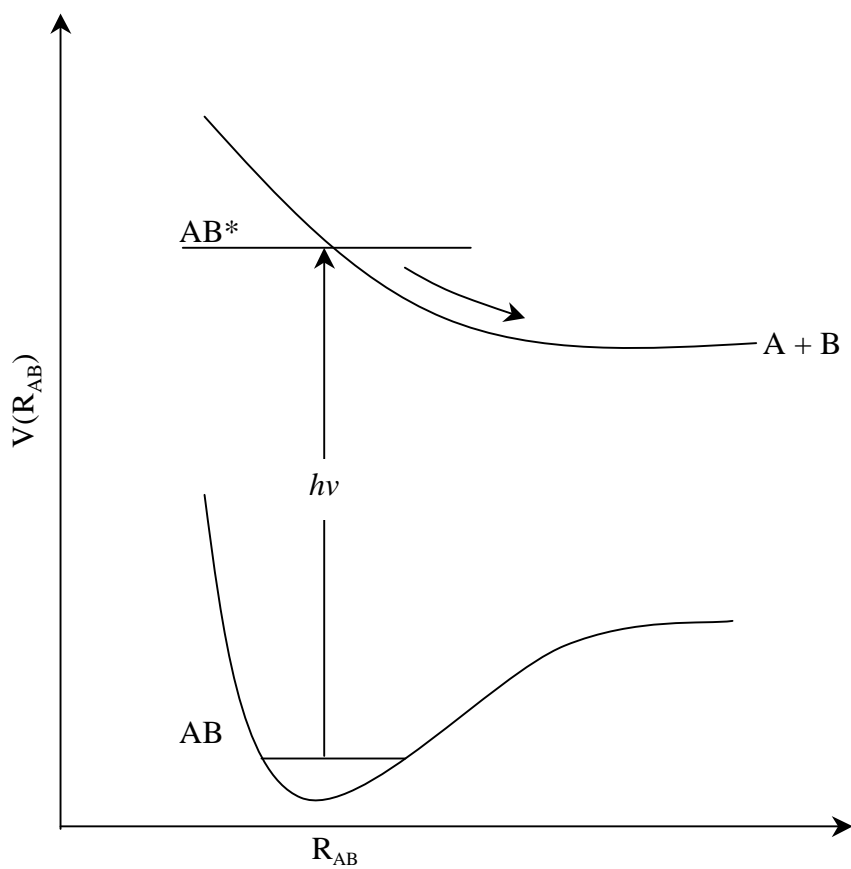


Figure 1.2 Illustration of direct dissociation (adapted from reference 11): $AB + h\nu \rightarrow AB^* \rightarrow A + B$. AB^* is the photoexcited complex and R_{AB} represents the internuclear distance between A and B.

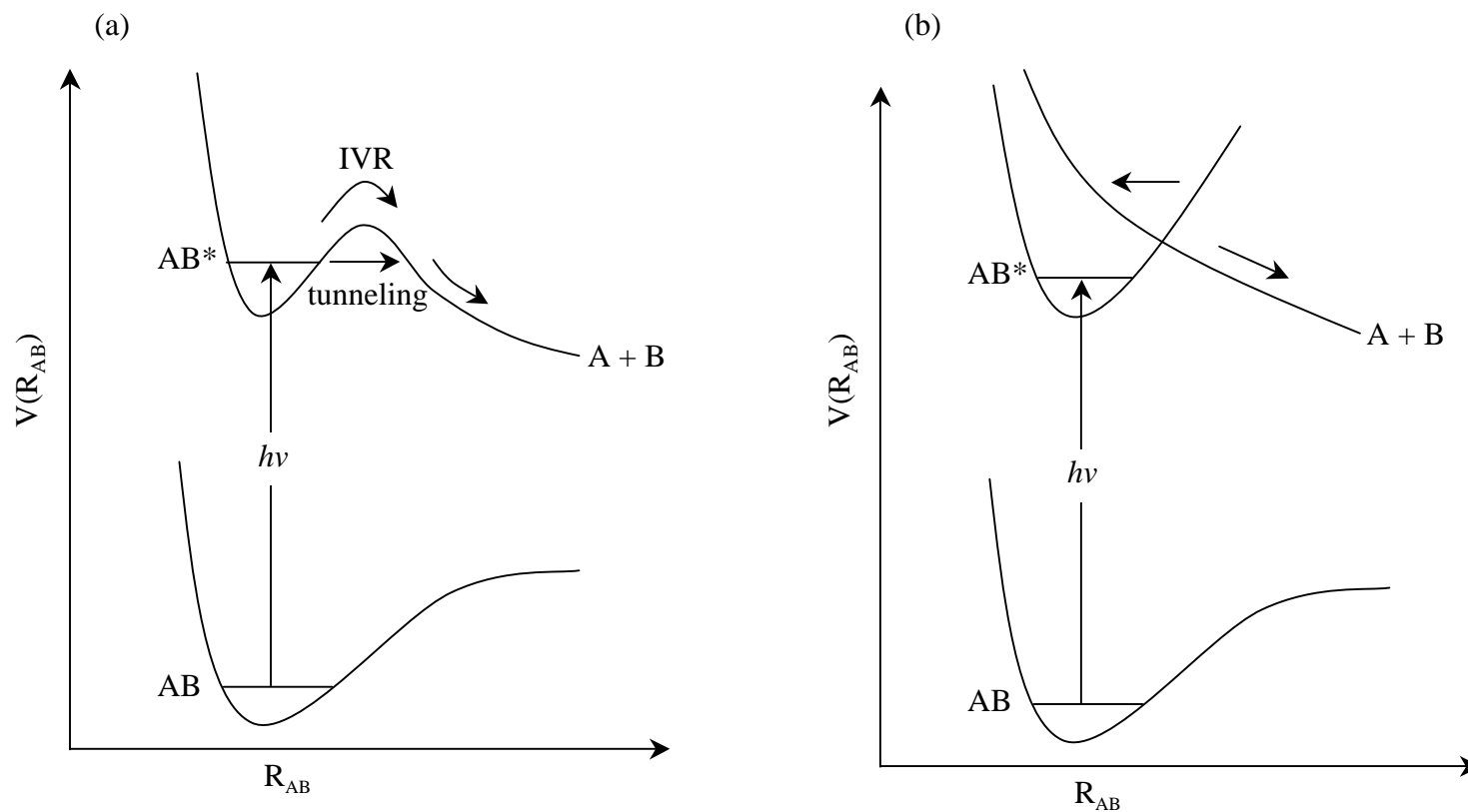


Figure 1.3 Illustration of indirect photodissociation (adapted from reference 11). AB* is the photoexcited complex and R_{AB} represents the internuclear distance between A and B. (a) AB* dissociates *via* IVR or tunneling. (b) AB* dissociates *via* a transition from a bound electronic state to a repulsive electronic state.

1.2.1 Experimental Approaches

Recent improvements in laser technology, molecular beam techniques and detection schemes have yielded sophisticated photodissociation experiments.^{11,13,15-17} Experimentalists are able to excite molecules to zero-order quantum states, as well as define the angular momentum and total energy. Thus, photodissociation experiments are ideally suited to study chemical reaction dynamics. Insight into: (1) the Franck-Condon region accessed during the excitation step, (2) the lifetime of the parent molecule in the excited state, (3) the chemical bonds broken after photoabsorption, (4) the identity of the products, (5) the branching ratio for the possible reaction channels, and (6) the distribution of energy over the various degrees of freedom (translational, electronic, vibrational, rotational) of the products, all provide clues to the molecular motion during dissociation.^{11, 13, 15-17} These clues help validate or question the approximations (*e.g.* Born-Oppenheimer) used in calculating PESs.¹¹⁻¹³

Photodissociation experiments can also yield information about the vector properties of the photofragments.^{11,12,18-20} Anisotropy measurements can yield information regarding the symmetry of the transition, as well as the time scale for dissociation. This is achieved through the use of polarized laser radiation. The maximum probability for excitation occurs when the transition dipole moment, $\bar{\mu}$, of the parent molecule is oriented parallel to the electric vector, $\bar{\epsilon}$, of the photolysis radiation (*i.e.* $P = |\bar{\mu} \cdot \bar{\epsilon}|^2$). The angular distribution of the products' recoil velocity, \bar{v} , relative to $\bar{\epsilon}$ (and consequently, $\bar{\mu}$) is given by:

$$f(\theta) = \frac{1}{4\pi} (1 + \beta P_2(\cos\theta)) \quad (1)$$

where β is the anisotropy parameter, $P_2(\cos\theta)$ is the second-order Legendre polynomial and θ is the angle between \bar{v} and $\bar{\epsilon}$. β can assume values between 2 and -1, corresponding to parallel and perpendicular transitions, respectively. The alignment of the photofragments can also be determined by measuring the correlations between the product angular momentum vector, \bar{J} , relative to $\bar{\epsilon}$ and \bar{v} , $\bar{J} - \bar{\epsilon}$ and $\bar{J} - \bar{v}$, respectively.¹⁸⁻²⁰

There are numerous experimental methods designed to study photodissociation dynamics. Laser-induced fluorescence (LIF), multiphoton ionization (MPI), resonantly enhanced MPI (REMPI), Doppler spectroscopy, time-of-flight (TOF) spectroscopy, and velocity map imaging are a few experimental techniques that measure product state and angular distributions.¹²⁻¹⁸ Advanced pump-probe experiments using femtosecond laser pulses have been used to directly observe dissociation in real-time, as well.^{17,21,22} A more exhaustive list of photodissociation experimental methods can be found in several review articles.^{13-15,20}

The experimental results presented in this dissertation were obtained using high- n Rydberg hydrogen time-of-flight spectroscopy (HRTOF), a specific type of TOF spectroscopy. HRTOF is discussed in more detail in chapter 2.

1.2.2 Theoretical Approaches

Advances in the field of photodissociation dynamics result from the collaboration between theoreticians and experimentalists. Theoretical calculations provide high quality potential energy curves or surfaces (for diatomics or polyatomics, respectively). PESs can be displayed as contour maps of chemical reactions and are useful tools when studying interatomic forces along reaction coordinates. The topography of the PESs (*e.g.* the presence of potential wells, barriers, avoided crossings, etc.) can help reconcile branching ratios and product state distributions obtained from experiment.^{11,23,24}

The PES for a molecule containing N atoms is a function of $3N - 6$ independent variables (*i.e.* the internuclear internal coordinates).^{11,24} Clearly, the computational cost is significant for large molecules! In order to simplify the calculations required to generate PESs, the Born-Oppenheimer (BO) approximation is invoked. This is an adiabatic approximation that separates the nuclear and electronic degrees of freedom based on the large difference between the masses (and subsequent velocities) of the electrons and nuclei.

Born-Oppenheimer Approximation

The BO approximation assumes that electrons can instantaneously adjust to nuclear motion.²⁴ The nuclei are assumed to be stationary and do not contribute to the total Hamiltonian. Thus, an electronic Hamiltonian can be written as follows:

$$H^{el} = T_e + V_{ee} + V_{nn} + V_{en} \quad (2)$$

where T_e is the kinetic energy of the electrons and V_{ee} , V_{nn} and V_{en} are the Coulomb potentials for the electron-electron, nuclei-nuclei and electron-nuclei interactions, respectively. The kinetic energy and Coulomb terms are expanded below:

$$T_e = -\sum_i \frac{\hbar^2}{2m_e} \nabla_i^2 \quad (3)$$

$$V_{ee} = \frac{1}{2} \sum_{ij} \frac{1}{|r_{ij}|} \quad (4)$$

$$V_{nn} = \frac{1}{2} \sum_{ab} \frac{Z_a Z_b}{|R_{ab}|} \quad (5)$$

$$V_{en} = -\sum_i \sum_a \frac{Z_a}{|r_i - R_a|} \quad (6)$$

where r and R represent the electron and nuclear coordinates, respectively. Notice that the nuclear kinetic energy term, T_n :

$$T_n = -\sum_a \frac{\hbar^2}{M_a} \nabla_a^2$$

is absent. The non-relativistic, electronic Schrödinger equation can then be solved for fixed positions of the nuclei:

$$H^{el} \phi_i^{el}(r; R) = U_i(R) \phi_i^{el}(r; R) \quad (7)$$

where H^{el} denotes the electronic Hamiltonian, $\phi_i^{el}(r; R)$ is the i^{th} eigenfunction with eigenenergy, U_i , and r and R represent the electron and nuclear coordinates, respectively. Each electronic wave function, $\phi_i^{el}(r; R)$, depends parametrically on the nuclear coordinates and corresponds to a specific electronic energy, *i.e.* each electronic

configuration gives rise to a specific adiabatic PES, U_i . The kinetic energy of the nuclei has no effect on the electronic wavefunctions; thus, molecular motion is restricted to a single PES and transitions between adiabatic surfaces are forbidden.²⁴

Breakdown of the Born-Oppenheimer Approximation

In reality, the nuclear motion cannot be discounted. The total wavefunction can be expanded in terms of the electronic wavefunctions obtained by using the BO approximation:

$$\Phi_j = \sum_i \phi_i^{el}(r; R) \chi_i(R) \quad (8)$$

where the nuclear functions, $\chi_i(R)$, are expansion coefficients. Substitution of Φ_j into the total Hamiltonian, $H = H^{el} + T_n$, yields:

$$(H_{el} + T_n) \sum_i \phi_i^{el}(r; R) \chi_i(R) = E_j \sum_i \phi_i^{el}(r; R) \chi_i(R) \quad (9)$$

Lastly, multiplication by ϕ_k^{el} followed by integration over the electronic coordinates results in:

$$\left(T_n + U_k(R) - E_j \right) \chi_k^i = \sum_{ja} \frac{1}{2m_a} \left[\langle \phi_k | \nabla_a^2 \phi_i \rangle \chi_i^j + 2 \langle \phi_k | \nabla_a \phi_i \rangle \nabla_a \chi_i^j \right] \quad (10)$$

The right side of equation 10 represents the nonadiabatic coupling terms. If these terms are set to zero, equation 10 describes the nuclear motion on the BO potential energy surfaces. If the right side is nonzero, nuclear motion no longer evolves on a single PES.

The term, $\langle \phi_k | \nabla_a \phi_i \rangle \nabla_a \chi_i^j$, is primarily responsible for nonadiabatic interactions.²⁴⁻²⁶ The matrix element, $\langle \phi_k | \nabla_a \phi_i \rangle$, corresponds to the change in the

electronic wavefunction on the k^{th} PES and is significant for regions where the electronic wavefunction depends strongly on the nuclear geometry. The coupling term, $\langle \phi_k | \nabla_a \phi_i \rangle \nabla_a \chi_i^j$, is velocity dependent due to the nuclear momentum, $\nabla_a \chi_j^i$. When nuclear motion approaches the time scale of electronic motion, the nuclear and electronic degrees of freedom can couple and the BO approximation breaks down. Coupling is allowed between adiabatic surfaces and nonadiabatic transitions can occur, especially in regions where the adiabats are near degenerate.

Nonadiabatic coupling between PESs results in exciting chemistry. Of interest in this dissertation is the coupling between two PESs of the same symmetry. Consider the ground, \tilde{X}^1A_1 , and first excited, \tilde{A}^1A_2'' , electronic states of NH_3 . For planar geometries ($\theta = 90^\circ$, where θ is the angle between a NH bond and the normal to the trigonal plane), the \tilde{X} and \tilde{A} states of NH_3 correlate to $\text{NH}_2(\tilde{A}^2A_1)$ and $\text{NH}_2(\tilde{X}^2B_1)$, respectively. At nonplanar geometries ($\theta \neq 90^\circ$), the \tilde{X} and \tilde{A} states have the same 1A symmetry and an avoided crossing results. Consequently, $\text{NH}_3(\tilde{X})$ correlates adiabatically to $\text{NH}_2(\tilde{X})$ whereas $\text{NH}_3(\tilde{A})$ correlates adiabatically to $\text{NH}_2(\tilde{A})$.²⁷

The intersection between $\text{NH}_3(\tilde{X})$ and $\text{NH}_3(\tilde{A})$ is an example of a conical intersection. A conical intersection is an efficient “molecular funnel” that can facilitate nonadiabatic transitions between PESs of the same symmetry. The topology of a conical intersection is represented by a double cone.^{28,29} However, the point of intersection is a seam with dimension $N^{\text{int}} - 2$, where N^{int} is the number of the internal degrees of freedom. It should be noted that relativistic effects, namely spin-orbit interaction, can alter the

dimensionality of this seam.^{28,29} Conical intersections are also subject to the geometric phase effect, which refers to the electronic wavefunction's change in sign after traveling around a conical intersection. For a more rigorous description of conical intersections, see the reviews by Yarkony.^{28,29}

The presence of a conical intersection along the reaction coordinate can result in transitions between upper and lower electronic states, as well as surprising product branching ratios and quantum state distributions. The conical intersections between the ground and first electronic states of NH_3 , PH_3 and AsH_3 have a profound effect on the photodissociation dynamics and are discussed in Chapter 3.

Diabatic Representation

The diabatic representation provides another perspective of the nuclear dynamics. The nonadiabatic coupling terms (refer to equation 10) are singular at a point of conical intersection, which leads to computational difficulties in the adiabatic representation. In general, the electronic wavefunctions in the diabatic representation are expanded in such a way as to eliminate the derivative coupling terms.^{24,30,31} Diabatic potential energy surfaces can cross and nuclear motion evolves on a single diabat. Transitions can occur due to non-diagonal matrix elements (*i.e.* the potential energy terms) of the Hamiltonian in the basis of diabatic states. Figure 1.4 shows the adiabatic and diabatic surfaces of NH_3 .

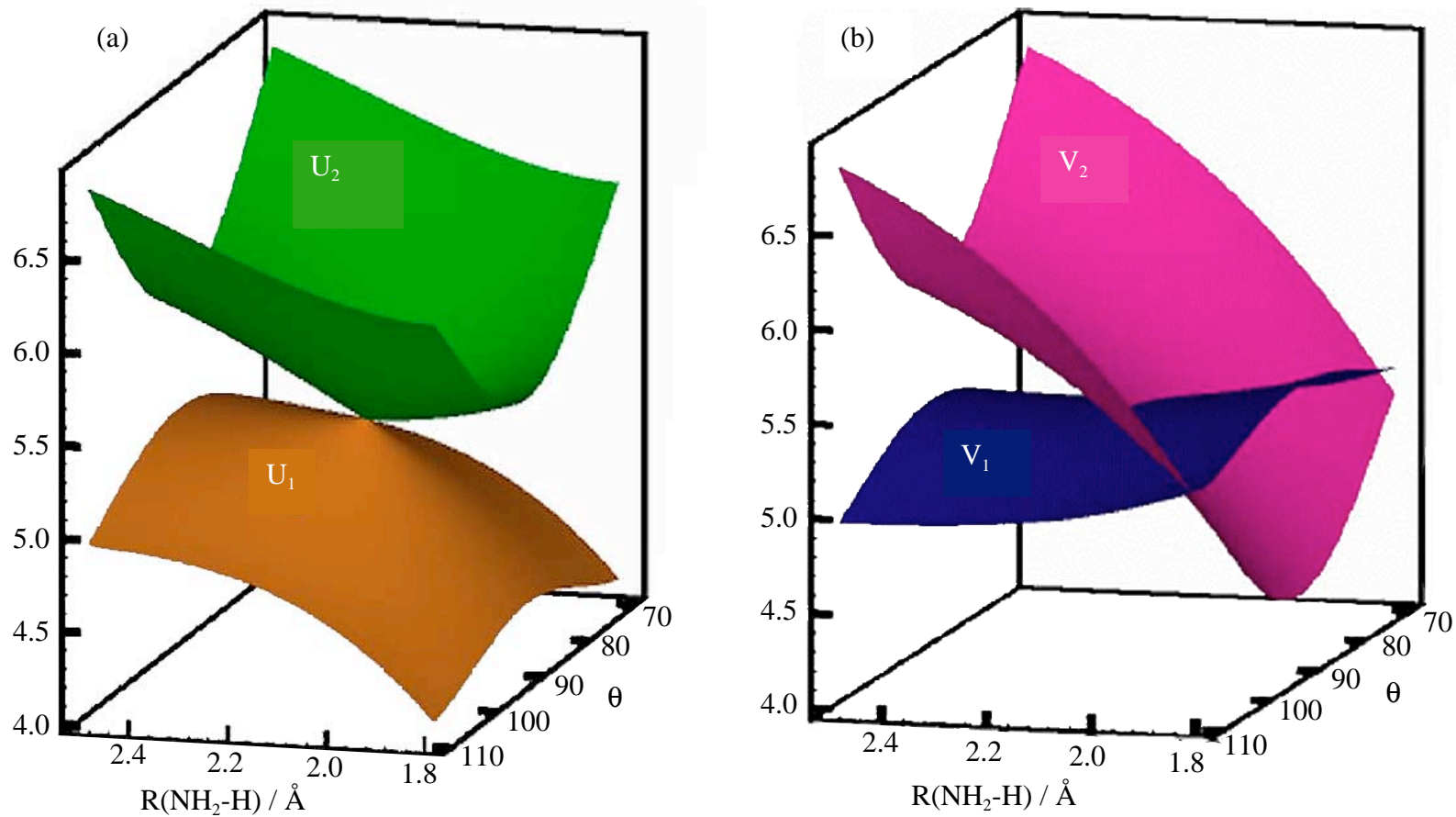


Figure 1.4 (a) Adiabatic (U_1 , U_2) and (b) diabatic (V_1 , V_2) potential energy surfaces of NH₃. θ is the angle between a NH bond and the normal to the trigonal plane ($\theta = 90^\circ$ represents a planar geometry). Note the presence of a conical intersection between the adiabatic PESs at $\theta = 90^\circ$ and $R = 2.13 \text{ \AA}$.²⁷

1.3 Relativistic Calculations

Theoretical calculations become increasingly complex for large systems. The number of electrons, electron-correlation and relativistic effects can be daunting. There are numerous theoretical strategies designed to handle large molecules and relativistic effects.^{8,9,24} Most *ab initio* relativistic calculations rely on frozen core techniques, which replace core electrons with a relativistic effective core potential (RECP).¹⁰ The valence electrons are considered the most important insofar as molecular formation and are treated explicitly. This method has enjoyed considerable success and enables relativistic, core-valence (*e.g.* the penetration of valence electrons in the core region) and electron correlation effects to be treated simultaneously. Other methods consider all the electrons, such as the one-center Dirac-Fock expansion of Desclaux and Pyykkö.⁸ This method is applicable to diatomic hydrides and treats only those electrons centered on the heavy atom.

The Schrödinger equation is unsuitable for relativistic calculations as it does not treat spatial and temporal coordinates equally (the time and spatial coordinates use first and second partial derivatives, respectively).^{9,32} Also, the kinetic energy terms implicit in the Schrödinger equation do not include the particle's velocity with respect to c . The Dirac equation is applicable for relativistic systems.

The Dirac equation for a free particle in the absence of an external field can be written as follows:

$$i\hbar \frac{\partial}{\partial t} \psi = h_D \psi \quad (11)$$

$$h_D = c\alpha \cdot p + \beta m_0 c^2 = \frac{\hbar}{i} c\alpha \cdot \nabla + \beta m_0 c^2 \quad (12)$$

where h_D is the Dirac Hamiltonian, p is the momentum operator, m_0 is the stationary mass, α and β are $N \times N$ matrices ($N \geq 4$) and the wavefunction, ψ , is a N -component column vector. The quantity $\alpha \cdot p$ is explicitly given as:

$$\alpha \cdot p = \frac{\hbar}{i} \left(\alpha_x \frac{\partial}{\partial x} + \alpha_y \frac{\partial}{\partial y} + \alpha_z \frac{\partial}{\partial z} \right) \quad (13)$$

The coefficients α and β can take numerous representations, but must follow the following requirements:

- (1) Hermitian : $\alpha^\dagger = \alpha$, $\beta^\dagger = \beta$
- (2) anticommute: $\alpha_i \alpha_j + \alpha_j \alpha_i = 2\delta_{ij}$
 $\alpha_i \beta = -\beta \alpha_i$
 $(\alpha_i)^2 = \beta^2 = I_{N \times N}$

One representation of the α and β matrices is:

$$\alpha_i = \begin{bmatrix} 0 & \sigma_i \\ \sigma_i & 0 \end{bmatrix}, \beta = \begin{bmatrix} I & 0 \\ 0 & I \end{bmatrix}$$

where σ_i are the 2×2 Pauli matrices and I is the 2×2 unit matrix.³²

The Breit-Pauli Hamiltonian includes relativistic effects *via* a perturbative approach.⁹ The Breit-Pauli Hamiltonian for a multielectron system is:

$$H_{BP} = H_0 + H_D + H_{MV} + H_{SO} \quad (14)$$

H_0 = nonrelativistic Hamiltonian

$$H_D(\text{Darwin}) = \frac{\alpha}{8} (\nabla^2 V) = \frac{\alpha}{8} \left[\nabla^2 \left(-Z \sum_i \frac{1}{r_i} + \sum_{i < j} \frac{1}{r_{ij}} \right) \right]$$

$$H_{MV}(\text{mass-velocity}) = -\frac{\alpha}{8} \sum_i p_i^4$$

$$H_{SO}(\text{spin orbit}) = \left[\sum_i \frac{Z}{r_i^3} (L_i \cdot S_i) + \sum_{i \neq j} \frac{1}{r_{ij}^3} (r_{ij} \times P_i) \cdot (S_i + 2S_j) \right]$$

where α is the fine-structure constant. A more in-depth description of the Dirac equation, the Breit-Pauli Hamiltonian and other relativistic theoretical models can be found in a number of textbooks and review articles on relativistic quantum chemistry.^{7-9,32}

1.3.1 Potential Energy Surfaces and Relativity

The inclusion of spin-orbit coupling can lead to dramatic changes in the PESs. Consider the case of the two heaviest group-V diatomic hydrides, SbH and BiH. The SO splittings for the ground state, ($^3\Sigma_{0+}^- - ^3\Sigma_1^-$), of SbH and BiH are 655 cm⁻¹ and 4917 cm⁻¹, respectively.¹⁰ The ground electronic state of SbH has been calculated as a mixture of 92% $^3\Sigma_{0+}^-(\sigma^2\pi^2)$ and 3% $^1\Sigma_{0+}^+(\sigma^2\pi^2)$ at its equilibrium geometry, $R_{\text{SbH}} = 1.72 \text{ \AA}$, whereas the ground state of BiH is comprised of 76% $^3\Sigma_{0+}^-(\sigma^2\pi^2)$ and 16% $^1\Sigma_{0+}^+(\sigma^2\pi^2)$ at $R_{\text{BiH}} = 1.81 \text{ \AA}$.¹⁰ The X state of BiH at $R_{\text{BiH}} = 3.2 \text{ \AA}$ becomes¹⁰:

$$\begin{aligned} &54\% \ ^3\Sigma_{0+}^-(\sigma^2\pi^2), 12\% \ ^1\Sigma_{0+}^+(\sigma^2\pi^2), 14\% \ ^3\Sigma_{0+}^-(\sigma^{*2}\pi^2), 3\% \ ^1\Sigma_{0+}^+(\sigma^{*2}\pi^2), \\ &6\% \ ^3\Pi_{0+}(\sigma^2\sigma^*\pi), 5\% \ ^3\Sigma_{0+}^-(\sigma\alpha\sigma^*\alpha\pi_x\beta\pi_y\beta - \sigma\beta\alpha^*\beta\pi_x\alpha\pi_y\alpha) \end{aligned}$$

Clearly SO coupling leads to interesting electronic states.

SO coupling splits the electronic states of SbH and BiH into relativistic, Ω , states, where $\Omega = |\Lambda + S|$. Λ denotes the angular momentum along the internuclear axis

and S is the spin angular momentum. The $^3\Sigma^-$ and $^1\Delta$ electronic states of SbH and BiH form 0^+ , 1 and 2 relativistic states, respectively; whereas, the $^1\Sigma^+$ and $^5\Sigma^-$ states form 0^+ , and 0^- , 1, 2 relativistic states, respectively. The PESs for SbH and BiH with and without SO coupling are shown in Figure 1.5 and 1.6, respectively.

1.4 Group-V Hydrides

The group-V hydrides, NH_3 , PH_3 , AsH_3 , SbH_3 and BiH_3 provide an excellent opportunity to study trends. There is a great deal of theoretical and experimental research on NH_3 , resulting in high-quality PESs and a consensus regarding the dynamics on the lowest excited surfaces.³³⁻³⁸ The conical intersection between the ground and first excited electronic states results in competition between nonadiabatic and adiabatic dissociation. The topography surrounding the conical intersection has also been shown to directly influence product state distributions.³²⁻³⁷

The heavier group-V hydrides have received much less attention. The progression toward heavier group-V hydrides becomes arduous for experimental and theoretical research. Toxicity becomes an issue and the large number of electrons complicates calculations. Comparisons between the equilibrium geometries of the \tilde{X} and \tilde{A} states of NH_3/NH_2 , PH_3/PH_2 and $\text{AsH}_3/\text{AsH}_2$ reveal important differences that are manifest in the photodissociation dynamics.^{39,40} AsH_3 lies intermediate between the nonrelativistic and relativistic regimes. Will relativistic effects influence the photodissociation dynamics of the heaviest group-V members, SbH_3 and BiH_3 ?

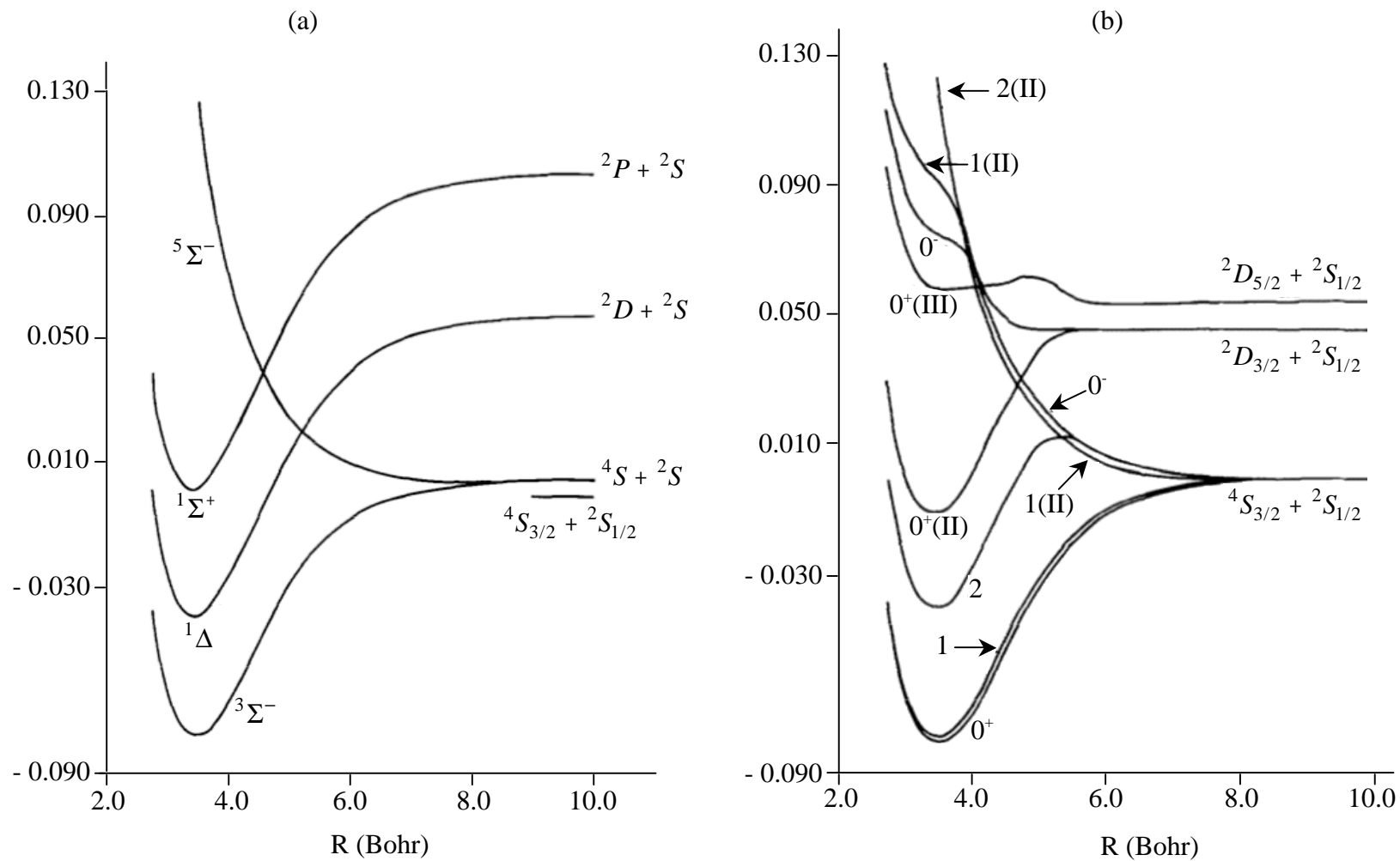


Figure 1.5 Potential energy curves for SbH (a) without SO coupling and (b) with SO coupling.¹⁰

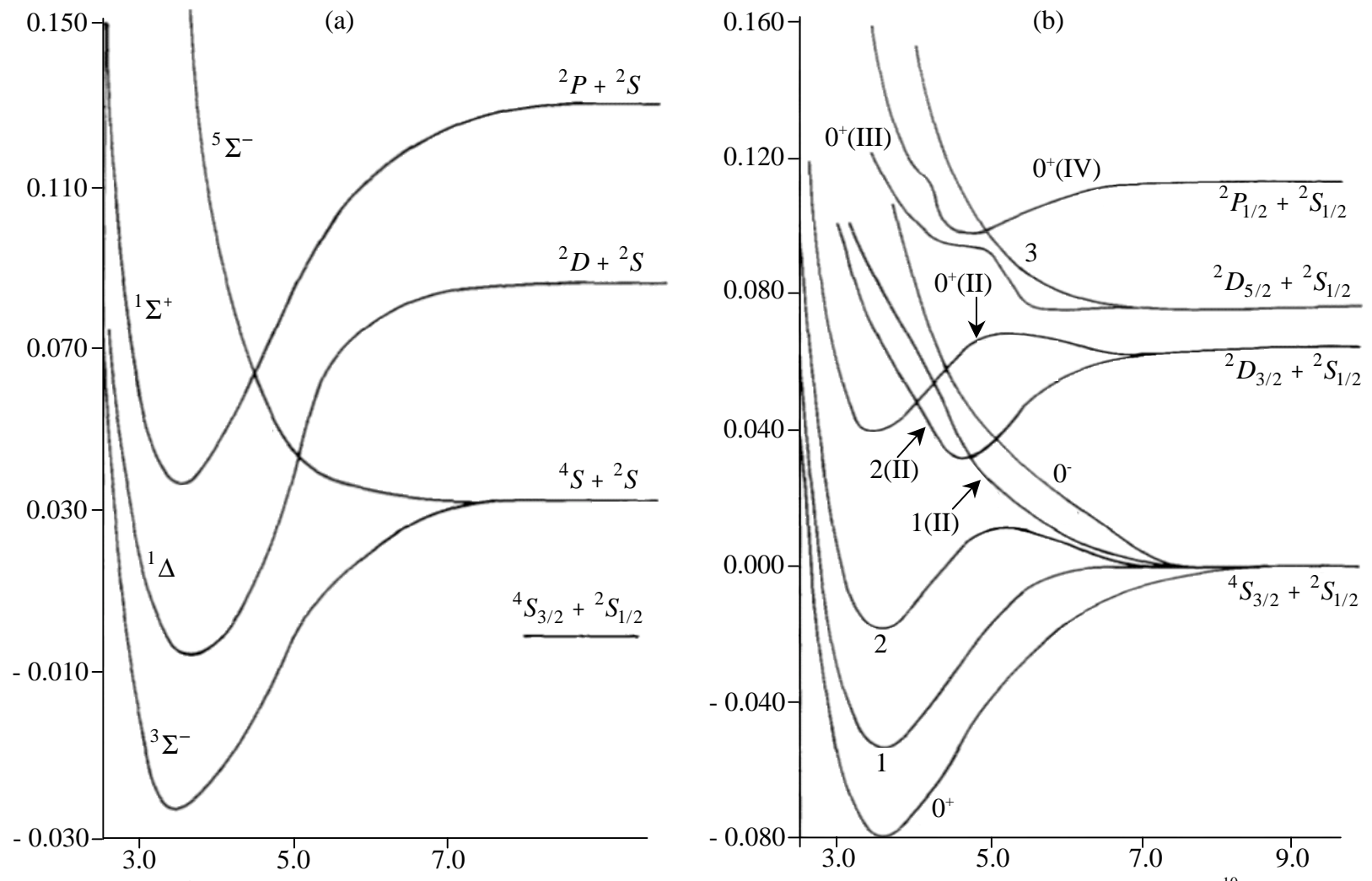


Figure 1.6 Potential energy curves of BiH (a) without SO coupling and (b) with SO coupling.¹⁰

Chapter 2 details HRTOF spectroscopy. Chapter 3 describes experiments on the ultraviolet photodissociation of AsH₃. Chapter 4 suggests additional experiments on AsH₃ that will, perhaps, result in a better understanding of its photochemistry. Preliminary experimental results regarding the photodissociation of SbH₃ are also discussed, as well as some thoughts on BiH₃.

1.5 Chapter 1 References

1. Scerri, E. R. *The Periodic Table: Its Story and its Significance*; Oxford University Press: Oxford, 2007.
2. Greenwood, N. N.; Earnshaw, A. *Chemistry of the Elements*; Reed Educational and Professional Publishing: Oxford, 1997.
3. Oxtoby, D. W.; Gillis, H. P.; Nachtrieb, N. H. *Principles of Modern Chemistry*; Thomson Learning, Inc.: Ontario, 2002.
4. Zumdahl, S. S.; Zumdahl, S. A. *Chemistry*; Houghton Mifflin Company: New York, 2007.
5. Rich, R. *Periodic Correlations*; W. A. Benjamin: New York, 1965.
6. Pitzer, K. S. *Acc. Chem. Res.* **1979**, *12*, 271.
7. Christiansen, P. A.; Ermler, W. C.; Pitzer, K. S. *Annu. Rev. Phys. Chem.* **1985**, *36*, 407.
8. Pyykkö, P.; Desclaux, J.-P. *Acc. Chem. Res.* **1979**, *12*, 276.
9. Balasubramanian, K. *Relativistic Effects in Chemistry, Part A*; John Wiley & Sons, Inc: New York, 1997.
10. Balasubramanian, K. *Relativistic Effects in Chemistry, Part B*; John Wiley & Sons, Inc.: New York, 1997.
11. Shinke, R. *Photodissociation Dynamics*; Cambridge University Press: Cambridge, 1993.
12. Ashfold, M. N. R.; Baggott, J. E. *Molecular Photodissociation Dynamics*; Royal Society of Chemistry: Piccadilly, 1987.
13. Butler, L. J.; Neumark, D. M. *J. Phys. Chem.* **1996**, *100*, 12801.
14. Simmons, J. P. *J. Phys. Chem.* **1984**, *88*, 1287.
15. Sato, H. *Chem. Rev.* **2001**, *101*, 2687.
16. Jakubetz, W. *Methods in Reaction Dynamics*; Springer: New York, 2001.

17. Ashfold, M. N. R.; Lambert, I. R.; Mordaunt, D. H.; Morley, G. P.; Western, C. M. *J. Phys. Chem.* **1992**, *96*, 2938.
18. Kim, Z. H.; Alexander, A. J.; Kandel, S. A.; Rakitzis, T. P.; Zare, R. N. *Faraday Discuss.* **1999**, *113*, 27.
19. Dixon, R. N. *Acc. Chem. Res.* **1991**, *24*, 16.
20. Hall, G. E.; Houston, P. L. *Annu. Rev. Phys. Chem.* **1989**, *40*, 375.
21. Scherer, N. F.; Knee, J. L.; Smith, D. D.; Zewail, A. H. *J. Phys. Chem.* **1985**, *89*, 5141.
22. Rosker, M. J.; Dantus, M.; Zewail, A. H. *J. Chem Phys.* **1988**, *89*, 6113.
23. Shapiro, M; Bersohn, R. *Annu. Rev. Phys. Chem.* **1982**, *33*, 409.
24. Miller, W. H. *Dynamics of Molecular Collisions, Part B*; Plenum Press: New York, 1976.
25. Butler, L. J. *Annu. Rev. Phys. Chem.* **1998**, *49*, 125.
26. Worth, G. A.; Cederbaum, L. S. *Annu. Rev. Phys. Chem.* **2004**, *55*, 127.
27. Nangia, S.; Truhlar, D. G. *J. Chem. Phys.* **2006**, *124*, 124309.
28. Yarkony, D. *J. Phys. Chem. A.* **2001**, *105*, 6277.
29. Yarkony, D. *Acc. Chem. Res.* **1998**, *31*, 511.
30. Jasper, A. W.; Nangia, S.; Zhu, C.; Truhlar, D. G. *Acc. Chem. Res.* **2006**, *39*, 101.
31. Manthe, U.; Köppel, H. *J. Chem. Phys.* **1990**, *93*, 1658.
32. Greinier, W. *Relativistic Quantum Mechanics*; Springer: New York, 1997.
33. McCarthy, M. I.; Rosmus, P.; Werner, H. J.; Botshwina, P.; Vaida, V. *J. Chem. Phys.* **1987**, *86*, 6693.
34. Ranu, R.; Peyerimhoff, S. D.; Buenker, R. J. *J. Mol. Spectrosc.* **1997**, *68*, 253.

35. Rosmus, P.; Botshwina, P.; Werner, H. J.; Vaida, V.; Engelking, P. C.; McCarthy, M. I. *J. Chem. Phys.* **1987**, *86*, 6677.
36. Nangia, S.; Truhlar, D. G. *J. Chem. Phys.* **2006**, *124*, 124309.
37. Biesner, J.; Schnieder, L.; Ahler, G.; Xie, X.; Welge, K. H.; Ashfold, M. N.R.; Dixon, R. N. *J. Chem. Phys.* **1998**, *88*, 3607.
38. Loomis, R. A.; Reid, J. P.; Leone, S. J. *J. Chem. Phys.* **2000**, *112*, 658.
39. Lambert, I. R.; Morley, G. P.; Mordaunt, D. H.; Ashfold, M. N. R.; Dixon, R. N. *Can. J. Chem.* **1994**, *72*, 977.
40. Smith-Freeman, L. A.; Schroeder, W. P.; Wittig, C. *J Phys. Chem. A.* **2009**, *113*, 2158.

Chapter 2

Experimental Methods

High- n Rydberg hydrogen time-of-flight spectroscopy is the experimental method we employed to study the photodissociation dynamics of AsH_3 and SbH_3 . Section 2.1 outlines the basic methodology of time-of-flight spectroscopy, while subsections discuss hydrogen atom time-of-flight spectroscopy and high- n Rydberg hydrogen time-of-flight spectroscopy. Section 2.2 is a general overview of our experimental apparatus, with detailed descriptions of individual components summarized in the subsections.

2.1 Time-of-flight Spectroscopy

Time-of-flight (TOF) spectroscopy is a sophisticated method designed to measure photofragment translational energy distributions.¹⁻⁵ Wilson and co-workers first demonstrated the advantages of pairing time-of-flight spectroscopy with a molecular beam to study photodissociation dynamics in collision-free conditions.^{6,7} Recent advances in narrow-band, tunable laser sources, vacuum technology and molecular beam techniques have since resulted in highly efficient, versatile TOF experiments.

Typically, a molecule of interest (ABC) is prepared in a cold molecular beam that is intersected by photolysis radiation.



After photodissociation, fragment A “flies” from the interaction region and enters a flight tube where it is detected and the distribution of arrival times is recorded. The TOF tube is routinely positioned mutually orthogonal to the molecular beam and laser radiation.

Conservation of momentum dictates that the recoil velocity of the BC co-fragment can be determined from the recoil velocity of fragment A in the center-of-mass (c.m.) reference frame. The c.m. translational energy is expressed as:

$$E^{c.m.} = E_A^{c.m.} + E_{BC}^{c.m.} = \frac{1}{2} m_A \left(v_A^{c.m.} \right)^2 + \frac{1}{2} m_{BC} \left(v_{BC}^{c.m.} \right)^2 \quad (2)$$

where m is the mass and $E^{c.m.}$ and $v^{c.m.}$ are the translational energy and velocity in the c.m. reference frame, respectively. If the detector is perpendicular to the molecular beam, the velocity of fragment A in the c.m. frame can be determined by:

$$\left(v_A^{c.m.} \right)^2 = \left(v_{c.m.}^L \right)^2 + \left(v_A^L \right)^2 \quad (3)$$

where v^L represents the velocity in the lab frame. This is easily visualized in Figure 2.1 below.

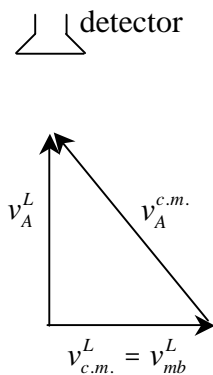


Figure 2.1 The velocity of fragment A in the c.m. frame.

The velocity of the center-of-mass in the lab frame is the velocity of the parent species (ABC) in the molecular beam, $v_{c.m.}^L = v_{mb}^L$. Thus, the measured TOF spectrum can be converted to the c.m. translational energy distribution using the following formulas:

$$E_{c.m.} = \frac{1}{2} m_A \left(\left(\frac{d}{t_A} \right)^2 + v_{mb}^2 \right) \left(1 + \frac{m_A}{m_{BC}} \right) \quad (4)$$

$$P(E_{c.m.}) \propto t^3 f(t(E_{c.m.})) \quad (5)$$

where d is the length of the flight tube, and t is the arrival time of fragment A. Referring to equation (5), the measured TOF distribution, $f(t)$, is converted to the corresponding c.m. translational energy distribution, $P(E_{c.m.})$, by using the time-to-energy Jacobian, which is proportional to t^3 , and the relationship between t and $E_{c.m.}$ given in equation (4).⁸

Energy conservation requires that:

$$E_{avail} = E_{hv} + E_{int}^{ABC} - D_0^{A-BC} = E_{int}^A + E_{int}^{BC} + E_{trans}^{c.m.} \quad (6)$$

where E_{hv} is the energy of the photon, D_0^{A-BC} is the dissociation energy of ABC, E_{int} is the internal energy of a particular species and $E_{trans}^{c.m.}$ is the c.m. translational energy. The use of a molecular beam ensures that the internal energy of the parent molecule is negligible.⁹ If fragment A is atomic with no low-lying states, equation (2) can be written as

$$E_{avail} = E_{hv} - D_0^{A-BC} = E_{int}^{BC} + E_{trans}^{c.m.} = constant \quad (7)$$

Thus, the internal energy distribution of the products (BC) can be determined directly from the c.m. translational energy distribution.⁴

TOF spectroscopy can also be used to measure the angular distribution of products following photodissociation. This is achieved by monitoring the TOF spectrum as a function of detector angle *via* a rotating molecular beam source (or rotating detector).⁴

Traditional TOF techniques often utilize electron impact ionization and quadrupole mass spectrometers to detect photofragments.⁴ The main disadvantage of this detection scheme is the limited resolution due to the uncertainty in the length of the flight path, L. The resolution is predominantly determined by the ratio $\Delta L/L$, where ΔL is the length of the ionizer.^{1,4,10}

2.1.1 Hydrogen Atom TOF Spectroscopy

Hydrogen atom TOF spectroscopy (HTOF) offers improved resolution and signal-to-noise (S/N) compared to traditional TOF spectroscopy.¹¹⁻¹³ The basic set-up of a HTOF

experiment involves the photodissociation of a hydride molecule in a cold molecular beam. Nascent hydrogen atoms are “tagged” in the interaction region via resonance enhanced photoionization involving the $n = 2$ level (Lyman- α). The H^+ ions that enter the flight tube are detected and the TOF spectrum is recorded.

The flight distance between the interaction region and the ion detector is well defined, thus improving resolution compared to conventional TOF spectroscopy using electron impact ionization.¹ The H atoms recoil with the majority of the translational energy due to their small mass as compared to the co-fragments. Also, the velocity of the parent molecules in the molecular beam is small compared to the velocity of the H atoms, minimizing uncertainty in the TOF measurement. However, the H^+ TOF spectrum is assumed to accurately represent the neutral H atom TOF spectrum; yet, stray electric fields and space-charge effects resulting from the high concentration of H^+ ions generated at the interaction region may alter the trajectories of the H^+ ions and introduce error into the TOF measurement.¹¹

2.1.2 High- n Rydberg Hydrogen TOF Spectroscopy

High- n Rydberg hydrogen time-of-flight spectroscopy (HRTOF) was developed by K. Welge and co-workers in the early 1990's.¹⁴ The overall experimental set-up is similar to H atom TOF spectroscopy; the difference lies in the “tagging” process of the hydrogen photofragments.^{1,14} After photolysis, the nascent H atoms are excited to high- n Rydberg levels *via* doubly resonant two-photon excitation. Neutral H atoms that traverse the flight tube are field ionized immediately prior to detection. Space charge effects are

eliminated and the trajectories of the neutral H atoms are impervious to stray electric fields. Vibrational resolution is often achieved in HRTOF experiments, and rotational resolution is attainable.^{1,14}

HRTOF spectroscopy utilizes the unique properties of Rydberg atoms.¹⁵ One crucial key to the success of HRTOF experiments is the long lifetime of the H atoms in high- n Rydberg states. Typically, a weak dc field ($\sim 5 - 30$ V/cm) is applied to a pair of electrodes surrounding the interaction region in order to eliminate ion background signals and make space anisotropic for high- n Rydberg atoms. This enables high- n Rydberg atoms to be prepared with large l values and, consequently, long emission lifetimes that scale as $\sim n^5$.¹⁵

Rydberg atoms are extremely large, with radii scaling as $\sim n^2$. The electron is positioned far from the nuclei, leading to small binding energies. The ionization potential (IP) of high- n Rydberg states decrease rapidly with increasing n ($\text{IP} \sim n^{-2}$), thus weak electric fields are able to effectively remove the electron from high- n Rydberg states. As a result, field ionization is a sensitive method of ionizing high- n Rydberg H atoms in HRTOF spectroscopy.¹⁵

2.2 Experimental Details

High- n Rydberg time-of-flight spectroscopy is used in our experiments to study the ultraviolet photochemistry of AsH₃ and SbH₃. A schematic of the HRTOF apparatus is shown in Figure 2.2. A detailed description of the experimental arrangement has been

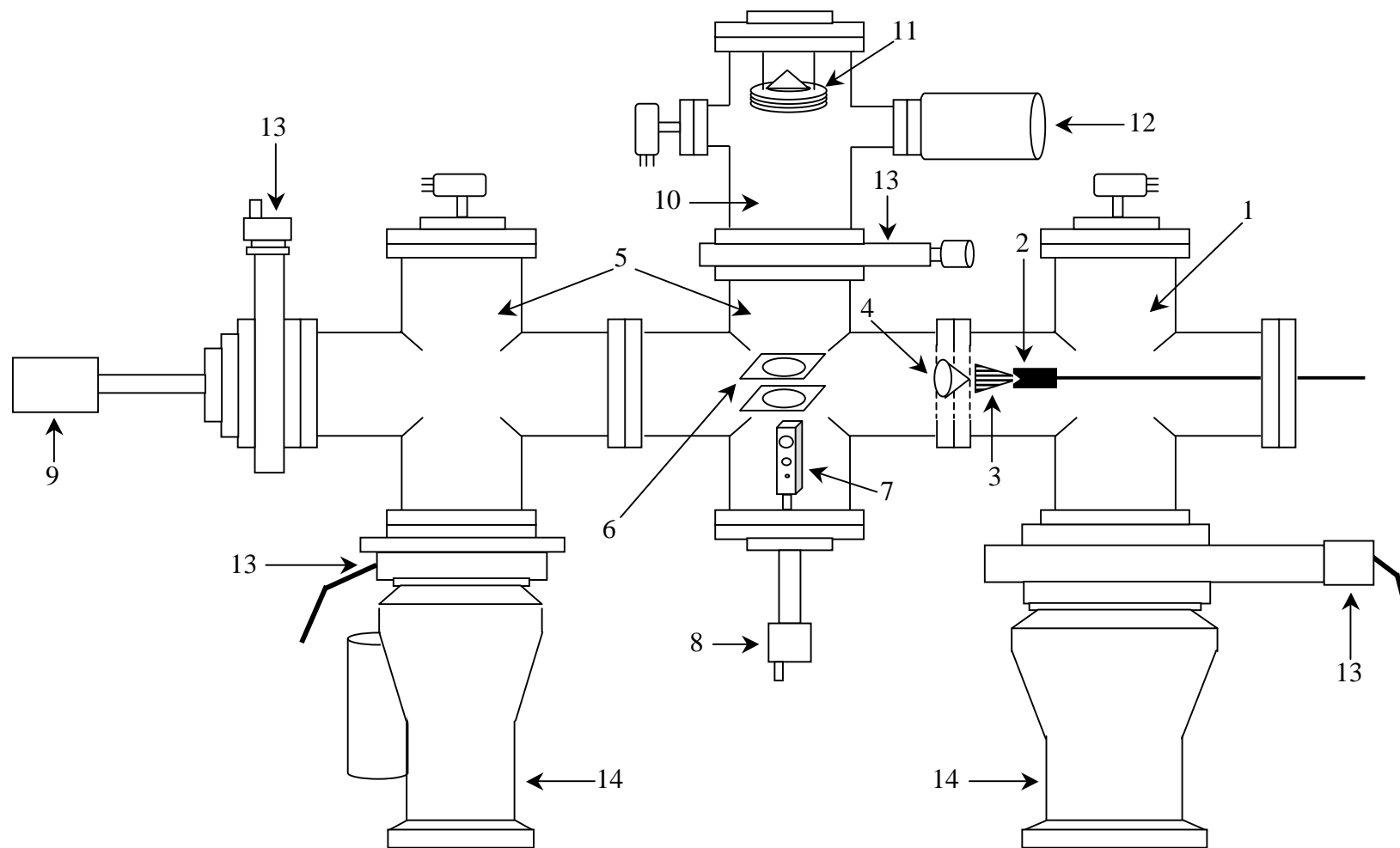


Figure 2.2 Schematic of the HRTOF apparatus. Components include: 1) source chamber, 2) pulsed nozzle, 3) molecular beam, 4) skimmer, 5) main chamber, 6) electrode pair, 7) alignment bar, 8) linear motion feedthrough, 9) RGA, 10) TOF tube, 11) detector assembly, 12) turbomolecular pump, 13) gate valve, 14) diffusion pump.

discussed previously, however pertinent details are presented below.^{8,16} Specifics regarding individual experiments are provided in chapters 3 and 4.

2.2.1 Vacuum System

The vacuum chamber is comprised of three sections, the source chamber, the main chamber and the TOF chamber. The source chamber is connected to a diffusion pump (Varian, VHS-10). During a typical experiment, the pressure varies from 2×10^{-7} Torr (molecular beam turned off) to 2×10^{-4} Torr (molecular beam turned on). A pulsed nozzle (General Valve, 0.8 mm orifice) is housed in the source chamber and operated by a pulse driver (General Valve, Iota One) at a repetition rate of 10 Hz. A 1-mm-diameter skimmer located 1 cm downstream from the nozzle separates the source and main chambers and collimates the molecular beam.

The main chamber is attached to a diffusion pump (Edwards, MK2 series) with a cryo-cooled diffstak (Edwards, 160-series). A background pressure of $\sim 2 \times 10^{-6}$ Torr is maintained in the main chamber during the HRTOF experiments. A pair of electrode plates surrounds the interaction region, located 5 cm downstream from the skimmer. A weak dc field (~ 20 V/cm) is applied to the electrodes.

A quadrupole mass spectrometer (Stanford Research Systems, RGA 300) is attached to the main chamber and positioned in-line with the molecular beam. This allows us to monitor the composition of the molecular beam.

The flight path is mutually perpendicular to the molecular beam and lasers. We have three TOF tubes, varying in length from 13.9 cm to 110.6 cm. The resolution in a

HRTOF experiment is dependent upon the length of the drift distance. Shorter distances are better suited for low S/N experiments; however, resolution is sacrificed. The HRTOF experiments discussed herein all had respectable S/N ratios, thus a 43.5 cm flight tube was utilized. The exact length of the TOF tube was determined by the photodissociation of HCl, since the bond dissociation energy and spin-orbit splitting values are well established.¹⁵ The high- n Rydberg atoms that “fly” from the interaction region and drift along the TOF axis, reach the microchannel plate detectors (MCPs) located at the top of the TOF tube.

2.2.2 Detector Assembly

The detector assembly, shown in Figure 2.3, consists of two back-to-back MCPs (Photonis, 5 cm diameter) in a chevron configuration paired with a conical anode. Two fine meshes preceding the MCPs are responsible for field ionization. The resulting H⁺ ions are subsequently detected by the MCPs with near unit efficiency.^{8,17} The output signal is amplified using a fast pulse amplifier (Avtech, AV-141C1).

2.2.3 Laser Systems

The outputs of three pulsed laser systems are utilized; a schematic is shown in Figure 2.4. The photolysis and probe radiations intersect the molecular beam at the interaction region and counter-propagate through the main chamber with a crossing angle $\sim 7^\circ$.

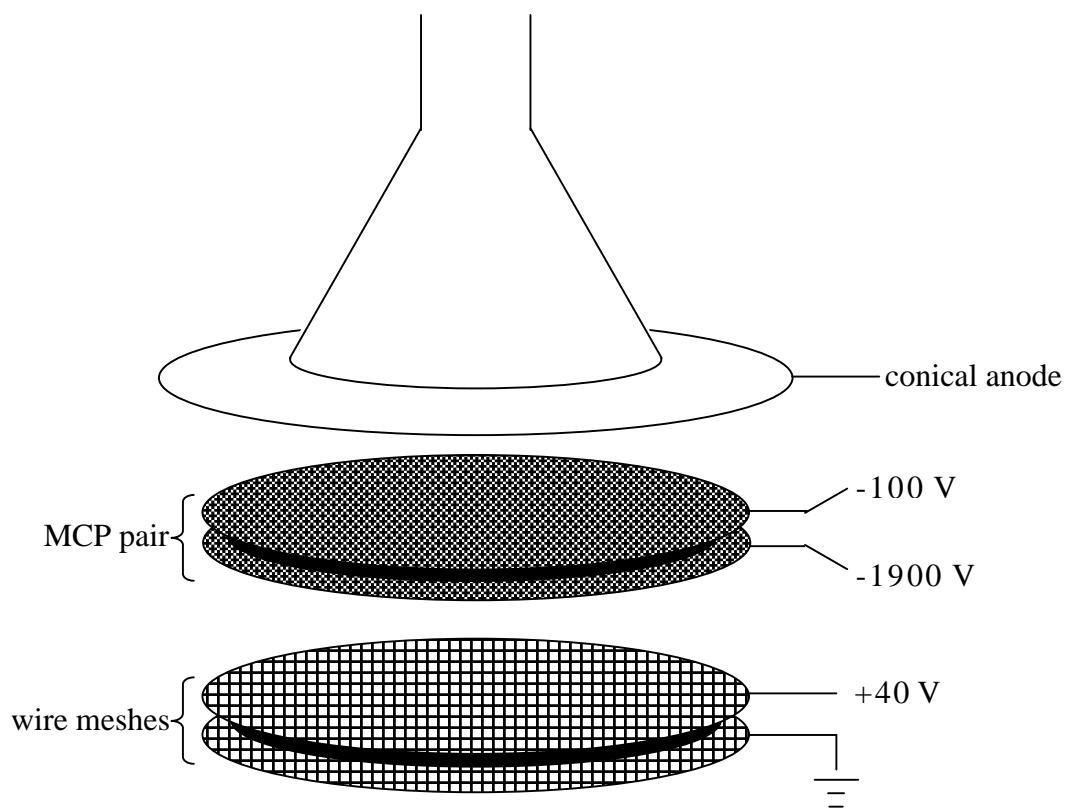


Figure 2.3 Schematic of the detector assembly

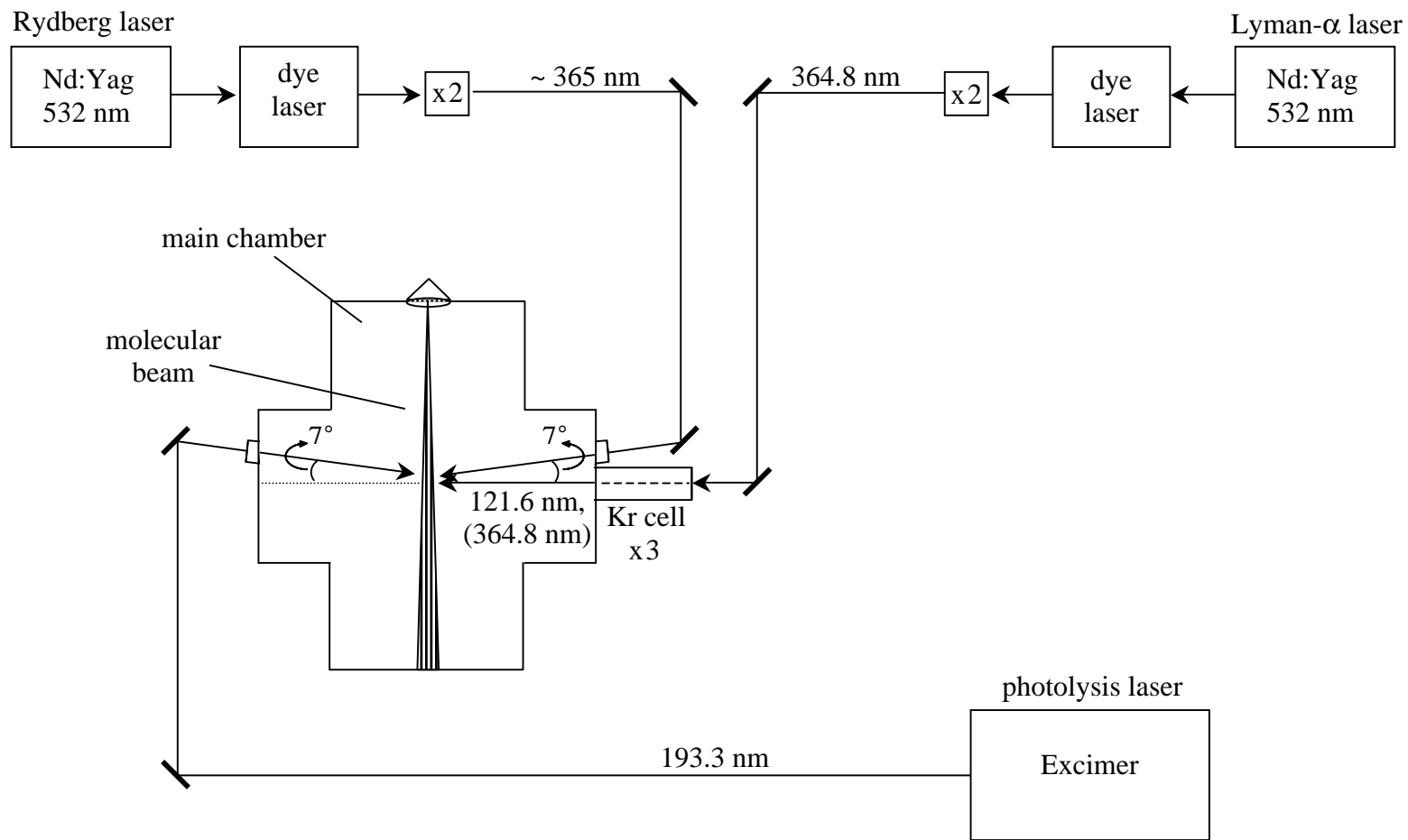


Figure 2.4 Schematic of the main chamber and laser radiation pathways. This represents an aerial view.

An ArF excimer laser (Lambda Physik Compex 201) provides the photolysis radiation at 193.3 nm. The photolysis radiation is focused using a 100 cm focal length lens.

Following photodissociation, the nascent H atoms are probed using sequential excitation to high- n Rydberg levels: 121.6 nm radiation excites the $2p \leftarrow 1s$ transition of the H atoms (Lyman- α) and ~ 365 nm radiation promotes the excited H atoms to a Rydberg state with $n \sim 50$. Two Nd-YAG pump lasers (Continuum Powerlite 8010 and 9010) and two dye lasers are used for this "tagging" of the H atoms. The output of one dye laser (Continuum ND6000, LDS 750 dye) is frequency doubled in a KDP-C crystal, producing 364.8 nm radiation. The resulting near-UV radiation is then focused by a quartz lens ($f = 75$ mm) into a 10-cm tripling cell, where Lyman- α radiation is generated by non-resonant frequency tripling in Kr. The VUV radiation is focused by a MgF_2 lens ($f.l. = 64$ mm) into the interaction region. The output of the second dye laser (Continuum ND6000, LDS 750 dye) is frequency doubled in a KDP-C crystal, yielding the Rydberg (~ 365 nm) radiation required to promote the H atom ($n = 2$) to a high Rydberg state. The Rydberg radiation is focused using a 100 cm lens.

A complete TOF spectrum is recorded with each laser shot. Averaging a large number of laser shots, *e.g.* 60,000 – 100,000 laser shots, improves the S/N in our photodissociation experiments.

2.2.4 Laser and Molecular Beam Alignment

The spatial and temporal overlap of the photolysis and probe radiations with the molecular beam is crucial and challenging. We begin the alignment process by first utilizing the alignment bar that is mounted to a linear motion feedthrough located directly below the interaction region in the main chamber. The alignment bar is shown in Figure 2.5.

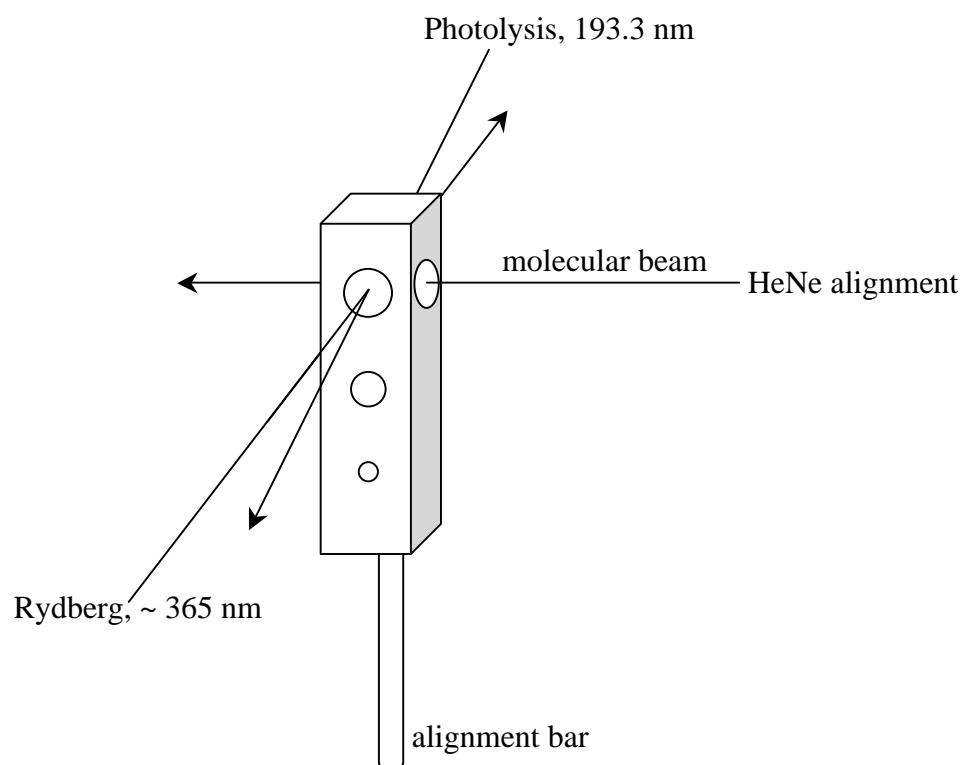


Figure 2.5 Schematic of the alignment bar.

There are three pinholes of varying sizes in the alignment bar. There is also a pinhole that is perpendicular to the molecular beam. A HeNe laser is aligned through the source chamber, the skimmer and the largest pinhole in the alignment bar (perpendicular to the molecular beam) in order to determine the relative position of the molecular beam (refer to Figure 2.5). Next, the photolysis (193.3 nm) and Rydberg (~ 365 nm) radiations are sent through the largest pinhole in the alignment bar, whereby the intensity of the radiations are optimized to ensure good spatial overlap with the molecular beam. The spatial overlap of the photolysis and Rydberg radiation can be further verified by raising the smaller diameter pinholes in the alignment bar to the height of the molecular beam.

The spatial alignment of the 121.6 nm radiation is cumbersome and cannot be optimized using the alignment bar. The alignment of the fundamental 364.8 nm radiation does not guarantee Lyman- α alignment, since the two beams diverge when passing through an optic off-center. Thus, we begin by first expanding a molecular beam of NO (Matheson Tri-Gas, 99.5% purity) through the pulsed nozzle. We apply a positive potential (+ 80 V) to the bottom electrode plate beneath the interaction region, which accelerates the positive ions generated from the VUV photoionization of NO. An adequate alignment of the 121.6 nm radiation can be found by optimizing the ion signal detected by the MCPs.

A digital delay/pulse generator (Stanford Research Systems, DG-535) was used to coordinate the temporal overlap of the three laser systems. The time delay between the photolysis and probe lasers was ~ 20 ns for our experiments. The laser profiles were also monitored by three high-speed photodiodes (Thorlabs, DET25K).

2.3 Chapter 2 References

1. Ashfold, M. N. R.; Lambert, I. R.; Mordaunt, D. H.; Morley, G. P.; Western, C. M. *J. Phys. Chem.* **1992**, *96*, 2938.
2. Wilson, K. R. *Excited State Chemistry*; Pitts, J. N., Eds.; Gordon and Breach: New York, 1970.
3. Ashfold, M. N. R.; Mordaunt, D. H.; Wilson, S. H. S. *Adv. Photochem.* **1996**, *21*, 217.
4. Wodtke, A. M.; Lee, Y. T. *Molecular Photodissociation Dynamics*; Ashfold, M. N. R.; Baggott, J. E., Eds.; The Royal Society of Chemistry Burlington House: London 1987, pp. 31-59.
5. Sato, H. *Chem. Rev.* **2001**, *101*, 2687.
6. Riley, S. J; Wilson, K. R. *Faraday Discuss. Chem. Soc.* **1972**, *53*, 132.
7. Busch, G. E.; Wilson, K. R. *J. Chem. Phys.* **1972**, *56*, 3626.
8. Zhang, J.; Dulligan, M.; Wittig, C. *J. Phys. Chem.* **1995**, *99*, 7446.
9. Scoles, G. *Atomic and Molecular Beam Methods*; Oxford University Press: New York, 1988, Vol. 1.
10. Lee, Y.T.; McDonald, J. D.; Lebreton, P. R.; Herschbach, D. R. *Rev. Sci. Instrum.* **1969**, *40*, 1402.
11. Xie, X.; Schnieder, L.; Wallmeier, H.; Boettner, R.; Welge, K. H.; Ashfold, M. N. R. *J. Chem. Phys.* **1990**, *92*, 1608.
12. Biesner, J.; Schnieder, L.; Schmeer, J.; Ahlers, G.; Xie, X.; Welge, K. H.; Ashfold, M. N. R.; Dixon, R. N. *J. Chem. Phys.* **1988**, *88*, 3607.
13. Biesner, J.; Schnieder, L.; Ahlers, G.; Xie, X.; Welge, K. H.; Ashfold, M. N. R.; Dixon, R. N. *J. Chem. Phys.* **1989**, *91*, 2901.
14. Schnieder, L.; Meier, W.; Welge, K. H.; Ashfold, M. N. R.; Western C. M. *J. Chem. Phys.* **1990**, *92*, 7027.
15. Gallagher, T. F. *Rydberg Atoms*; Cambridge University Press: Cambridge, 1994.
16. Zhang, J.; Dulligan, M.; Wittig, C. *J. Phys. Chem.* **1997**, *107*, 1403.

17. Wiza, J. L. *Nuclear Instruments and Methods*, **1979**, 162, 587.

Chapter 3

The Ultraviolet Photochemistry of AsH₃

High- n Rydberg time-of-flight spectroscopy has been used to study the 193.3 nm photolysis of AsH₃. The center-of-mass translational energy distribution for the 1-photon process: $\text{AsH}_3 + h\nu \rightarrow \text{AsH}_2 + \text{H}$, $P(E_{\text{c.m.}})$, indicates that AsH₂ internal excitation accounts for $\sim 64\%$ of the available energy [*i.e.*, $h\nu - D_0(\text{H}_2\text{As-H})$]. Secondary AsH₂ photodissociation also takes place. Analyses of superimposed structure atop the broad $P(E_{\text{c.m.}})$ distribution suggest that AsH₂ is formed with significant a -axis rotation as well as bending excitation. Comparison of the results obtained with AsH₃ versus those of the lighter group-V hydrides (NH₃, PH₃) lends support to the proposed mechanisms.

3.1 Introduction

The ultraviolet photolysis of gaseous AsH_3 is germane to the fabrication of semiconductor and electro-optical devices.¹⁻⁴ For example, it has been demonstrated that the 193.3 nm irradiation of AsH_3 can be used to stimulate and manipulate the growth of III-V semiconductor compounds such as GaAs, InGaAs, InGaAsP, etc. during metal-organic chemical vapor deposition (MOCVD).^{2,3} AsH_3 is of fundamental scientific interest as well. For example, a sensible goal is a quantitative understanding of how molecular properties and photochemical and photophysical mechanisms vary when the lightest group-V hydride, NH_3 , is replaced by progressively heavier counterparts (PH_3 , AsH_3 , SbH_3 , BiH_3) *i.e.*, that span the non-relativistic and relativistic regimes. High quality experimental data for the full complement of group-V hydrides would comprise a benchmark against which theoretical models could be tested.

Although there has been a great deal of theoretical and experimental research on NH_3 , much less has been done with the heavier group-V hydrides. Experimentalists must contend with toxicity and sample preparation / handling issues, and theoreticians must contend with large numbers of electrons and relativistic effects.

Extensive research on the photochemistry and photophysics of NH_3 has yielded high quality potential energy surfaces (PES's) and a consensus regarding the properties of the lowest excited surfaces and the dynamical processes that transpire on them.⁵⁻¹² This system is a textbook example of predissociation and nonadiabatic dynamics. The ground state electron configuration is $(1a_1)^2(2a_1)^2(1e)^4(3a_1)^2$ (C_{3v} notation). The promotion of an electron from the lone pair orbital $3a_1$ ($1a_2''$ in the D_{3h} limit) to the $3s a_1'$ Rydberg

orbital accounts for the $\tilde{A}^1A_2'' \leftarrow \tilde{X}^1A_1$ transition, with its pyramidal-to-planar geometry change. Consequently, the $\tilde{A} \leftarrow \tilde{X}$ absorption spectrum displays a prominent progression in the ν_2 umbrella mode.

Vibrational levels of the \tilde{A}^1A_2'' state are predissociated to the extent that there is no discernible rotational structure.¹¹ There is a small barrier to dissociation on this surface that arises from the Rydberg-to-valence transformation that accompanies lengthening of the N-H bond.^{5,7,13} The height of this barrier increases with out-of-plane bend angle (minimizing at planar geometries). For the \tilde{A}^1A_2'' vibrational levels $\nu_2' = 1$ and 2, dissociation proceeds *via* tunneling through the barrier. An \tilde{A}/\tilde{X} conical intersection also plays a significant role.⁵⁻⁸

Referring to Fig. 3.1, in C_{2v} symmetry $NH_3(\tilde{A})$ correlates diabatically with $NH_2(\tilde{X}^2B_1)$, while $NH_3(\tilde{X})$ correlates diabatically with $NH_2(\tilde{A}^2A_1)$. For nonplanar geometries ($\theta \neq 90^\circ$ in Fig. 1), the $NH_3 \tilde{X}$ and \tilde{A} states are each of the same symmetry and there is avoided crossing. Consequently, $NH_3(\tilde{A})$ correlates adiabatically with $NH_2(\tilde{A})$, while $NH_3(\tilde{X})$ correlates adiabatically with $NH_2(\tilde{X})$. Figure 3.1 illustrates these aspects of the surfaces.¹⁴

The barrier and conical intersection influence the dissociation dynamics of $NH_3(\tilde{A})$. Biesner *et al.* studied this for $0 \leq \nu_2' \leq 6$ using H atom photofragment translational energy spectroscopy.¹⁵ They found that NH_2 is born with significant internal excitation, mainly in the form of *a*-axis rotation. They concluded that NH_3 out-of-plane

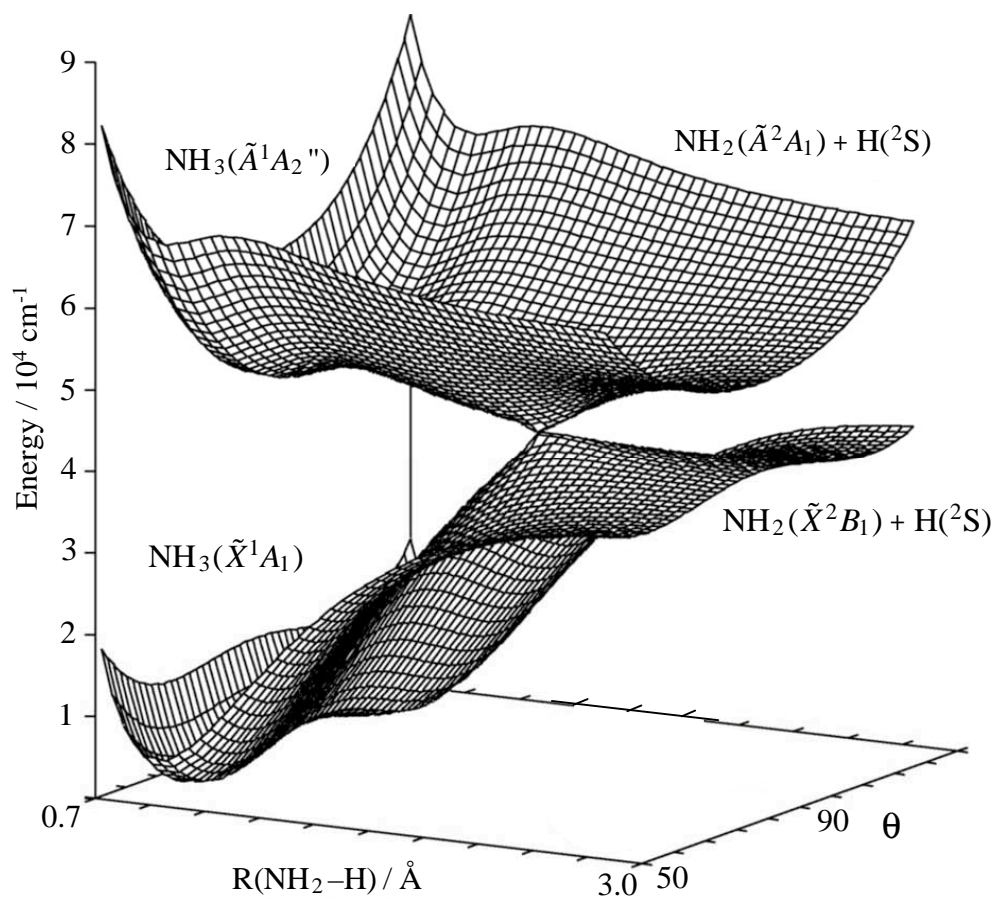


Figure 3.1 The ground and excited state potential energy surfaces of NH₃ (adapted from reference 14). Vertical excitation from the NH₃ \tilde{X}^1A_1 ground vibrational level to \tilde{A}^1A_2'' can lead to dissociation to NH₂(\tilde{A}^2A_1) *via* adiabatic paths, or to NH₂(\tilde{X}^2B_1) *via* nonadiabatic paths that pass near the conical intersection. θ is the angle between an NH bond and the normal to the trigonal plane. $\theta = 90^\circ$ corresponds to planar geometry.

bending is encouraged by the shape of the potential in the vicinity of the conical intersection, resulting in considerable $\text{NH}_2(\tilde{X})$ a -axis rotation. In contrast, near-planar dissociation leads to NH_2 with modest a -axis rotation. It is intuitive that umbrella mode vibrational excitation correlates with a -axis rotation. It should be noted that competition between adiabatic and nonadiabatic pathways is energy dependent, with $\text{NH}_2(\tilde{A})$ accounting for 10-30% of the NH_2 product when NH_3 is excited to $v_2' = 6$ of its \tilde{A} state.¹⁵ These experimental findings are in accord with theoretical calculations and results from other experiments.^{5,10,12,15}

The dissociation dynamics of PH_3 are similar to those of NH_3 , albeit with several important differences. The $\tilde{A} \leftarrow \tilde{X}$ transition involves the promotion of the lone pair orbital $5a_1$ to the $4s a_1$ Rydberg orbital, and calculations indicate a small barrier on the $\text{PH}_3(\tilde{A})$ surface.¹⁶ The height of this barrier is comparable to the zero point energy of the stretching vibration. The $\tilde{A} \leftarrow \tilde{X}$ absorption spectrum is a broad continuum, consistent with rapid \tilde{A} dissociation.¹⁷ Whereas the $\text{NH}_3(\tilde{A})$ equilibrium geometry is planar, the $\text{PH}_3(\tilde{A})$ equilibrium geometry has been calculated to be nonplanar ($\theta_{\text{H-P-H}} \sim 114^\circ$).¹⁶ The ground state of PH_3^+ is also nonplanar,¹⁸ so it is intuitive that $\text{PH}_3(\tilde{A})$ is nonplanar. The $\tilde{A} \leftarrow \tilde{X}$ transition increases the equilibrium bond angle from 93.5° to 114° ,¹⁶ which ensures significant v_2 vibrational excitation. Table 3.1 gives values of relevant equilibrium angles for NH_3 , PH_3 , and AsH_3 .

Table 3.1 Equilibrium H-M-H angles for N, P and As, and related electronic states.*

$\text{NH}_3(\tilde{X}^1A_1)$	107°	
$\text{NH}_3(\tilde{A}^1A_2'')$	120°	$\text{NH}_3(\tilde{A}) \rightarrow \text{NH}_2(\tilde{X})$
$\text{NH}_2(\tilde{X}^2B_1)$	103.4°	$\theta_{\text{H-N-H}}^{\text{equil}} : 120^\circ \rightarrow 103.4^\circ$
$\text{NH}_2(\tilde{A}^2A_1)$	144°	
$\text{PH}_3(\tilde{X}^1A_1)$	93.5°	
$\text{PH}_3(\tilde{A}^1A_1)$	114°	$\text{PH}_3(\tilde{A}) \rightarrow \text{PH}_2(\tilde{X})$
$\text{PH}_2(\tilde{X}^2B_1)$	91.4°	$\theta_{\text{H-P-H}}^{\text{equil}} : 114^\circ \rightarrow 91.4^\circ$
$\text{PH}_2(\tilde{A}^2A_1)$	123.1°	
$\text{AsH}_3(\tilde{X}^1A_1)$	92.1°	
$\text{AsH}_3(\tilde{A}^1E)$	112°	$\text{AsH}_3(\tilde{A}) \rightarrow \text{AsH}_2(\tilde{X})$
$\text{AsH}_2(\tilde{X}^2B_1)$	90.4°	$\theta_{\text{H-As-H}}^{\text{equil}} : 112^\circ \rightarrow 90.4^\circ$
$\text{AsH}_2(\tilde{A}^2A_1)$	123°	

*See text for details and references

It has been suggested that the $\text{PH}_3 \tilde{A}/\tilde{X}$ conical intersection affects the dissociation dynamics in a manner that is analogous to the case of NH_3 . Several experimental studies have shown that PH_2 is born with substantial internal excitation,¹⁹⁻²¹ though the exact nature of this excitation is more difficult to discern than for NH_2 . Lambert *et al.*¹⁹ investigated the UV photolysis of PH_3 by using high- n Rydberg time-of-flight (HRTOF) spectroscopy. They found that $\text{PH}_2(\tilde{X})$ rovibrational excitation accounts, on average, for $\sim 62\%$ of the available energy. Structured translational energy distributions indicated significant $\text{PH}_2(\tilde{X})$ a -axis rotation, as well as bending excitation. It was postulated that $\text{PH}_2(\tilde{X})$ vibrational excitation is due to the change in bond angle: from 114° in $\text{PH}_3(\tilde{A})$ to 91.4° in $\text{PH}_2(\tilde{X})$. The data also showed evidence of $\text{PH}_2(\tilde{X})$ photodissociation.

The scarcity of experimental and theoretical data on AsH_3 is striking compared to what is available for the lighter group-V hydrides. For example, no information concerning dissociation pathways on \tilde{A} and \tilde{X} surfaces is available. However, taking cues from PH_3 and NH_3 , it is *assumed* that there is a small barrier to dissociation on \tilde{A} and an \tilde{A}/\tilde{X} conical intersection. The $\tilde{A} \leftarrow \tilde{X}$ absorption is continuous, with weak superimposed structure, as with PH_3 . Analyses of AsH_3 and PH_3 absorption spectra reveal that $v_2' \sim v_2''/2$ in these cases, whereas $v_2' \sim v_2''$ for NH_3 .¹⁷ Humphries *et al.* have proposed that the \tilde{A} states of AsH_3 and PH_3 are pyramidal, with $\tilde{A} \leftarrow \tilde{X}$ transitions terminating on levels that lie above the inversion barrier.¹⁷ Also, the AsH_3 photoelectron spectrum suggests a pyramidal geometry.^{22,23} The equilibrium bond angle for $\text{AsH}_3(\tilde{A})$ is

assumed to be 112° on the basis of the AsH_3^+ bond angle²⁴ and the geometry of $\text{PH}_3(\tilde{A})$. The equilibrium bond angle for the $\text{AsH}_3 \tilde{X}$ state is 92.1° .²⁵ It is noteworthy that a calculation of the lowest excited singlet indicates that it has E symmetry, which would make this case quite different than the lowest excited singlets of NH_3 and PH_3 . This will be discussed later.

Velocity aligned Doppler spectroscopy has been used by Koplitz *et al.* to examine the 193.3 nm (hereafter referred to simply as 193 nm) photodissociation of AsH_3 .²⁶ Their results indicate that AsH_2 fragments are formed with average internal energies $\sim 2/3$ the available energy. However, the low resolution of the method precluded a determination of the internal energy distribution. An $\text{AsH}_2 \tilde{A} \rightarrow \tilde{X}$ emission spectrum has been recorded by Ni *et al.* following 193 nm photolysis of AsH_3 .²⁹ Both v_2' and v_2'' progressions were evident, as well as spectral features that were assigned to As. Photolysis of AsH_2 was suggested as a possible mechanism for the As emission.

In the study reported here, the 193 nm photodissociation of AsH_3 has been examined using HRTOF spectroscopy. Figure 3.2 shows a number of possible products.^{22,24,28-33} Note that the photon energy is substantially larger than the AsH_3 bond dissociation energy. The results indicate that AsH_2 is produced with significant internal excitation. $\text{AsH}_2(\tilde{A})$ is also produced, but it is a minor channel. The center-of-mass (c.m.) translational energy distribution, $P(E_{\text{c.m.}})$, consists of partially resolved structure superimposed on a broad background. Unambiguous assignment is not feasible because the structured features are broad and of modest signal-to-noise ratio (S/N) and there is a significant amount of secondary photolysis.

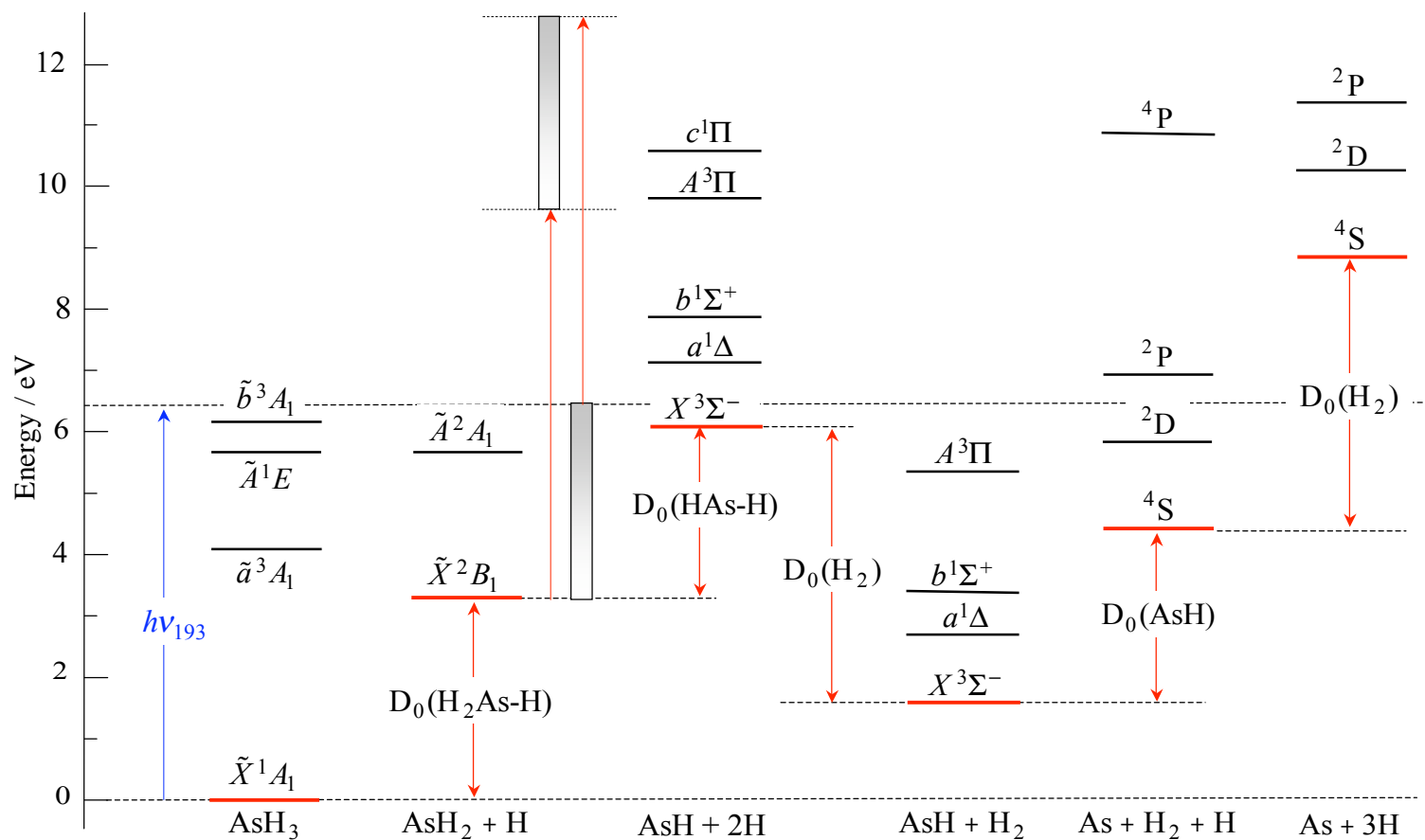


Figure 3.2 Energies relevant to 193 nm photolysis of AsH₃ are indicated, including product species that can undergo secondary photodissociation. The two red arrows and shaded rectangles to the right of the AsH₂ + H column indicate the range of energies associated with internally excited AsH₂.^{22,24,28-33}

In consideration of the photodissociation dynamics of NH_3 and PH_3 , it is suggested that the main features arise from $\text{AsH}_2(\tilde{X})$ with substantial a -axis rotation, as well as bending excitation. Secondary photolysis of $\text{AsH}_2(\tilde{X})$ yields AsH . In light of the similarities between the present results and those obtained with PH_3 , it is interesting that the $\text{AsH}_3 \tilde{A}$ state has been calculated to be 1E ,²⁴ whereas the $\text{PH}_3 \tilde{A}$ state is 1A_1 . The AsH_3 system lies intermediate between non-relativistic and relativistic regimes. An important goal is that this system achieves the same degree of accord between theory and experiment enjoyed by lighter counterparts.

3.2 Experimental Methods and Results

The HRTOF arrangement shown in Fig. 3.3 has been discussed previously,³⁴ so only details that are relevant to the present study are given here. A pulsed valve (General Valve, 0.8 mm orifice) expanded mixtures of AsH_3 (Matheson Tri-Gas, 99.999%) dilute in a carrier gas (10% in H_2 , 5% in H_2 , and 5% in Ar). The molecular beam was collimated 1 cm downstream from the nozzle by a 1 mm diameter skimmer. At the interaction region, 5 cm downstream from the skimmer, the molecular beam was intersected by the outputs of 3 pulsed laser systems.

Photolysis radiation was from an ArF excimer laser (Lambda Physik Compex 201). HRTOF spectroscopy probed nascent H atoms by using sequential excitation to high- n Rydberg levels: 121.6 nm radiation excited H atoms (Lyman- α) and ~ 365 nm radiation promoted the excited H atoms to a Rydberg state with $n \sim 50$. Metastable H-

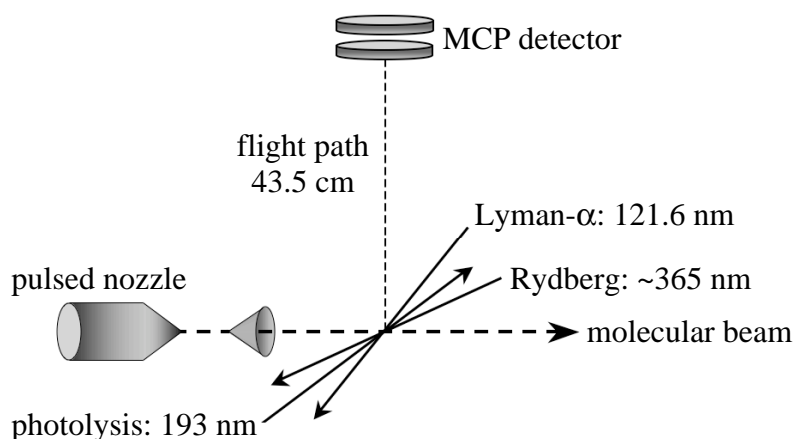


Figure 3.3 Schematic of the experimental arrangement.

atoms to a Rydberg state with $n \sim 50$. Metastable H atoms that traversed the 43.5 cm flight tube (perpendicular to the interaction region, see Fig. 3.3) were field ionized and detected with near unit efficiency by two back-to-back microchannel plates (MCP's) in a chevron configuration. A weak dc field applied to a pair of electrodes surrounding the interaction region eliminated ion background signals and made space anisotropic for high- n Rydberg atoms. This enabled high- n Rydberg atoms to be prepared with large orbital angular momentum values and consequently long spontaneous emission lifetimes after they left the interaction region.

An HRTOF spectrum for the photolysis of jet-cooled AsH_3 is presented in Fig. 3.4. Vertical dashed lines indicate the earliest arrival time that can be attributed to primary photolysis using $D_0(\text{H}_2\text{As-H}) = 74.9 \pm 0.2 \text{ kcal/mol}$.²² The signal that precedes

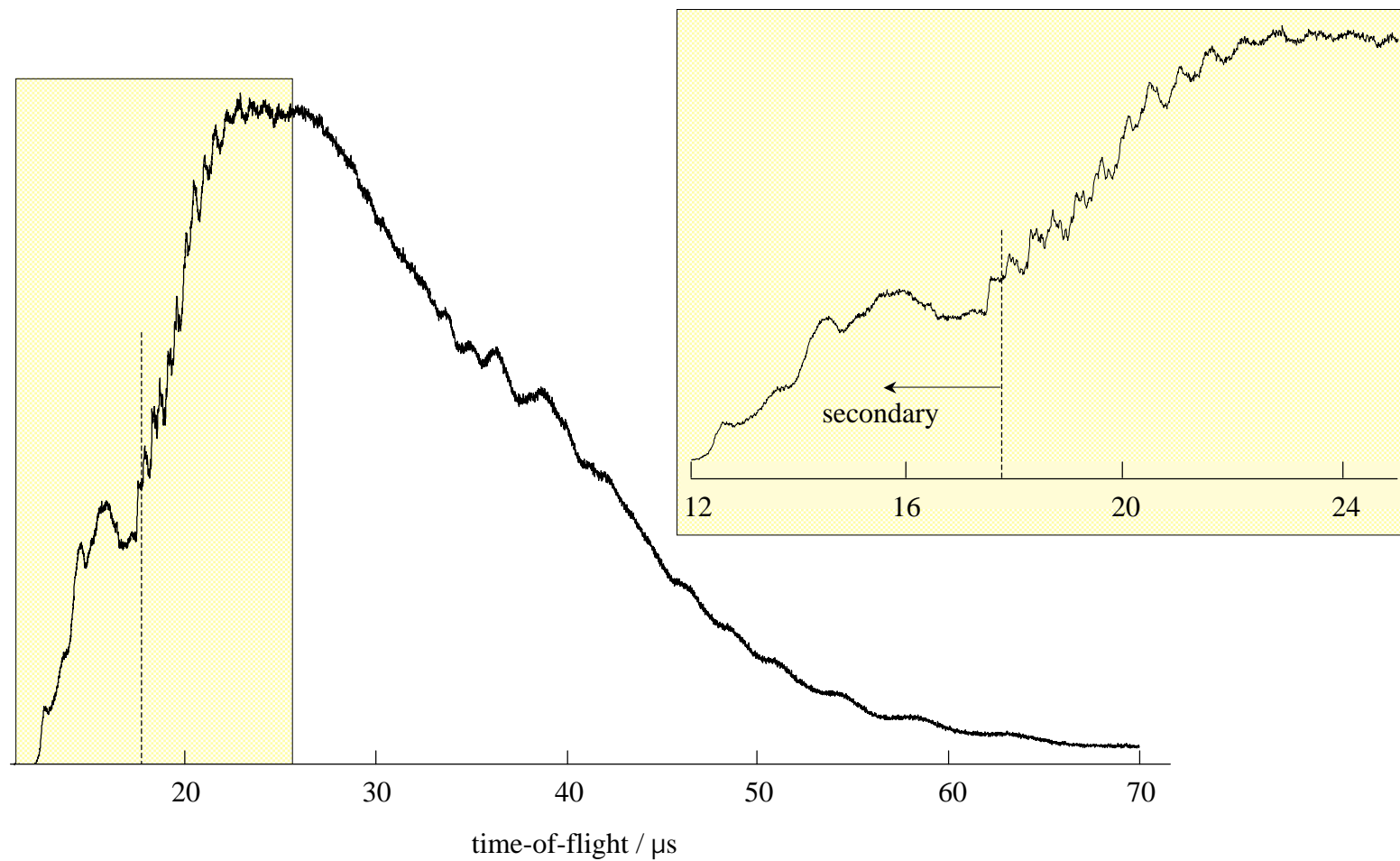


Figure 3.4 HRTOF spectrum obtained using 10% AsH₃ and 193 nm photolysis: Results from 121,000 laser firings were summed to obtain the trace. The 193 nm energy ranged between 2.2 and 2.5 mJ. The vertical dashed lines indicate the earliest possible arrival time compatible with 1-photon AsH₃ photodissociation.

the dashed line is evidence of secondary photolysis. Many such spectra were recorded, and no qualitative differences were observed. The one shown in Fig. 4 is one of the better ones insofar as S/N is concerned.

Figure 3.5 shows HRTOF spectra for the photolysis of AsH₃ (10% in H₂). These traces were obtained using 193 nm energies of 0.5 and 4.2 mJ. The 193 nm radiation is focused using a 100 cm focal length lens, resulting in fluences of ~ 5 and ~ 40 J / cm², respectively. Reducing the photolysis fluence lessens the production of fast H atoms that derive from secondary photolysis. However, the broad unstructured one-photon signal was not simplified; it was just of lower intensity. Analogous spectra collected using supersonic expansions of 5% AsH₃ in H₂ and 5% AsH₃ in Ar showed no discernible variations from the spectrum in Fig. 3.4, so they are not presented.

The spectrum in Fig. 3.4 was converted to the c.m. translational energy distribution shown in Fig. 3.6(a) by using the formulas:

$$E_{c.m.} = \frac{1}{2} m_H \left((d/t)^2 + v_{mb}^2 \right) \left(1 + m_H / m_{AsH_2} \right) \quad (1)$$

$$P(E_{c.m.}) \propto t^3 f(t(E_{c.m.})) \quad (2)$$

where v_{mb} is the molecular beam velocity, d is the length of the flight tube, and t is the H-atom arrival time. Referring to (2), the measured TOF distribution, $f(t)$, is converted to the corresponding c.m. translational energy distribution, $P(E_{c.m.})$, by using the time-to-energy Jacobian, which is proportional to t^3 , and the relationship between t and $E_{c.m.}$ given in (1). Note: $P(E_{c.m.})$ applies only to those channels that yield H atoms.

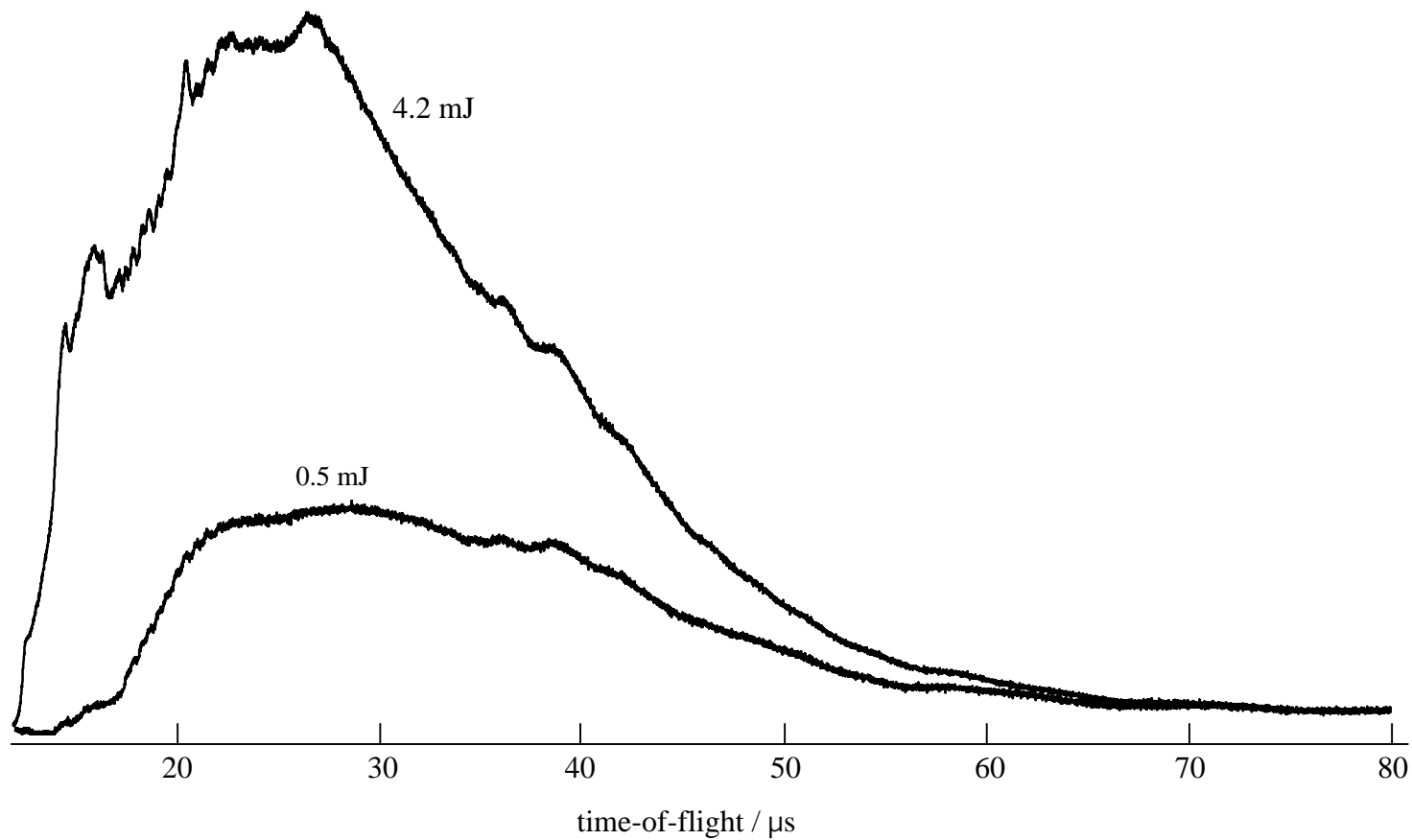


Figure 3.5 HRTOF spectra for photolysis energies of 0.5 and 4.2 mJ; 135,000 and 116,000 laser firings, respectively.

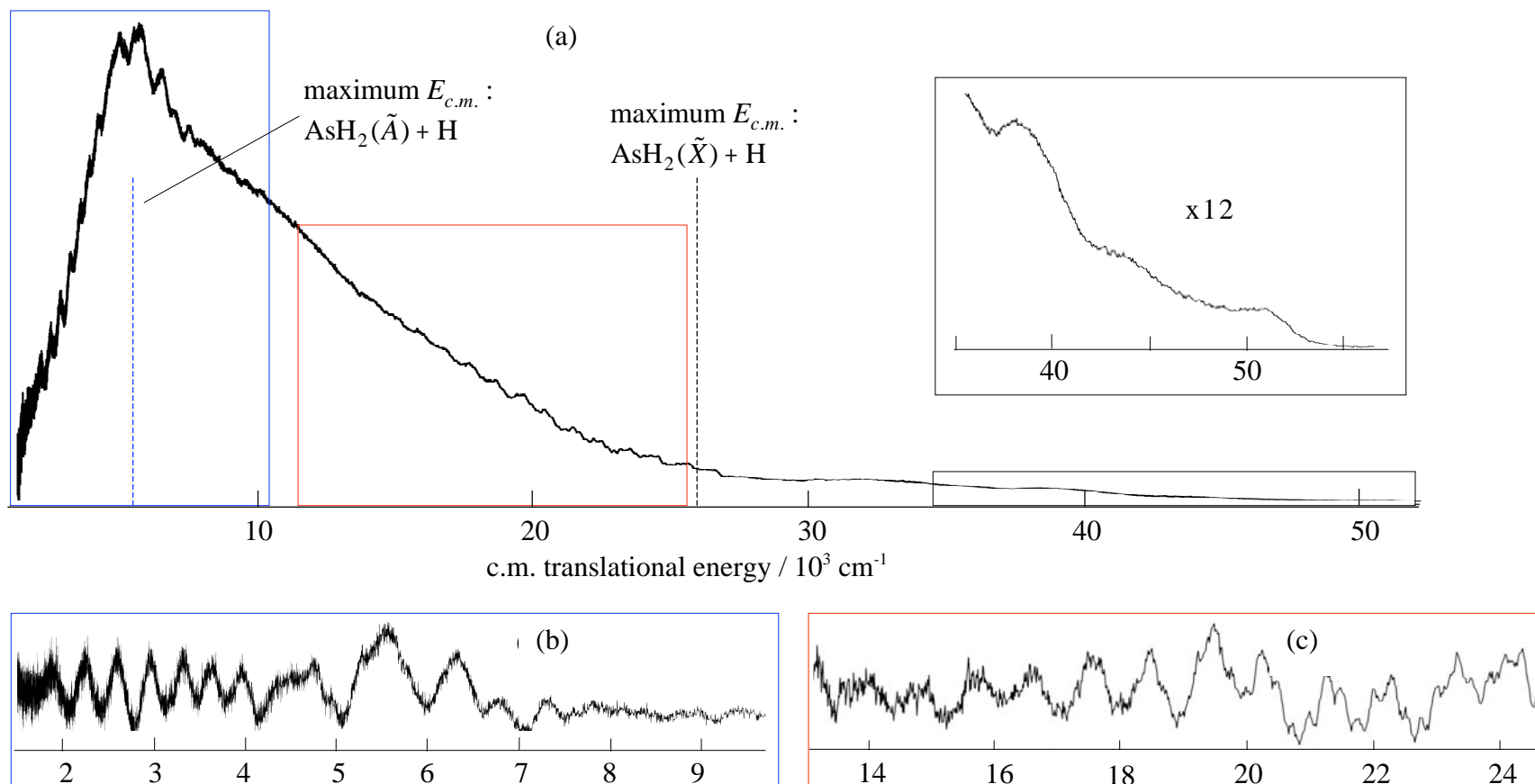


Figure 3.6 (a) The HRTOF spectrum in Fig. 4 has been converted to $P(E_{c.m.})$; inset: expanded view of the high-energy region. The black dashed line to the right of the red box indicates the maximum $E_{c.m.}$ available to a 1-photon process. The blue dashed line in the blue box indicates the maximum $E_{c.m.}$ available to the $\text{AsH}_2(\tilde{A})$ channel via a 1-photon process. (b) This pertains to the blue box in (a). To highlight peaks, the underlying continuous distribution has been suppressed. (c) This pertains to the red box in (a). To highlight peaks, the underlying continuous distribution has been suppressed.

The black dashed line to the right of the red box in Fig. 3.6(a) indicates the maximum $E_{c.m.}$ allowed by energy conservation when the H atoms result from primary photolysis. Translational energies in excess of this value derive from secondary photolysis. The inset in Fig. 3.6(a) shows a fairly abrupt termination of $P(E_{c.m.})$ at $51\,800 \pm 500\text{ cm}^{-1}$, corresponding to dissociation of AsH_2 with internal energies near $D_0(\text{H-AsH}) = 66.5 \pm 0.02\text{ kcal/mol}$,²² and negligible AsH internal excitation. The value $51\,800 \pm 500\text{ cm}^{-1}$ was obtained by deconvoluting the data to account for instrument resolution.

Background subtraction was used to elucidate peaks in the ranges 1000-10 000 cm^{-1} [Fig. 3.6(b)] and 14 000-24 000 cm^{-1} [Fig. 3.6(c)]. The average spacing between peaks in the high-energy region is $\sim 1000\text{ cm}^{-1}$, in rough accord with the AsH_2 bend frequency.²⁸ In the low-energy region, the spacing is $\sim 360\text{ cm}^{-1}$ for the range 1500-5000 cm^{-1} . We interpret this as due to a -axis rotation in $\text{AsH}_2(\tilde{X})$, as discussed in the next section.

3.3 Discussion

The unambiguous identification of the participating pathways and mechanisms in the 193 nm photodissociation of AsH_3 , as well as its nascent photofragments, is difficult for several reasons. First, the photon energy exceeds greatly the bond dissociation energies of AsH_3 and AsH_2 , thereby enabling highly internally excited fragments to be produced, with a multitude of possible reaction channels. Second, theoretical calculations

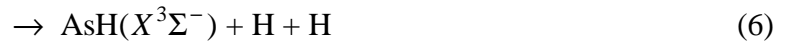
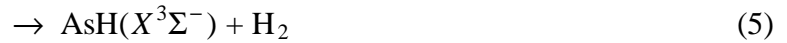
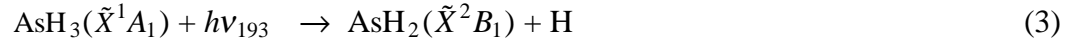
on AsH_3 and AsH_2 are limited. Third, the presence of significant secondary photolysis adds an unappreciated subtlety to the assignment of the c.m. translational energy distribution. The eye is drawn to the peaks, yet the broad background contains nearly all of the signal, and therefore the real story. The above points compromise our ability to extract product internal energy distributions.

The goal of this section is a qualitative understanding of the photoinitiated decomposition dynamics of the AsH_3 system, in particular *vis-à-vis* its NH_3 and PH_3 counterparts. The NH_3 system has received a great deal of attention owing to its experimental accessibility and its relatively straightforward electronic structure. At the same time, it is important to examine heavier counterparts, and AsH_3 is a good candidate, as it lies intermediate between non-relativistic and relativistic regimes.

3.3.1 Primary Photolysis: $\text{AsH}_3 \rightarrow \text{AsH}_2 + \text{H}$

The $P(E_{\text{c.m.}})$ distribution shown in Fig. 6(a) is broad, with partially resolved structure and a maximum at low $E_{\text{c.m.}}$. Despite the presence of secondary photolysis, an estimate of the "center-of-gravity" of the distribution indicates that AsH_2 internal excitation accounts for $\sim 64\%$ of the available energy [*i.e.*, $E_{\text{avail}} = h\nu - D_0(\text{H}_2\text{As-H})$]. This is in agreement with the qualitative result of Koplitz *et al.*,²⁶ who reported that internal excitation accounts for $\sim 2/3$ of the available energy.

Following the absorption of a 193 nm (6.42 eV) photon, the following channels are energetically accessible (also see Fig. 3.2):



Given that $\text{AsH}_2(\tilde{A})$ lies $19\,909\text{ cm}^{-1}$ above $\text{AsH}_2(\tilde{X})$,²⁸ the maximum $E_{\text{c.m.}}$ that is compatible with reaction (4) is 5600 cm^{-1} (see Fig. 2). The distribution shown in Fig. 3.6 indicates that reaction (3) dominates, with high $\text{AsH}_2(\tilde{X})$ rovibrational excitation. This is reasonable in light of the photodissociation dynamics of PH_3 ¹⁹⁻²¹ and NH_3 .^{10-12,15}

Ultraviolet photoexcitation results in a change of equilibrium geometry. The $\text{AsH}_3(\tilde{X})$ electron configuration is $\dots(a_1)^2(e)^4(a_1)^2$, and the equilibrium value of the $\theta_{\text{H-As-H}}$ angle is 92.1° .²⁵ According to the Walsh diagram for this system, promotion of an

a_1 lone pair electron to the Rydberg a_1 orbital increases the $\theta_{\text{H-As-H}}$ equilibrium angle.³⁵ This will excite the ν_2 umbrella mode, as in the analogous $\tilde{A} \leftarrow \tilde{X}$ transitions in NH_3 and PH_3 .^{7,17} It should be noted that the promotion of an a_1 lone pair electron to other excited orbitals in this energy region might also result in umbrella mode excitation.

The photoinitiated dissociation dynamics of NH_3 provides insight. The NH_3 $\tilde{A} \leftarrow \tilde{X}$ absorption spectrum exhibits a resolved n_2 progression that reflects the pyramidal-to-planar geometry change. Experimental studies of the state selected (*i.e.*, ν_2') photodissociation of $\text{NH}_3(\tilde{A})$ confirm that NH_2 is formed with significant internal excitation that is primarily in the form of a -axis rotation.^{10,15} Not surprisingly, the amount of NH_2 internal excitation increases with photon energy. Moreover, excitation of the NH_2 bend has been observed following dissociation via higher ν_2' .^{12,14,15} Theory and experiment confirm that dissociation commencing from the \tilde{A} surface is sensitive to: (i) its vibrational state; (ii) geometries and motions sampled during fragmentation; (iii) the topography of the conical intersection region; and (iv) competition between adiabatic and nonadiabatic pathways.^{5-12,14,15}

Dissociation to ground electronic state products is governed by the \tilde{A}/\tilde{X} conical intersection. For example, trajectory calculations of Biesner *et al.* illustrate the intersection's influence on energy disposal into product degrees of freedom.¹⁰ Referring to Fig. 1, trajectories are funneled toward the intersection, and nonadiabatic transitions are facilitated by near-planar geometry. Dissociation to $\text{NH}_2(\tilde{X})$ can occur either on the first pass through the intersection region or, if this fails, on a subsequent pass. The intersection

region has a large gradient in the angular coordinate, and this promotes $\text{NH}_2(\tilde{X})$ a -axis rotation. Trajectories that fail to emerge on the $\text{NH}_2(\tilde{A})$ asymptote in the first pass through the conical intersection region can sample more of the \tilde{A} surface.¹⁰

Dissociation of NH_3 from higher ν_2' leads to NH_2 with larger amounts of vibrational and electronic excitation.^{12,15} Competition ensues between adiabatic and nonadiabatic pathways once the threshold for $\text{NH}_2(\tilde{A})$ has been reached ($\nu_2' \geq 3$). $\text{NH}_3(\tilde{A})$ that dissociates via markedly nonplanar configurations, thereby avoiding the conical intersection region, does so on the surface that correlates to $\text{NH}_2(\tilde{A})$. Loomis *et al.* used time resolved Fourier transform infrared (FTIR) emission spectroscopy to investigate 193 nm NH_3 photodissociation.¹² They found a bimodal $\text{NH}_2(\tilde{A})$ rotational distribution that they attributed to near-planar and bent geometries that dissociate. Angular momentum conservation dictates that (for $J = 0$ parent) the angular momentum of NH_2 is equal and opposite the orbital angular momentum of the fragment pair.¹¹ Dissociation from $\text{NH}_3(\tilde{A})$ is rapid, *i.e.*, ~ 20 fs. Thus, out-of-plane bending is manifest as a -axis rotation of the $\text{NH}_2(\tilde{A})$ product.¹²

3.3.2 AsH₂ Internal Excitations

Given that a 193 nm photon prepares $\text{AsH}_3(\tilde{A})$ with significant ν_2 (umbrella) vibrational excitation, and in light of the similarities between AsH_3 and PH_3 and between AsH_2 and PH_2 , it is reasonable to expect the participating pathways and dissociation

dynamics of AsH_3 to resemble those of PH_3 . For example, consider the different $\theta_{\text{H-M-H}}$ equilibrium values that exist between parent and product species. The equilibrium values of $\theta_{\text{H-P-H}}$ for $\text{PH}_3(\tilde{A})$ and $\text{PH}_2(\tilde{X})$ are 114° and 91.4° , respectively.^{16,36} This large difference of 22.6° can lead to significant bending excitation in the $\text{PH}_2(\tilde{X})$ product that accrues via the diabatic surface that correlates $\text{PH}_3(\tilde{A})$ to $\text{PH}_2(\tilde{X})$.

Note that, in this regard, PH_3 differs (perhaps significantly) from NH_3 . The equilibrium values of $\theta_{\text{H-N-H}}$ for $\text{NH}_3(\tilde{A})$ and $\text{NH}_2(\tilde{X})$ are 120° and 103.4° ,⁵ respectively: a change of 16.6° . This is 6° less than the 22.6° change that occurs with PH_3 . Without a detailed calculation, however, it is not feasible to infer the degree of vibrational excitation present in the triatom product given the $\theta_{\text{H-M-H}}$ equilibrium angles for a parent and its triatom product. Specifically, though the angular change in going from parent to products is large, the degree of vibrational adiabaticity along the reaction coordinate must be assessed.

Because of this vibrational adiabaticity, differences of 22.6° versus 16.6° might result in larger fractional differences in the degree of triatom bending excitation. For example, Lambert *et al.* observed PH_2 with substantial bending excitation and a -axis rotation following the ultraviolet photolysis of PH_3 .¹⁹ In contrast, it is known that NH_2 is formed with a relatively modest amount of bending excitation.^{10-12,15}

The equilibrium bond angles for $\text{AsH}_3(\tilde{A})$ and $\text{AsH}_2(\tilde{X})$ are 112° (an estimate based on AsH_3^+ and $\text{PH}_3(\tilde{A})$) and 90.4° ,³⁷ respectively. These values and their 21.6°

difference are close to those of their PH_3 counterparts (114° , 91.4° , 22.6° , respectively). Thus, it is reasonable to expect AsH_2 to be formed with high internal excitation, specifically, a -axis rotation and bending excitation.

This is consistent with our data. The structure in the $P(E_{\text{c.m.}})$ distribution at low translational energies [Fig. 3.6(b)] is consistent with $\text{AsH}_2(\tilde{X})$ having significant a -axis rotation. For example, to rationalize the peaks in Fig. 3.6(b), rotational energies for $\text{AsH}_2(\tilde{X})$, which is a near-oblate top ($\kappa = 0.8034$),²⁸ were calculated using the formula:

$$F(J, K_c) = \bar{B}J(J + 1) + (C - \bar{B})K_c^2 \quad (13)$$

where

$$\bar{B} = (A + B)/2 \quad (14)$$

Values of rotational constants: A , B , and C are 7.550 , 7.162 , and 3.615 cm^{-1} , respectively,²⁸ and $F(J, K_c)$ is the rotational energy.

Energy separations between calculated rotational levels matched the lower-energy spacings in Fig. 3.6(b). The structure below 5000 cm^{-1} is fit with J values in the range 46-54, as indicated in Fig. 3.7. The large amount of $\text{AsH}_2(\tilde{X})$ internal energy, the complex energy disposal, and the scarcity of spectroscopic data make unique assignment impossible. Other sets of rotational levels also fit the data. However, the peaks cannot be fit using any reasonable choice of vibrational frequencies. Moreover, the established propensity toward a -axis rotation is consistent with low K_c values. For example, including K_c values up to 10 does not alter the fit to the data indicated in Fig. 3.7.

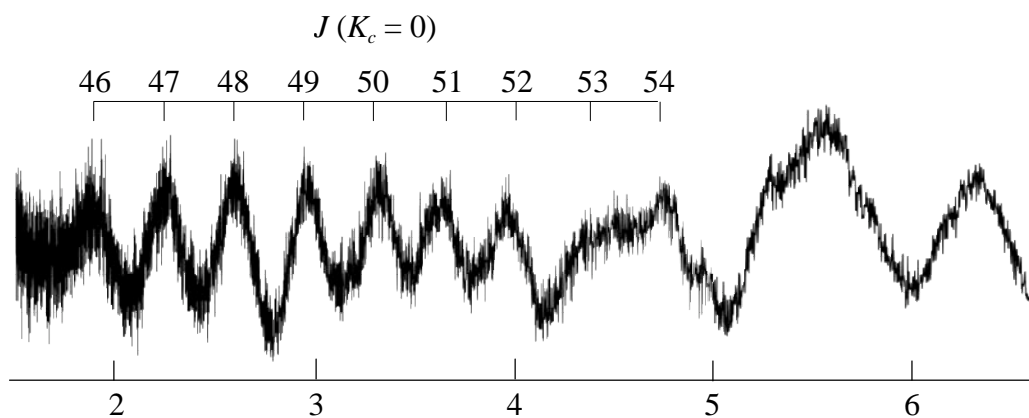


Figure 3.7 Low energy features can be fit using high J values and various distribution of low K_c values.

Figure 3.6(c) highlights the structure present at the higher $E_{c.m.}$ values. Separations between peaks (though the data are of low S/N) are comparable to the bend of $\text{AsH}_2(\tilde{X})$.²⁸ Why does this structure occur at higher translational energy? Again, qualitative guidance is available from NH_3 . $\text{NH}_3(\tilde{A})$ that retains near- C_{2v} symmetry during dissociation passes through the conical intersection region to form $\text{NH}_2(\tilde{X})$ in low rotational states.¹⁰ Loomis *et al.* used an impulsive model to rationalize the efficient disposal of energy into NH_2 bending excitation for planar dissociation.¹² $\text{AsH}_3(\tilde{A})$ that remains near-planar during dissociation has a high probability of undergoing a nonadiabatic transition. The resulting $\text{AsH}_2(\tilde{X})$ will have bending excitation because of the change in equilibrium bond angle in going from $\text{AsH}_3(\tilde{A})$ to $\text{AsH}_2(\tilde{X})$, but less a -axis rotation than molecules that dissociate having considerable umbrella mode excitation.

Adiabatic and nonadiabatic transitions compete. $\text{AsH}_2(\tilde{A})$ arises from $\text{AsH}_3(\tilde{A})$ that dissociates mainly from geometries that avoid the conical intersection region. Therefore, $\text{AsH}_2(\tilde{A})$ is expected to have a -axis rotational excitation. Though the equilibrium angles of $\text{AsH}_3(\tilde{A})$ and $\text{AsH}_2(\tilde{A})$ (112° and 123° , respectively)^{24,37} differ by a smaller amount than for $\text{AsH}_3(\tilde{A})$ and $\text{AsH}_2(\tilde{X})$ (112° and 90.4° , respectively),^{24,37} it is not unreasonable to anticipate $\text{AsH}_2(\tilde{A})$ bending excitation.

$\text{AsH}_2(\tilde{A})$ is a near-prolate top ($\kappa = -0.8249$).²⁸ Rotational energies were estimated using: $F(J, K_a) = \bar{B}J(J+1) + (A - \bar{B})K_a^2$, where $\bar{B} = (B - C)/2$, and A , B , and C values are 17.207, 4.920, and 3.740 cm^{-1} .²⁸ Peak separations in Fig. 6(b) could not be fit using these calculated spacings.

3.3.3 Secondary Photolysis: $\text{AsH}_2 \rightarrow \text{AsH} + \text{H}$

Our considerations here are restricted to secondary photolysis processes that yield H atom fragments. Channels that yield H_2 are not considered. Figures 3.4-3.6 indicate that the photodissociation of AsH_3 yields AsH_2 with significant internal excitation, and that this species is photolyzed. Energy conservation requires:

$$h\nu_{193} + E_{\text{AsH}_2} - D_0(\text{HAs-H}) = E_{\text{AsH}} + E_{\text{c.m.}} \quad (17)$$

where E_{AsH_2} and E_{AsH} are the internal energies of AsH_2 and AsH , respectively. For those (infrequent) instances in which $E_{\text{AsH}_2} \approx D_0(\text{HAs-H})$ and E_{AsH} is negligible, $E_{\text{c.m.}}$ is approximately equal to $h\nu_{193}$. In this case, the photon energy ($51,780 \text{ cm}^{-1}$) appears as

$E_{c.m.}$. Indeed, the inset in Fig. 6(a) indicates a fairly abrupt termination of $P(E_{c.m.})$ at $51\,800 \pm 500\text{ cm}^{-1}$. This is also easy to see in the TOF spectrum in Fig. 3.4. Namely, the arrival time for which $E_{c.m.} = h\nu_{193}$ is $12.4\ \mu\text{s}$, which coincides with the sharp onset of signal in the TOF spectrum. Thus, AsH_2 is formed with a distribution of internal energies that extends all the way up to $D_0(\text{HAs-H})$.

Many channels are accessible when AsH_2 absorbs a 193 nm photon. Referring to Fig. 3.2, photodissociation of $\text{AsH}_2(\tilde{X})$ from even its lowest rovibrational level can, on energetic grounds, access a number of product channels. Because AsH_2 contains significant internal excitation, the possibilities are legion.

Though $\text{AsH}(a^1\Delta)$ and $\text{AsH}(b^1\Sigma^+)$ are energetically accessible via secondary photolysis, emission from these species has not been observed following 193 nm excitation.²⁷ This can be due to the fact that singlet-triplet emission is weak, or that these channels are not accessed. $\text{AsH}(A^3\Pi)$ is energetically accessible when $\text{AsH}_2(\tilde{X})$ contains more than 1500 cm^{-1} of internal energy prior to its photoexcitation. Nonetheless, $\text{AsH}(A^3\Pi)$ has not been detected in emission following 193 nm photolysis of AsH_3 .

Photodissociation of $\text{AsH}_2(\tilde{X})$ that has $E_{\text{AsH}_2} \leq D_0(\text{HAs-H})$ can, on energetic grounds, yield $\text{AsH}(X)$ and $\text{AsH}(A)$ with $E_{c.m.} \leq 51\,700\text{ cm}^{-1}$ and $\leq 21\,700\text{ cm}^{-1}$, respectively. The $E_{c.m.}$ distribution in Fig. 6 is broad, peaking at $\sim 6\,000\text{ cm}^{-1}$. Vibrational excitation in AsH is expected to be modest on the basis of changes of bond lengths: $1.483\ \text{\AA}$ in $\text{AsH}_2(\tilde{A})$;³⁷ $1.534\ \text{\AA}$ in $\text{AsH}(X)$;³⁰ $1.577\ \text{\AA}$ in $\text{AsH}(A)$.³⁰ Though PES's are not available, possible pathways can be considered in light of symmetry and

spin.³⁷ $\text{AsH}_2(\tilde{X}^2B_1)$ and $\text{AsH}_2(\tilde{B}^4B_1)$ correlate to $\text{AsH}(X^3\Sigma^-) + \text{H}(^2S)$, whereas $\text{AsH}_2(\tilde{A}^2A_1)$ does not correlate to $\text{AsH}(X^3\Sigma^-)$. For PH_2 , it has been noted that \tilde{A} may predissociate via 4B_1 because of spin-orbit interaction.³⁸ However, 4B_1 is much higher in energy than 2A_1 , so predissociation of 2A_1 via 4B_1 is considered unlikely in the present experiments.

3.4 Conclusions

HRTOF spectroscopy has been used to examine the 193 nm photodissociation of AsH_3 . Contributions from secondary AsH_2 photodissociation are also present. The degree of secondary photodissociation can be minimized, but not eliminated, by using low 193 nm fluences. The experimental method is only sensitive to product channels that give H atoms, *i.e.*, an elimination channel such as $\text{AsH}_2 \rightarrow \text{As} + \text{H}_2$ cannot be detected using the present arrangement. The main experimental result is a broad $P(E_{\text{c.m.}})$ distribution that contains a modest amount of superimposed structure.

The dominant reaction pathway is $\text{AsH}_3 \rightarrow \text{AsH}_2(\tilde{X}) + \text{H}$. Nascent $\text{AsH}_2(\tilde{X})$ has considerable rovibrational excitation. The average value of E_{AsH_2} is $\approx 16\,300\text{ cm}^{-1}$, which is $\approx 64\%$ of the available energy: $E_{\text{avail}} = h\nu - D_0(\text{H}_2\text{As-H})$. The distribution of E_{AsH_2} values extends to values as large as $D_0(\text{HAs-H})$. For those cases in which $E_{\text{AsH}_2} \approx D_0(\text{HAs-H})$ and E_{AsH} is negligible, AsH_2 photodissociation yields $E_{\text{c.m.}} \approx h\nu_{193}$. This is manifest as a fairly abrupt termination of $P(E_{\text{c.m.}})$ at $51\,800 \pm 500\text{ cm}^{-1}$ [inset in

Fig. 3.6(a)], which matches $h\nu_{193} = 51780 \text{ cm}^{-1}$. This confirms that AsH_2 is formed with a distribution of internal energies that extends all the way to $\text{D}_0(\text{HAs-H})$.

It is known that $\text{AsH}_2(\tilde{\text{A}})$ is produced because its fluorescence has been detected,²⁷ though its yield could not be determined in the fluorescence measurements. In the present experiments, its yield is found to be modest. This follows from the fact that $E_{\text{c.m.}}$ must be $\leq 5600 \text{ cm}^{-1}$ for the $\text{AsH}_2(\tilde{\text{A}})$ channel (Fig. 3.2), and this energy range accounts for a modest fraction of the observed $P(E_{\text{c.m.}})$ distribution. Thus, most of the reactive flux passes from electronically excited AsH_3 to ground electronic state products, presumably via a nonadiabatic transition mechanism similar to those of PH_3 and NH_3 .

The 193 nm photolysis of AsH_3 has much in common with that of PH_3 . On the basis of the PH_3 experimental data and known PH_3 , PH_2 , AsH_3 , and AsH_2 geometrical properties, AsH_2 bending excitation is expected. For example, note the differences between equilibrium angles $\theta_{\text{H-M-H}}$: $114^\circ \rightarrow 91.4^\circ$ for $\text{PH}_3(\tilde{\text{A}}) \rightarrow \text{PH}_2(\tilde{\text{X}})$; and $112^\circ \rightarrow 90.4^\circ$ for $\text{AsH}_3(\tilde{\text{A}}) \rightarrow \text{AsH}_2(\tilde{\text{X}})$. The separations between adjacent peaks in the structure present in the *high-energy* region of the $P(E_{\text{c.m.}})$ distribution [Fig. 3.6(c)] are in qualitative accord with $\text{AsH}_2(\tilde{\text{X}})$ bending quanta.

Separations between adjacent peaks in the *low-energy* region of the $P(E_{\text{c.m.}})$ distribution are in accord with $\text{AsH}_2(\tilde{\text{X}})$ rotational levels. This is consistent with a mechanism in which parent umbrella motion evolves to *a*-axis rotation of the $\text{AsH}_2(\tilde{\text{X}})$ product, as occurs with the lighter group-V hydrides.

Theory is in good shape for NH_3 , but the same is not true for AsH_3 . Accurate electronic structure calculations will go a long way toward elucidating mechanisms and provide a detailed quantitative understanding of the photophysics and photochemistry of the full range of group-V hydrides. It is imperative that calculations for the heavier species are done at a high level of theory if experimental results are to be reconciled with confidence.

3.5 Chapter 3 References

1. Donnelly, V. M.; Karlicek, R. F. *J. Appl. Phys.* **1982**, *53*, 6399.
2. Pütz, N.; Heinecke, H.; Veuhoff, E.; Arens, G.; Heyen, M.; Lüth, H.; Balk, P. *J. Cryst. Growth* **1984**, *68*, 194.
3. Kukimoto, H.; Ban, Y.; Komatsu, H.; Takechi, M.; Ishizaki, M. *J. Cryst. Growth* **1986**, *77*, 223.
4. Aoyagi, Y.; Kanazawa, M.; Doi, A.; Iwai, S.; Namba, S. *J. Appl. Phys.* **1986**, *60*, 3131.
5. McCarthy, M. I.; Rosmus, P.; Werner, H. J.; Botshwina, P.; Vaida, V. *J. Chem. Phys.* **1987**, *86*, 6693.
6. Ranu, R.; Peyerimhoff, S. D.; Buenker, R. J. *J. Mol. Spectrosc.* **1977**, *68*, 253.
7. Rosmus, P.; Botschwina, P.; Werner, H. J.; Vaida, V.; Engelking, P. C.; McCarthy, M. I. *J. Chem. Phys.* **1987**, *86*, 6677.
8. Nangia, S.; Truhlar, D. G. *J. Chem. Phys.* **2006**, *124*, 124309.
9. Vaida, V.; McCarthy, M. I.; Engelking, P. C.; Rosmus, P.; Werner, H. J.; Botschwina, P. *J. Chem. Phys.* **1987**, *86*, 6669.
10. Biesner, J.; Schnieder, L.; Ahlers, G.; Xie, X.; Welge, K. H.; Ashfold, M. N. R.; Dixon, R. N. *J. Chem. Phys.* **1988**, *88*, 3607.
11. Mordaunt, D.; Ashfold, M. N. R.; Dixon, R. N. *J. Chem. Phys.* **1996**, *104*, 6460.
12. Loomis, R. A.; Reid, J. P.; Leone, S. *J. Chem. Phys.* **2000**, *112*, 658.
13. Kassab, E.; Gleghorn, J. T.; Evleth, E. M. *J. Am. Chem. Soc.* **1983**, *105*, 1746.
14. Hause, M. L.; Yoon, Y. H.; Crim, F. F. *J. Chem. Phys.* **2006**, *125*, 174309.
15. Biesner, J.; Schnieder, L.; Ahlers, G.; Xie, X.; Welge, K. H.; Ashfold, M. N. R.; Dixon, R. N. *J. Chem. Phys.* **1989**, *91*, 2901.
16. Müller, J.; Ågren, H. *J. Chem. Phys.* **1982**, *76*, 5060.

17. Humphries, C. M.; Walsh, A. D.; Warsop, P. A. *Discuss. Faraday Soc.* **1963**, 35, 148.
18. Maripuu, R.; Reineck, I.; Ågren, H.; Nian-Zu, W.; Rong, J. M.; Veenhuizen, H.; Al-Shamma, S. H.; Karlsson, L.; Siegbahn, K. *Mol. Phys.* **1983**, 48, 1255.
19. Lambert, I. R.; Morley, G. P.; Mordaunt, D. H.; Ashfold, M. N. R.; Dixon, R. N. *Can. J. Chem.* **1994**, 72, 977.
20. Baugh, D.; Koplitz, B.; Xu, Z.; Wittig, C. *J. Chem. Phys.* **1988**, 88, 879.
21. Sam, C. L.; Yardley, J. T. *J. Chem. Phys.* **1978**, 69, 4621.
22. Berkowitz, J. *J. Chem. Phys.* **1988**, 89, 7065.
23. Potts, A. W.; Price, W. C. *Proc. R. Soc. London Ser. A.* **1972**, 326, 181.
24. Dai, D.; Balasubramanian, K. *J. Chem. Phys.* **1990**, 93, 1837.
25. Binning Jr., R. C.; Curtiss, L. A. *J. Chem. Phys.* **1990**, 92, 1860.
26. Koplitz, B.; Xu, Z.; Wittig, C. *Appl. Phys. Lett.* **1988**, 52, 860.
27. Ni, T.; Lu, Q.; Ma, X.; Yu, S.; Kong, F. *Chem. Phys. Lett.* **1986**, 126, 417.
28. He, S.-G.; Clouthier, D. J. *J. Chem. Phys.* **2007**, 126, 154312.
29. Balasubramanian, K.; Nannegari, V. *J. Mol. Spectrosc.* **1989**, 138, 482.
30. Dixon, R. N.; Lamberton, H. M. *J. Mol. Spectrosc.* **1968**, 25, 12.
31. Aren, M.; Richter, W. *J. Chem. Phys.* **1990**, 93, 7094.
32. Buetel, M.; Setzer, K. D.; Shestakov, O.; Fink, E. H. *J. Mol. Spectrosc.* **1996**, 178, 165.
33. Moore, C. E. *Atomic Energy Levels*; National Bureau of Standards: Washington, DC, 1971.
34. Zhang, J.; Riehn, C. W.; Dulligan, M.; Wittig, C. *J. Chem. Phys.* **1996**, 104, 7027.

35. Walsh, A. D. *J. Chem. Soc.* **1953**, 2296.
36. Berthou, J. M.; Pascat, B.; Guenebaut, H.; Ramsay, D. A. *Can. J. Phys.* **1972**, *50*, 2265.
37. Dixon, R. N.; Duxbury, G.; Lamberton, H. M. *Proc. R. Soc. London Ser. A.* **1968**, *305*, 271.
38. Xuan, C. N; Margani, A. *J. Chem. Phys.* **1994**, *100*, 7000.

Chapter 4

Future Directions

The previous chapters have discussed the photochemistry of NH_3 , PH_3 and AsH_3 . Attention must also be given to the heavier group-V hydrides, SbH_3 and BiH_3 . Section 4.1 introduces SbH_3 . The SbH_3 room temperature absorption spectrum and recent results from high- n Rydberg hydrogen time-of-flight (HRTOF) experiments are presented in the subsections. Sections 4.2 and 4.2 detail future HRTOF experiments on BiH_3 and the group-V dihydrides, respectively.

4.1 SbH₃

The experimental study of antimony trihydride (stibine), SbH₃, presents the next challenge in our quest to understand the molecular properties and photochemistry of the group-V hydrides. Antimonide materials are used to form infrared optoelectronic and III-V semiconductor devices (*e.g.* AlSb, GaSb, InSb, and ZnSb, etc.).¹⁻⁴ Photolytic processes are often utilized to initiate and control the growth of these semiconductor compounds during metalorganic chemical vapor deposition (MOCVD).^{1,2} SbH₃ is a possible Sb-precursor, however, complications arise due to its thermal instability. Deuterated stibine exhibits greater thermal stability relative to SbH₃ and is a promising Sb-source for MOCVD.⁵ In light of our scientific interest in the group-V hydrides, only SbH₃ was considered.

The amount of experimental and theoretical research on SbH₃ is limited compared to its lighter group-V counterparts. SbH₃ is an unpopular experimental candidate due to safety and sample preparation/handling issues. SbH₃ is a highly toxic, colorless gas (OSHA permissible exposure limit is 0.1 ppm)⁶ that can undergo autocatalytic decomposition at temperatures as low as -65°C,⁵ yielding antimony metal films and hydrogen gas. The large number of electrons and necessary inclusion of relativistic effects complicate theoretical calculations. At present, there is no information regarding dissociation pathways on the \tilde{X} and \tilde{A} potential energy surfaces (PESs) of SbH₃.

The electronic configurations of NH₃(\tilde{X}), PH₃(\tilde{X}), AsH₃(\tilde{X}) and SbH₃(\tilde{X}) are $\dots(a_1)^2(e)^4(a_1)^2$.^{3,7,8} The $\tilde{A} \leftarrow \tilde{X}$ transitions for these group-V hydrides involve promotion of the highest occupied lone pair electron to a Rydberg a_1 (a_2'' in the planar

D_{3h} limit) orbital.^{3,7,8} The $\text{NH}_3 \tilde{A} \leftarrow \tilde{X}$ absorption band displays a well-resolved progression in the ν_2 umbrella mode, which reflects the planar \leftarrow pyramidal geometry change.⁹ In contrast, the $\tilde{A} \leftarrow \tilde{X}$ absorption spectra for PH_3 , AsH_3 and SbH_3 exhibit broad continua.¹⁰ Analyses of the PH_3 , AsH_3 and SbH_3 absorption spectra reveal that $\nu'_2 \sim \nu''_2 / 2$, whereas $\nu'_2 \sim \nu''_2$ for NH_3 .¹⁰ This finding lead Humphries *et. al.* to suggest that the \tilde{A} states of PH_3 , AsH_3 and SbH_3 are slightly pyramidal with transitions terminating on vibrational levels well above the inversion barrier.¹⁰ The ground states of PH_3^+ , AsH_3^+ , and SbH_3^+ are nonplanar ($\theta_{H-M-H} \sim 114^\circ$, 112° and 110.5° for $M = \text{P}$, As and Sb , respectively)^{3,11-13}, thus it is reasonable to assume that $\text{PH}_3(\tilde{A})$, $\text{AsH}_3(\tilde{A})$ and $\text{SbH}_3(\tilde{A})$ are also nonplanar. Regardless, the $\tilde{A} \leftarrow \tilde{X}$ transitions for NH_3 , PH_3 , AsH_3 and SbH_3 are all accompanied by considerable changes in the equilibrium bond angle, (Table 4.1) resulting in significant ν_2 vibrational excitation.^{9,10}

The dissociation dynamics of $\text{NH}_3(\tilde{A})$ have been exhaustively studied.^{7,9,15-17} $\text{NH}_3(\tilde{A})$ is quasibound for the $\nu_2 = 1$ and $\nu_2 = 2$ vibrational levels; dissociation occurs *via* tunneling through an energy barrier.^{7,9} The height of this barrier is dependent on the out-of-plane bend angle, with a minimum at planar geometries. Dissociation from $\text{NH}_3(\tilde{A})$ is greatly influenced by the \tilde{X}/\tilde{A} conical intersection and can occur *via* nonadiabatic and adiabatic pathways:^{7,15-17}

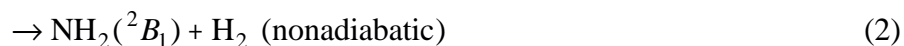
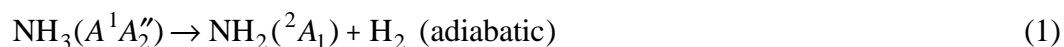


Table 4.1 Equilibrium H-M-H angles for N, P, As and Sb and related electronic states.*

$\text{NH}_3(\tilde{X}^1A_1)$	107°	
$\text{NH}_3(\tilde{A}^1A_2'')$	120°	$\text{NH}_3(\tilde{A}) \rightarrow \text{NH}_2(\tilde{X})$
$\text{NH}_2(\tilde{X}^2B_1)$	103.4°	$\theta_{\text{H-N-H}}^{\text{equil}} : 120^\circ \rightarrow 103.4^\circ$
$\text{NH}_2(\tilde{A}^2A_1)$	144°	
$\text{PH}_3(\tilde{X}^1A_1)$	93.5°	
$\text{PH}_3(\tilde{A}^1A_1)$	114°	$\text{PH}_3(\tilde{A}) \rightarrow \text{PH}_2(\tilde{X})$
$\text{PH}_2(\tilde{X}^2B_1)$	91.4°	$\theta_{\text{H-P-H}}^{\text{equil}} : 114^\circ \rightarrow 91.4^\circ$
$\text{PH}_2(\tilde{A}^2A_1)$	123.1°	
$\text{AsH}_3(\tilde{X}^1A_1)$	92.1°	
$\text{AsH}_3(\tilde{A}^1E)$	112°	$\text{AsH}_3(\tilde{A}) \rightarrow \text{AsH}_2(\tilde{X})$
$\text{AsH}_2(\tilde{X}^2B_1)$	90.4°	$\theta_{\text{H-As-H}}^{\text{equil}} : 112^\circ \rightarrow 90.4^\circ$
$\text{AsH}_2(\tilde{A}^2A_1)$	123°	
$\text{SbH}_3(\tilde{X}^1A_1)$	91.5°	
$\text{SbH}_3(\tilde{A}^1E)$	110.5°	$\text{SbH}_3(\tilde{A}) \rightarrow \text{SbH}_2(\tilde{X})$
$\text{SbH}_2(\tilde{X}^2B_1)$	89.8°	$\theta_{\text{H-Sb-H}}^{\text{equil}} : 110.5^\circ \rightarrow 89.8^\circ$
$\text{SbH}_2(\tilde{A}^2A_1)$?	

*See text for details and references

It should be noted that at $v_2 \geq 3$, there is sufficient energy to produce $\text{NH}_2(^2A_1)$. Experimental studies have found that the NH_2 products are born with significant internal excitation, primarily in the form of a -axis rotation. The topography of the \tilde{A} PES near the conical intersection enhances NH_3 out-of-plane bending motion, leading to considerable NH_2 a -axis rotation; whereas, near-planar dissociation leads to modest NH_2 a -axis rotation.^{7,15-17}

The $\text{NH}_3(\tilde{A})$, $\text{PH}_3(\tilde{A})$ and $\text{AsH}_3(\tilde{A})$ PESs are qualitatively similar. Theoretical calculations indicate a small potential barrier on $\text{PH}_3(\tilde{A})$, the height of which is comparable to the zero-point energy of the stretching vibration.¹⁸ The $\text{PH}_3 \tilde{A} / \tilde{X}$ conical intersection is presumed to affect the dissociation dynamics akin to the case of NH_3 . There is inadequate information regarding the \tilde{X} and \tilde{A} surfaces of AsH_3 ; however, in consideration of group trends, it is supposed that there is also a small barrier to dissociation on \tilde{A} and an \tilde{A} / \tilde{X} conical intersection.¹⁸

The photodissociation dynamics of PH_3 and AsH_3 mirror those of NH_3 with a few notable differences. HRTOF spectroscopy has been used to investigate the UV photolysis of PH_3 and AsH_3 .^{8,14} Structured translational energy distributions indicate that the internal excitation of $\text{PH}_2(\tilde{X})$ and $\text{AsH}_2(\tilde{X})$ accounts for $\sim 62\%$ and $\sim 64\%$ of the available energy [*i.e.* $h\nu - D_0(\text{H}_2\text{P} - \text{H} / \text{H}_2\text{As} - \text{H})$], respectively. The PH_2 and AsH_2 products are formed with significant a -axis rotation, as well as bending excitation. The change in bond angle from $\text{PH}_3(\tilde{A})$ to $\text{PH}_2(\tilde{X})$ and $\text{AsH}_3(\tilde{A})$ to $\text{AsH}_2(\tilde{X})$ is suggested as a plausible source for the product vibrational excitation.^{8,14}

It is reasonable to assume that the photodissociation dynamics of $\text{SbH}_3(\tilde{A})$ will exhibit marked similarities with PH_3 and AsH_3 . It should be noted that calculations of the lowest excited singlet surfaces indicate that $\text{SbH}_3(\tilde{A})$ and $\text{AsH}_3(\tilde{A})$ have E symmetry, which differs from the lowest excited singlets of NH_3 and PH_3 .^{3,7,18} An $\text{SbH}_2 \tilde{A} \rightarrow \tilde{X}$ emission spectrum has been recorded by Ni *et. al.* following the 193.3 nm photolysis of SbH_3 .¹⁹ Formation of an antimony coating on the input windows hampered the transmission of the photolysis radiation, limiting their experimental resolution. However, their results indicated that $\text{SbH}_2(\tilde{A}^2A_1)$ was formed in highly-excited vibrational states. Emission from nascent Sb atoms ($6s \rightarrow 5p$) was also observed using 193.3 nm and 248 nm photolysis radiation. Photolysis of SbH_2 was suggested as a possible mechanism for the Sb emission.¹⁹ It is interesting to note that the 248 nm photolysis of AsH_3 yielded no detectable fluorescence.²⁰

In a preliminary study, we successfully synthesized SbH_3 and obtained the room temperature UV absorption spectrum. HRTOF spectroscopy was also employed to examine the 193.3 photodissociation of SbH_3 . Figure 4.1 shows the possible products from primary and secondary photolysis processes. Unfortunately, results from the HRTOF experiment were inconclusive. This will be discussed later.

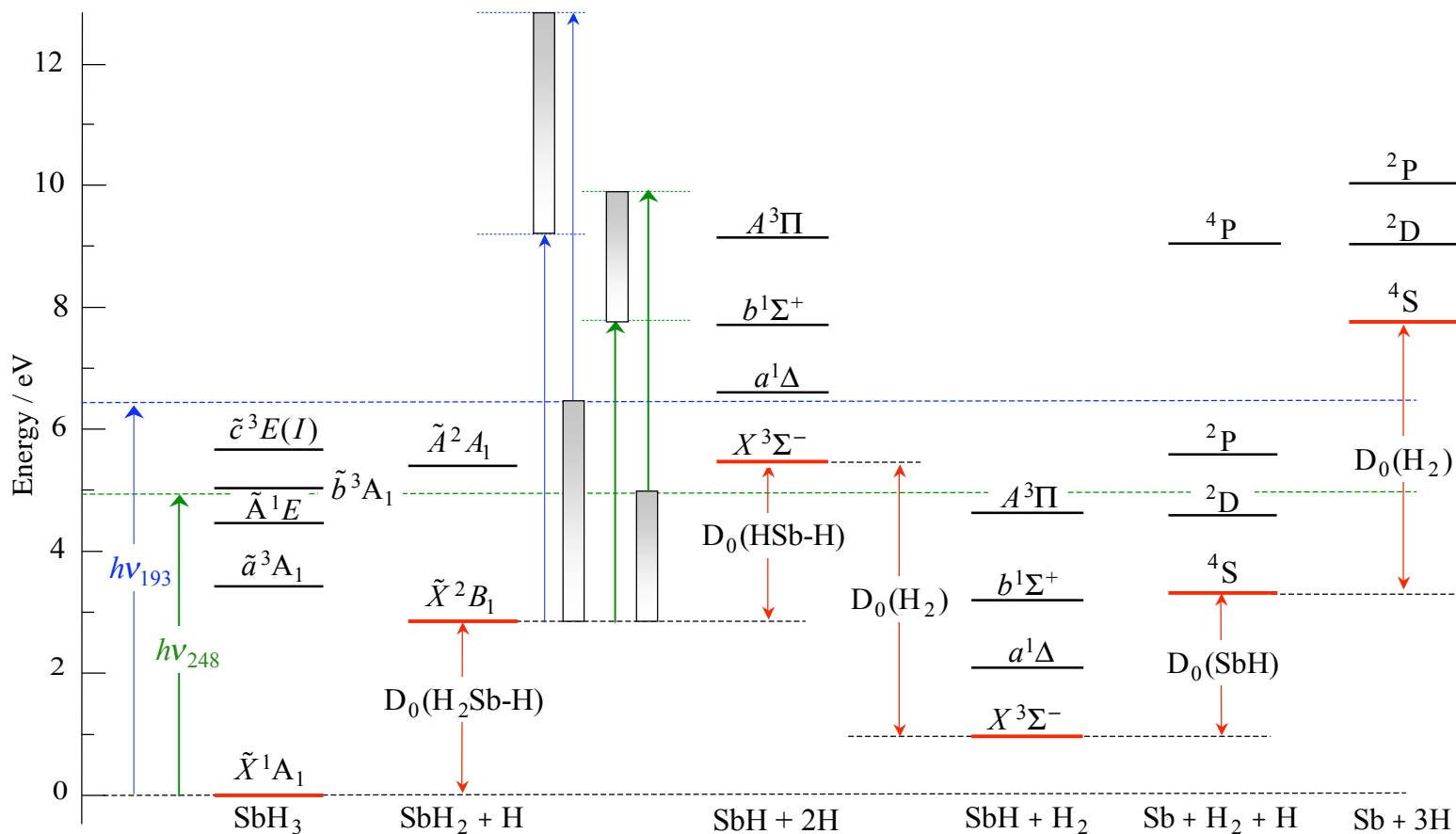
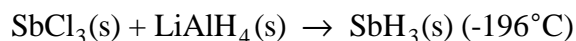


Figure 4.1 Energy level diagram for the 193.3 and 248 nm photolysis of SbH_3 . The 193 nm photon energy is significantly greater than the SbH_3 bond dissociation energy. The product species that can undergo secondary photodissociation are also shown. The shaded rectangles indicate possible energy ranges for internally excited SbH_2 . The spin-orbit SbH states are not shown here.^{3,4,21,2}

4.1.1 SbH₃ Synthesis

SbH₃ (mp -88°C, bp -18°C) was synthesized via a nonaqueous method reported by M.A. Todd *et. al.*⁵ This synthesis has been shown to be highly efficient, with a product yield of ~ 85%. SbH₃ was generated from the reaction between antimony chloride and lithium aluminum hydride in tetraethylene glycol dimethyl ether (tetraglyme):



All reagents were purchased from Alfa Aesar and used as received. The reaction apparatus was attached to a vacuum line and all glassware was passivated using warm methyl acetate, dried and evacuated prior to use.

The reaction apparatus consisted of a 500-ml beaker equipped with an addition funnel. The reaction vessel was attached to a purification and collection trap maintained at -40°C and -196°C, respectively. A suspension of LiAlH₄(s) (0.52 g) in 100 ml of tetraglyme was prepared in the 500-ml beaker equipped with a stir bar. SbCl₃ suspended in 50 ml of tetraglyme was added to the addition funnel. The reaction vessel was cooled *via* an acetone/dry ice bath and the entire setup was evacuated and held under vacuum for the duration of the reaction.

The addition of SbCl₃ initiated the reaction. The suspension in the reaction vessel turned black and bubbled violently, evidence of SbH₃(g) formation. After passing through the purification trap, SbH₃(s) appeared as a grayish-white solid on the walls of the collection trap. When the reaction was complete (~ 30 minutes), the collection trap was sealed off and removed from the apparatus. The SbH₃ sample was not light sensitive and the lifetime was ~ 1.5 hours at room temperature.

4.1.2. Ultraviolet Absorption Spectrum of SbH_3

A specially-designed UV-Vis cell with quartz (KU1 grade) windows was attached to the collection trap and a vacuum line. After the UV-Vis cell was evacuated, the liquid nitrogen Dewar was removed from the collection trap to allow sublimation to occur. Once $\text{SbH}_3(\text{g})$ collected in the UV-Vis cell, the cell was sealed off and the room temperature ultraviolet absorption spectrum was recorded using a Varian Carey Series 300 spectrophotometer (resolution ~ 0.2 nm). The UV absorption spectrum of SbH_3 is shown in Figure 4.2. There is evidence of a long wavelength tail extending to ~ 280 nm.

The long wavelength tail in the absorption spectrum may arise from relativistic effects. As a result of the large nuclear charge in SbH_3 , the core electrons travel at a considerable fraction of the speed of light. In order to offset the increased kinetic energy, the radii of the core electron orbitals decrease and orbital energies are lowered.^{22,23} This orbital contraction shields the nuclear charge from the valence electrons, affecting the orbital energies and the photochemistry of SbH_3 .

4.1.3 High- n Rydberg Time-of-flight Experiments

HRTOF spectroscopy was used to study the 193.3 nm photolysis of SbH_3 . The HRTOF apparatus was discussed in detail in chapter 3, so only relevant details are presented here. Following the synthesis of $\text{SbH}_3(\text{s})$, the collection vessel, cooled by the liquid nitrogen trap, was attached to a vacuum line and the molecular beam foreline. The foreline was evacuated and the liquid nitrogen trap was slowly lowered. Hydrogen gas (Gilmore Liquid Air, 99.999%) was passed through the collection trap and a molecular beam of SbH_3 (% unknown) in H_2 was expanded through a pulsed nozzle (General Valve

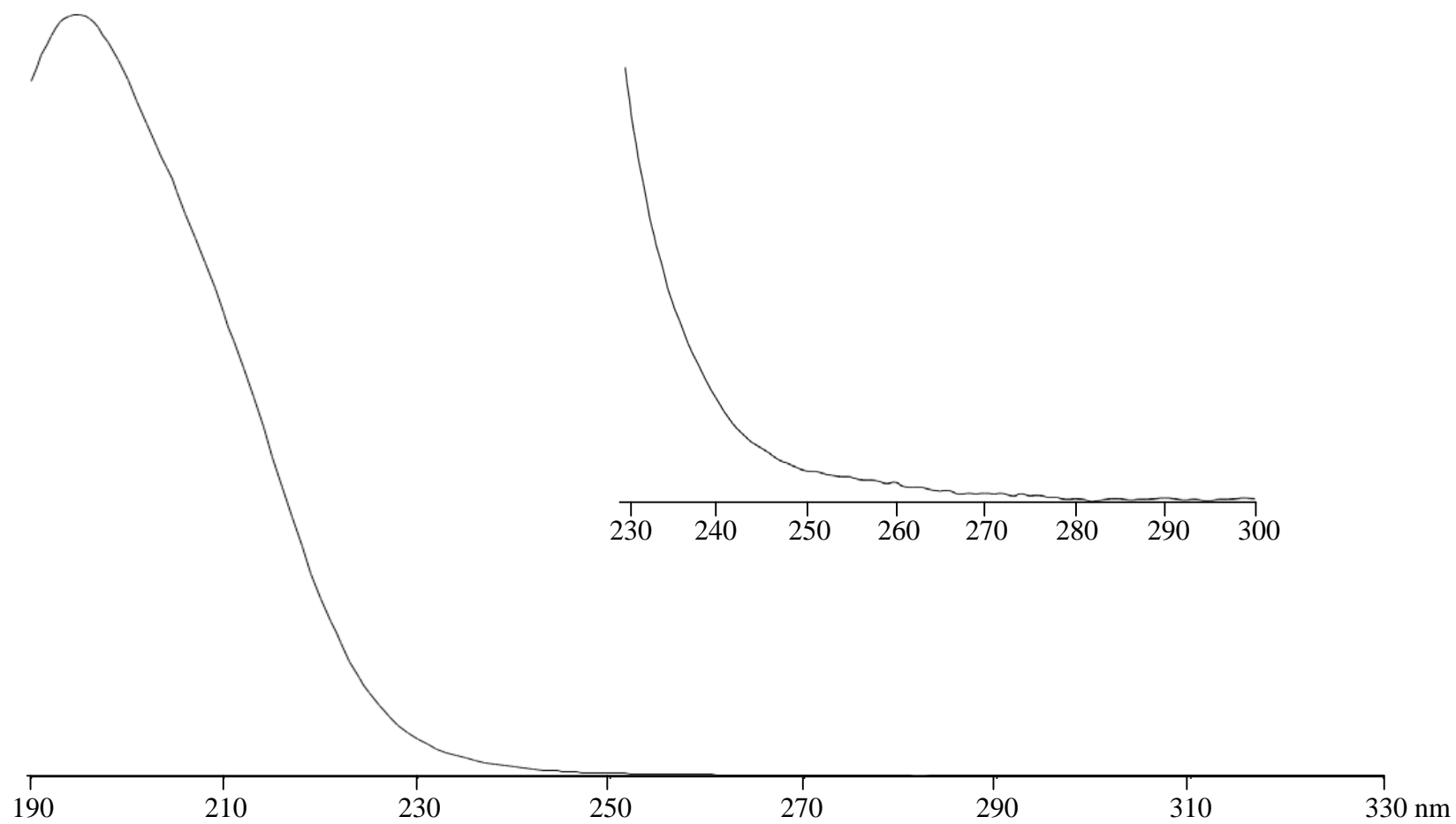


Figure 4.2 Room temperature absorption spectrum of SbH_3 ; inset; expanded view of the 230-300 nm region.

Series 9, 0.8 mm orifice). The molecular beam was collimated by a 1-mm-diameter skimmer located 1 cm downstream from the nozzle.

Photolysis radiation at 193.3 nm photolyzed SbH_3 at the interaction region (5 cm downstream from the skimmer). Nascent hydrogen atoms were promoted to high- n Rydberg levels *via* a double resonant excitation: 121.6 nm radiation excited the H atom $2p \leftarrow 1s$ transition, and ~ 365 nm radiation promoted the $n \leftarrow 2p$ transition, where n was ~ 50 . Metastable H atoms that traversed the 43.5 cm flight tube were field ionized and detected by microchannel plates arranged in a chevron configuration. Time-of-flight spectra were recorded and converted to center of mass (c.m.) translational energy spectra

4.1.4 Discussion

The instability of SbH_3 (lifetime ~ 1.5 hours) was the limiting factor in the HRTOF experiments. As a result of the rapid decomposition of SbH_3 (to form $3\text{Sb} + 2\text{H}_2$), the majority of the recorded HRTOF spectra represent only 5 000 – 30 000 laser firings. However, the quality of the HRTOF spectra was not the biggest issue; the overall shape of the spectra was inconsistent. The first few experimental trials yielded HRTOF spectra that qualitatively resembled the AsH_3 results. In later trials, two distinct, sharp peaks were present atop the broad background signal. This precluded confident analysis and assignment of the spectra.

Great care was taken to accurately reproduce experimental conditions for each HRTOF study. However, given the fickle nature of laser systems and the complications inherent in the SbH_3 synthesis, minute variations between experiments were expected. It

is possible that day-to-day fluctuations in laser intensities and focusing conditions led to multiphoton events and the varying features in the SbH_3 HRTOF spectra.

Despite the inconsistencies in the structure of the HRTOF spectra, a few general observations can still be made. All of the c.m. translational energy distributions are broad with a maximum at low $E_{c.m.}$. This suggests that SbH_2 products are formed with a significant amount of internal excitation. There is also clear evidence of secondary SbH_2 photodissociation.

In light of the photodissociation dynamics of NH_3 , PH_3 and AsH_3 , it is reasonable to expect that the SbH_2 photoproducts will be born with significant internal excitation. The $\text{SbH}_3 \tilde{A} \leftarrow \tilde{X}$ transition is accompanied by a large change in equilibrium geometry ($\theta_{H-Sb-H} = 110.5^\circ \leftarrow 91.5^\circ$)³, which results in ν_2 (umbrella) vibrational excitation. It is plausible that this out-of-plane bending motion can be directly carried through to SbH_2 a -axis rotation. The equilibrium values of θ_{H-Sb-H} for $\text{SbH}_3(\tilde{A})$ and $\text{SbH}_2(\tilde{X})$ are 110.5° and 89.8° , respectively.³ Again, taking cues from PH_3 and AsH_3 , this large difference of 20.7° may lead to significant bending excitation in $\text{SbH}_2(\tilde{X})$.

We have been given a sneak peek of the photodissociation dynamics of SbH_3 , and are left wanting more. The photodissociation of SbH_3 at 248 nm should be interesting since the photon energy will only be able to cleave one Sb-H bond. However, the success of future SbH_3 HRTOF experiments hinges upon sample stability. Collaboration with synthetic chemists might prove beneficial.

4.2 BiH₃

Bismuthine, BiH₃, is the last and ultimate member of the group-V hydrides. BiH₃(\tilde{X}^1A_1) has the smallest bond angle ($\theta_{H-Sb-H} = 90.3^\circ$) compared with its lighter group-V relatives and is a near-spherical oblate symmetric top ($B_0 \sim C_0$).^{3,24,25} The severe instability of BiH₃ and the difficulty associated with the synthesis has frustrated experimental research. Prior to 2002, no one was able to successfully replicate the BiH₃ synthesis first reported by E. Amberger in 1961.²⁶

The bismuth hydrides, especially BiH, have garnered theoretical interest due to the large role played by relativistic and spin-orbit effects.^{3,27,28} It is probable that these effects dramatically influence the photodissociation dynamics of BiH₃. Assuming that we could repeat the Amberger synthesis, the investigation of BiH₃ *via* HRTOF spectroscopy should provide valuable insight as to how relativistic effects influence photodissociation dynamics. In keeping with our studies on AsH₃ and SbH₃, 193.3 and 248 nm radiations are reasonable choices. The photon energy at both 193.3 nm and 248 nm has sufficient energy to break two H-bonds. Figure 4.3 presents an energy level diagram of possible BiH_n products.

4.3 A Quick Look at AsH₂

The dissociation dynamics of AsH₃ following 193.3 nm photolysis are complicated due to the multitude of possible reaction channels and AsH₂ secondary photodissociation. These factors limit our ability to resolve product state distributions.

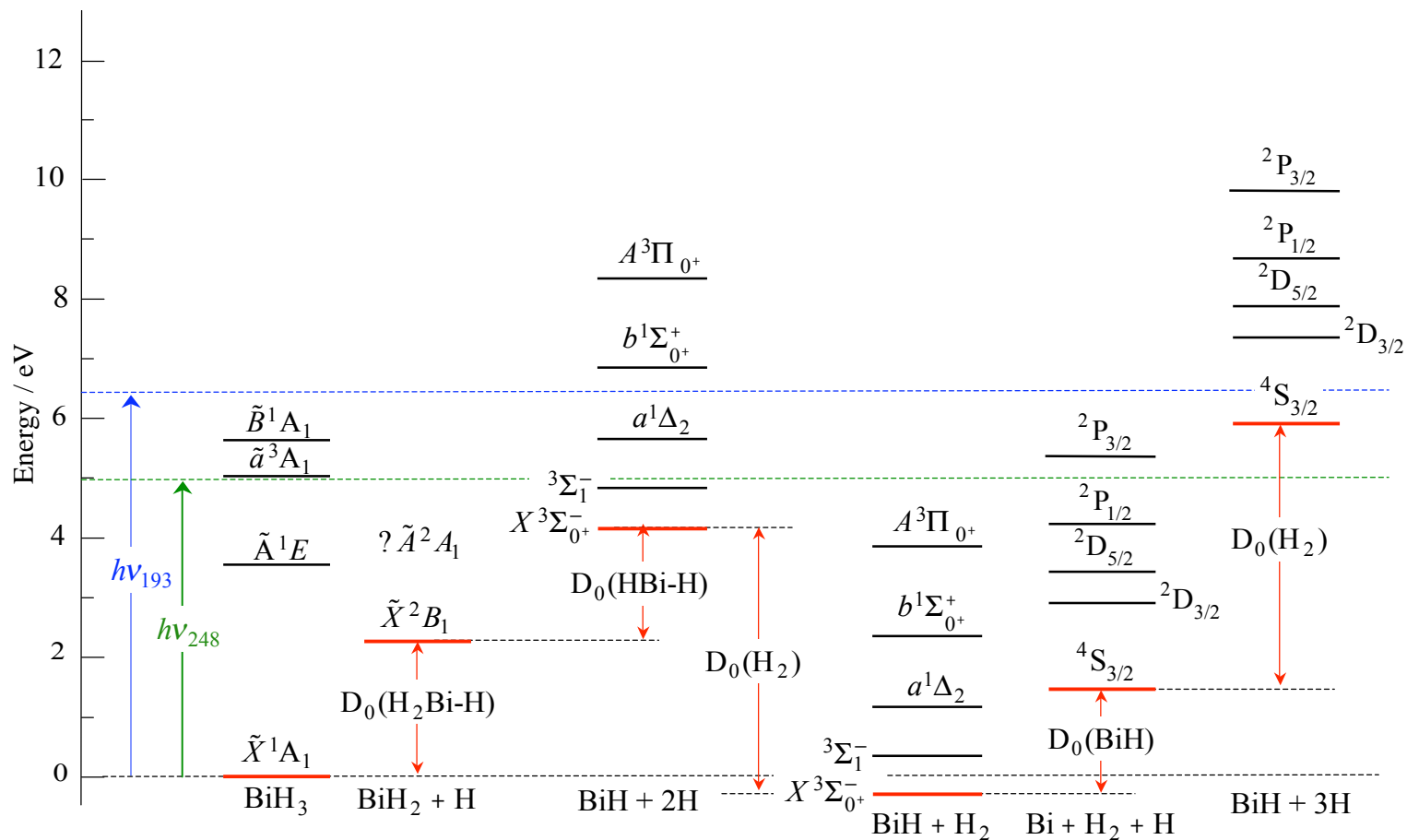


Figure 4.3 Energy level diagram for the 193.3 and 248 nm photolysis of BiH_3 . It should be noted that spin-orbit coupling splits the electronic states of BiH into numerous relativistic states. Only a few BiH spin-orbit states are shown here.^{3,27-29}

Our recent experimental results following the 193.3 nm photodissociation of AsH₃ (using high- n Rydberg hydrogen time-of-flight spectroscopy) yield broad c.m. translational energy distributions that peak at low $E_{c.m.}$. The modest amount of superimposed structure suggests that AsH₂ products are formed with significant internal excitation. Definitive assignment of the structure is impossible due the broad background and secondary photolysis.¹⁴

An experimental study of the photodissociation of jet cooled AsH₂ in which there is no contribution from AsH₃ background would resolve a number of issues. For example, this could be achieved by photodissociating AsH₃ in a high-pressure quartz expansion channel and then photodissociating expansion-cooled AsH₂ in spectral regions where AsH₃ does not absorb radiation. Figure 4.4 provides a possible experimental set-up.

The photodissociation dynamics of AsH₂ should prove to be interesting. The ground-state electron configuration of AsH₂ is $\dots(b_2)^2(a_1)^2(b_1)^1$.²⁷ The $\tilde{A}^2A_1 \leftarrow \tilde{X}^2B_1$ transition results from the promotion of an electron from the a_1 orbital to the b_1 orbital and is accompanied by a large increase in bond angle ($\theta_{H-As-H} : 123^\circ \leftarrow 90.4^\circ$).³⁰ AsH₂(\tilde{X}^2B_1) and AsH₂(\tilde{A}^2A_1) form a Renner-Teller pair; both states correlate with a $^2\Pi$ state at linear geometry. Fluorescence studies have shown that AsH₂(\tilde{A}) vibrational states are predissociated.^{30,31} It has been suggested that spin-orbit interactions are responsible for the predissociation.^{30,31} Possible dissociation pathways were discussed in chapter 3.

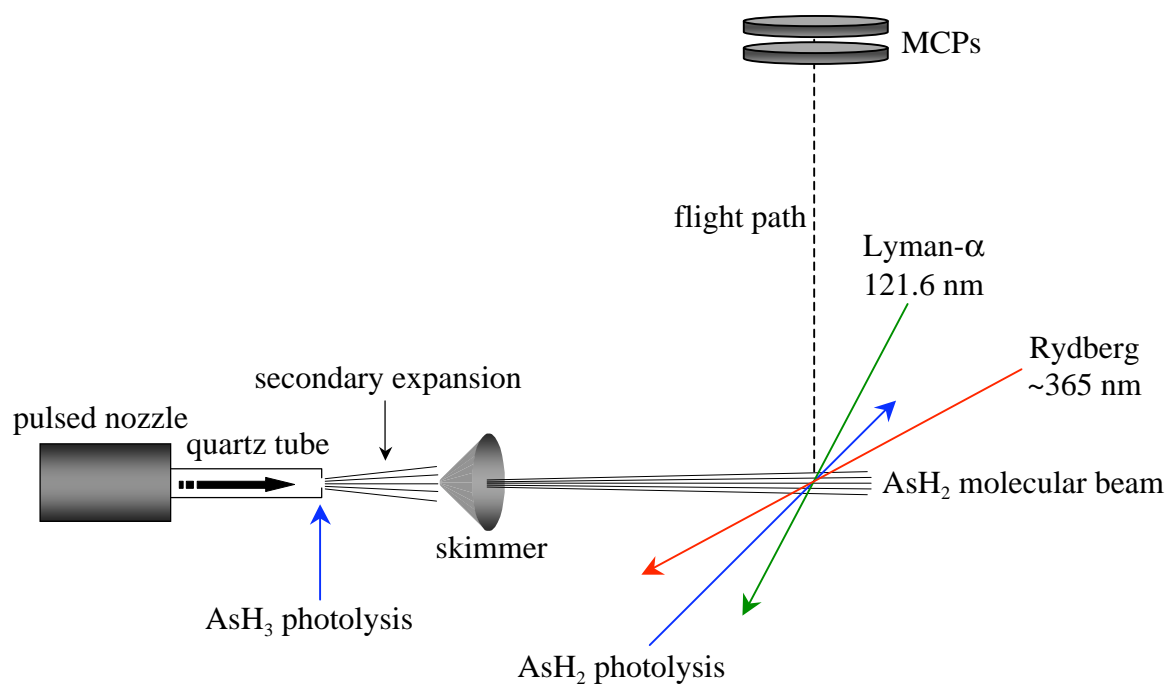


Figure 4.4 Schematic of a HRTOF experiment designed to probe AsH₂.

4.3.1 SbH₂ and BiH₂

The photodissociation dynamics of SbH₂ and BiH₂ could also be studied utilizing the experimental set-up described above. Relativistic and spin-orbit effects greatly perturb the electronic states of SbH and BiH.^{21,27,28} The inclusion of spin-orbit coupling splits the diatomic electronic states into their respective Ω states. Ω is defined as: $\Omega = |\Lambda + S|$, where Λ is the angular momentum along the internuclear axis and S is the spin angular momentum. For example, the $X^3\Sigma^-$ and $A^3\Pi$ electronic states of SbH and BiH form $0^+, 1$ and $0^+, 0^-, 1, 2$ relativistic states, respectively.^{21,28} Consequently, unique avoided crossings will lead to exciting dissociation dynamics!

4.4 Chapter 4 References

1. Greenswood, N. N.; Earnshaw, A. *Chemistry of the Elements*; Butterworth-Heinemann: Oxford, 1997.
2. Herman, I. P. *Chem. Rev.* **1989**, *89*, 1323.
3. Dai, D.; Balasubramanian, K. *J. Chem. Phys.* **1990**, *93*, 1837.
4. Ruscic, B.; Berkowitz, J. *J. Chem. Phys.* **1993**, *99*, 5840.
5. Todd, M. A.; Bandarari, G.; Baum, T. H. *Chem. Mater.* **1999**, *11*, 547.
6. http://www.osha.gov/dts/chemicalsampling/data/CH_219590.html
7. Biesner, J.; Schneider, L.; Schmeer, J.; Ahlers, G.; Xie, X.; Welge, K. H.; Ashfold, M. N. R.; Dixon, R. N. *J. Chem. Phys.* **1988**, *88*, 3607.
8. Lambert, I. R.; Morley, G. P.; Mordaunt, D. H.; Ashfold, M. N. R.; Dixon, R. N. *Can. J. Chem.* **1994**, *72*, 977.
9. Vaida, V.; McCarthy, M. I.; Engelking, P. C.; Rosmus, P.; Werner, H. J.; Botshwina, P. *J. Chem. Phys.* **1987**, *86*, 6669.
10. Humphries, C. M.; Walsh, A. D.; Warsop, P. A. *Discuss. Faraday Soc.* **1963**, *35*, 148.
11. Maripuu, R.; Reineck, I.; Ågren, H.; Nian-Zu, W.; Rong, J. M.; Veenhuizen, H.; Al-Shamma, S. H.; Karlsson, L.; Siegbahn, K. *Mol. Phys.* **1983**, *48*, 1255.
12. Berkowitz, J. *J. Chem. Phys.* **1988**, *89*, 7065.
13. Potts, A. W.; Price, W. C. *Proc. R. Soc. London, Ser. A* **1972**, *326*, 181.
14. Smith-Freeman, L. A.; Schroeder, W. P.; Wittig, C. *J. Phys. Chem. A* **2009**, *113*, 2158.
15. McCarthy, M. I.; Rosmus, P.; Werner, H. J.; Botshwina, P.; Vaida, V. *J. Chem. Phys.* **1987**, *89*, 6693.
16. Loomis, R. A.; Reid, J. P.; Leone, S. J. *J. Chem. Phys.* **2002**, *125*, 658.
17. Biesner, J.; Schneider, L.; Ahlers, G.; Xie, X.; Welge, K. H.; Ashfold, M. N. R.; Dixon, R. N. *J. Chem. Phys.* **1989**, *91*, 2901.

18. Müller, J.; Ågren, H. *J. Chem. Phys.* **1982**, *76*, 5060.
19. Ni, T.; Yu, S.; Ma, X; Kong, F. *Chem. Phys. Lett.* **1986**, *128*, 270.
20. Ni, T.; Lu, Q.; Ma, X; Yu, S.; Kong, F. *Chem. Phys. Lett.* **1986**, *126*, 417.
21. Balasubramanian, K. *J. Mol. Spectrosc.* **1987**, *124*, 458.
22. Balasubramanian, K. *Relativistic Effects in Chemistry, Parts A and B*; Wiley & Sons: New York, 1997.
23. Pitzer, K. *Acc. Chem. Res.* **1979**, *12*, 271.
24. Jerzembeck, W.; Bürger, H.; Constantin, F. L.; Margulès, L.; Demaison, J. *J. Mol. Spectrosc.* **2004**, *226*, 24.
25. Jerzembeck, W.; Bürger, H.; Constantin, F. L.; Margulès, L.; Demaison, J.; Breidung, W. T. *Angew. Chem. Int.* **2002**, *41*, 2550.
26. Amberger, E. *Chem. Ber.* **1961**, *94*, 1447.
27. Alekseyev, A.; Buenker, R. J.; Liebermann, H.-P.; Hirsch, G. *J. Chem. Phys.* **1994**, *100*, 2989.
28. Balasubramanian, K. *J. Mol. Spectrosc.* **1989**, *115*, 258.
29. Moore, C. E. *Atomic Energy Levels*: National Bureau of Standards: Washington, DC, 1971.
30. He, S.-G.; Clouthier, D. J. *J. Chem. Phys.* **2007**, *126*, 154312.
31. Dixon, R. N.; Duxbury, G.; Lamberton, H. M. *Proc. R. Soc. London Ser. A* **1968**, *305*, 271.

Bibliography

- Alekseyev, A.; Buenker, R. J.; Liebermann, H.-P.; Hirsch, G. *J. Chem. Phys.* **1994**, *100*, 2989.
- Amberger, E. *Chem. Ber.* **1961**, *94*, 1447.
- Aoyagi, Y.; Kanazawa, M.; Doi, A.; Iwai, S.; Namba, S. *J. Appl. Phys.* **1986**, *60*, 3131.
- Aren, M.; Richter, W. *J. Chem. Phys.* **1990**, *93*, 7094.
- Ashfold, M. N. R.; Baggott, J. E. *Molecular Photodissociation Dynamics*; Royal Society of Chemistry: Piccadilly, 1987.
- Ashfold, M. N. R.; Lambert, I. R.; Mordaunt, D. H.; Morley, G. P.; Western, C. M. *J. Phys. Chem.* **1992**, *96*, 2938.
- Ashfold, M. N. R.; Mordaunt, D. H.; Wilson, S. H. S. *Adv. Photochem.* **1996**, *21*, 217.
- Balasubramanian, K. *J. Mol. Spectrosc.* **1987**, *124*, 458.
- Balasubramanian, K. *J. Mol. Spectrosc.* **1989**, *115*, 258.
- Balasubramanian, K. *Relativistic Effects in Chemistry, Part A*; John Wiley & Sons, Inc: New York, 1997.
- Balasubramanian, K. *Relativistic Effects in Chemistry, Part B*; John Wiley & Sons, Inc: New York, 1997.
- Balasubramanian, K.; Nannegari, V. *J. Mol. Spectrosc.* **1989**, *138*, 482.
- Baugh, D.; Koplitz, B.; Xu, Z.; Wittig, C. *J. Chem. Phys.* **1988**, *88*, 879.
- Berkowitz, J. *J. Chem. Phys.* **1988**, *89*, 7065.
- Berthou, J. M.; Pascat, B.; Guenebaut, H.; Ramsay, D. A. *Can. J. Phys.* **1972**, *50*, 2265.
- Biesner, J.; Schneider, L.; Ahlers, G.; Xie, X.; Welge, K. H.; Ashfold, M. N. R.; Dixon, R. N. *J. Chem. Phys.* **1989**, *91*, 2901.
- Biesner, J.; Schneider, L.; Schmeer, J.; Ahlers, G.; Xie, X.; Welge, K. H.; Ashfold, M. N. R.; Dixon, R. N. *J. Chem. Phys.* **1988**, *88*, 3607.

Biesner, J.; Schnieder, L.; Ahlers, G.; Xie, X.; Welge, K. H.; Ashfold, M. N. R.; Dixon, R. N. *J. Chem. Phys.* **1989**, *91*, 2901.

Binning Jr., R. C.; Curtiss, L. A. *J. Chem. Phys.* **1990**, *92*, 1860.

Buetel, M.; Setzer, K. D.; Shestakov, O.; Fink, E. H. *J. Mol. Spectrosc.* **1996**, *178*, 165.

Busch, G. E.; Wilson, K. R. *J. Chem. Phys.* **1972**, *56*, 3626.

Butler, L. J. *Annu. Rev. Phys. Chem.* **1998**, *49*, 125.

Butler, L. J.; Neumark, D. M. *J. Phys. Chem.* **1996**, *100*, 12801.

Christiansen, P. A.; Ermler, W. C.; Pitzer, K. S. *Annu. Rev. Phys. Chem.* **1985**, *36*, 407.

Dai, D.; Balasubramanian, K. *J. Chem. Phys.* **1990**, *93*, 1837.

Dixon, R. N. *Acc. Chem. Res.* **1991**, *24*, 16.

Dixon, R. N.; Duxbury, G.; Lamberton, H. M. *Proc. R. Soc. London Ser. A* **1968**, *305*, 271.

Dixon, R. N.; Lamberton, H. M. *J. Mol. Spectrosc.* **1968**, *25*, 12.

Donnelly, V. M.; Karlicek, R. F. *J. Appl. Phys.* **1982**, *53*, 6399.

Gallagher, T. F. *Rydberg Atoms*; Cambridge University Press: Cambridge, 1994.

Greenswood, N. N.; Earnshaw, A. *Chemistry of the Elements*; Butterworth-Heinemann: Oxford, 1997.

Greiner, W. *Relativistic Quantum Mechanics*; Springer: New York, 1997.

Hall, G. E.; Houston, P. L. *Annu. Rev. Phys. Chem.* **1989**, *40*, 375.

Hause, M. L.; Yoon, Y. H.; Crim, F. F. *J. Chem. Phys.* **2006**, *125*, 174309.

He, S.-G.; Clouthier, D. J. *J. Chem. Phys.* **2007**, *126*, 154312.

Herman, I. P. *Chem. Rev.* **1989**, *89*, 1323.

http://www.osha.gov/dts/chemicalsampling/data/CH_219590.html

Humphries, C. M.; Walsh, A. D.; Warsop, P. A. *Discuss. Faraday Soc.* **1963**, *35*, 148.

- Jakubetz, W. *Methods in Reaction Dynamics*; Springer: New York, 2001.
- Jasper, A. W.; Nangia, S.; Zhu, C.; Truhlar, D. G. *Acc. Chem. Res.* **2006**, *39*, 101.
- Jerzembeck, W.; Bürger, H.; Constantin, F. L.; Margulès, L.; Demaison, J. *Mol. Spectrosc.* **2004**, *226*, 24.
- Jerzembeck, W.; Bürger, H.; Constantin, F. L.; Margulès, L.; Demaison, J.; Breidung, W. T. *Angew. Chem. Int.* **2002**, *41*, 2550.
- Kassab, E.; Gleghorn, J. T.; Evleth, E. M. *J. Am. Chem. Soc.* **1983**, *105*, 1746.
- Kim, Z. H.; Alexander, A. J.; Kandel, S. A.; Rakitzis, T. P.; Zare, R. N. *Faraday Discuss.* **1999**, *113*, 27.
- Kopplitz, B.; Xu, Z.; Wittig, C. *Appl. Phys. Lett.* **1988**, *52*, 860.
- Kukimoto, H.; Ban, Y.; Komatsu, H.; Takechi, M.; Ishizaki, M. *J. Cryst. Growth* **1986**, *77*, 223.
- Lambert, I. R.; Morley, G. P.; Mordaunt, D. H.; Ashfold, M. N. R.; Dixon, R. N. *Can. J. Chem.* **1994**, *72*, 977.
- Lee, Y.T.; McDonald, J. D.; Lebreton, P. R.; Herschbach, D. R. *Rev. Sci. Instrum.* **1969**, *40*, 1402.
- Loomis, R. A.; Reid, J. P.; Leone, S. J. *J. Chem. Phys.* **2000**, *112*, 658.
- Manthe, U.; Köppel, H. *J. Chem. Phys.* **1990**, *93*, 1658.
- Maripuu, R.; Reineck, I.; Ågren, H.; Nian-Zu, W.; Rong, J. M.; Veenhuizen, H.; Al-Shamma, S. H.; Karlsson, L.; Siegbahn, K. *Mol. Phys.* **1983**, *48*, 1255.
- McCarthy, M. I.; Rosmus, P.; Werner, H. J.; Botshwina, P.; Vaida, V. *J. Chem. Phys.* **1987**, *86*, 6693.
- Miller, W. H. *Dynamics of Molecular Collisions, Part B*; Plenum Press: New York, 1976.
- Moore, C. E. *Atomic Energy Levels*; National Bureau of Standards: Washington, DC, 1971.
- Mordaunt, D.; Ashfold, M. N. R.; Dixon, R. N. *J. Chem. Phys.* **1996**, *104*, 6460.
- Müller, J.; Ågren, H. *J. Chem. Phys.* **1982**, *76*, 5060.

- Nangia, S.; Truhlar, D. G. *J. Chem. Phys.* **2006**, *124*, 124309.
- Ni, T.; Lu, Q.; Ma, X.; Yu, S.; Kong, F. *Chem. Phys. Lett.* **1986**, *126*, 417.
- Ni, T.; Yu, S.; Ma, X.; Kong, F. *Chem. Phys. Lett.* **1986**, *128*, 270.
- Oxtoby, D. W.; Gillis, H. P.; Nachtrieb, N. H. *Principles of Modern Chemistry*; Thomson Learning, Inc.: Ontario, 2002.
- Pitzer, K. *Acc. Chem. Res.* **1979**, *12*, 271.
- Potts, A. W.; Price, W. C. *Proc. R. Soc. London Ser. A.* **1972**, *326*, 181.
- Pütz, N.; Heinecke, H.; Veuhoff, E.; Arens, G.; Heyen, M.; Lüth, H.; Balk, P. *J. Cryst. Growth* **1984**, *68*, 194.
- Pyykkö, P.; Desclaux, J.-P. *Acc. Chem. Res.* **1979**, *12*, 276.
- Ranu, R.; Peyerimhoff, S. D.; Buenker, R. J. *J. Mol. Spectrosc.* **1977**, *68*, 253.
- Rich, R. *Periodic Correlations*; W. A. Benjamin: New York, 1965.
- Riley, S. J.; Wilson, K. R. *Faraday Discuss. Chem. Soc.* **1972**, *53*, 132.
- Rosker, M. J.; Dantus, M.; Zewail, A. H. *J. Chem Phys.* **1988**, *89*, 6113.
- Rosmus, P.; Botschwina, P.; Werner, H. J.; Vaida, V.; Engelking, P. C.; McCarthy, M. I. *J. Chem. Phys.* **1987**, *86*, 6677.
- Ruscic, B.; Berkowitz, J. *Chem. Phys.* **1993**, *99*, 5840.
- Sam, C. L.; Yardley, J. T. *J. Chem. Phys.* **1978**, *69*, 4621.
- Sato, H. *Chem. Rev.* **2001**, *101*, 2687.
- Scerri, E. R. *The Periodic Table: Its Story and its Significance*; Oxford University Press: Oxford, 2007.
- Scherer, N. F.; Knee, J. L.; Smith, D. D.; Zewail, A. H. *J. Phys. Chem.* **1985**, *89*, 5141.
- Schnieder, L.; Meier, W.; Welge, K. H.; Ashfold, M. N. R.; Western, C. M. *J. Chem. Phys.* **1990**, *92*, 7027.

- Scoles, G. *Atomic and Molecular Beam Methods*; Oxford University Press: New York, 1988, Vol. 1.
- Shapiro, M; Bersohn, R. *Annu. Rev. Phys. Chem.* **1982**, *33*, 409.
- Shinke, R. *Photodissociation Dynamics*; Cambridge University Press: Cambridge, 1993.
- Simmons, J. P. *J. Phys. Chem.* **1984**, *88*, 1287.
- Smith-Freeman, L. A.; Schroeder, W. P.; Wittig, C. *J. Phys. Chem. A.* **2009**, *113*, 2158.
- Todd, M. A.; Bandarari, G.; Baum, T. H. *Chem. Mater.* **1999**, *11*, 547.
- Vaida, V.; McCarthy, M. I.; Engelking, P. C.; Rosmus, P.; Werner, H. J.; Botschwina, P. *J. Chem. Phys.* **1987**, *86*, 6669.
- Walsh, A. D. *J. Chem. Soc.* **1953**, 2296.
- Wilson, K. R. *Excited State Chemistry*; Pitts, J. N., Eds.; Gordon and Breach: New York 1970
- Wiza, J. L. *Nuclear Instruments and Methods*, **1979**, *162*, 587.
- Wodtke, A. M.; Lee, Y. T. *Molecular Photodissociation Dynamics*; Ashfold, M. N. R.; Baggott, J. E., Eds.; The Royal Society of Chemistry Burlington House: London 1987; pp. 31-59.
- Worth, G. A.; Cederbaum, L. S. *Annu. Rev. Phys. Chem.* **2004**, *55*, 127.
- Xie, X.; Schnieder, L.; Wallmeier, H.; Boettner, R.; Welge, K. H.; Ashfold, M. N. R. *J. Chem. Phys.* **1990**, *92*, 1608.
- Xuan, C. N; Margani, A. *J. Chem. Phys.* **1994**, *100*, 7000.
- Yarkony, D. *Acc. Chem. Res.* **1998**, *31*, 511.
- Yarkony, D. *J. Phys. Chem. A.* **2001**, *105*, 6277.
- Zhang, J.; Dulligan, M.; Wittig, C. *J. Phys. Chem.* **1995**, *99*, 7446.
- Zhang, J.; Dulligan, M.; Wittig, C. *J. Phys. Chem.* **1997**, *107*, 1403.
- Zhang, J.; Riehn, C. W.; Dulligan, M.; Wittig, C. *J. Chem. Phys.* **1996**, *104*, 7027.

Zumdahl, S. S.; Zumdahl, S. A. *Chemistry*; Houghton Mifflin Company: New York, 2007.